Chemical Science

Accepted Manuscript

This article can be cited before page numbers have been issued, to do this please use: S. Rajapakse, Y. Lee, S. B. Jayawardana, J. Helms, P. Mondal, A. Singh, B. S. Pierce, H. S. Shafaat and G. B. Wijeratne, *Chem. Sci.*, 2025, DOI: 10.1039/D4SC08701A.

ROYAL SOCIETY OF CHEMISTRY

rsc.li/chemical-science

View Article Online
DOI: 10.1039/D4SC08701A

ARTICLE

Modulation of Heme Peroxo Nucleophilicities with Axial Ligands Reveal Key Insights into the Mechanistic Landscape of Nitric Oxide Synthase

Received 00th January 20xx,
Accepted 00th January 20xx

DOI: 10.1039/x0xx00000x

Shanuk Rajapakse,[a] Yuri Lee,[b] Samith B. Jayawardana,[a] Joshua Helms,[a] Pritam Mondal,[a,c] Akhil Singh,[a] Brad S. Pierce,[a,*] Hannah S. Shafaat,[b,*] and Gayan B. Wijeratne[a,*]

Mid-valent heme-oxygen intermediates are central to a medley of pivotal physiological transformations in humans, and such systems are increasingly becoming more relevant therapeutic targets for challenging disease conditions. Nonetheless, precise mechanistic details pertaining to mid-valent heme intermediates as well as key structure-activity relationships remain enigmatic. To this end, this study strives to describe the influence of heme proximal ligation on the nucleophilic reactivity patterns of heme peroxo intermediates. A functional model system in which organic oxime substrates are used as *N*-hydroxy-L-arginine mimics reproduces the second mechanistic step of nitric oxide synthase. Our findings reveal that axial ligation of heme peroxo adducts escalates the rates of nucleophilic reactivity, wherein the anionic ligands exhibited the most pronounced "push effect". Coordination of these axial ligands are accompanied by distinct geometric and electronic perturbations, which are supported by complementary theoretical studies. Kinetic interrogations reveal that the axially ligated heme peroxo adducts presumably mediate oxime oxidation via the same mechanism as the parent (i.e., with only solvent ligation) heme-PO adduct, where the initial nucleophilic attack from the peroxo moiety on the oxime substrate is rate-limiting. All reaction products, including the final ketone as well as NO^-, have been characterized in detail.

Introduction

Heme enzymes are the cornerstones for a broad diversity of biological functionalities, and, hence, are ubiquitous within various aerobic and anaerobic organisms.[1-3] One of the key parameters that dictate the functional divergence of heme enzymes is the choice of the proximally ligating amino acid residue. Nature has meticulously designated these proximal amino acids to tailor the electronic properties of heme centers toward precise biological roles.[4, 5] In dioxygen-activating heme enzymes, the proximal ligands are directly involved in orchestrating the extent of dioxygen reduction, as well as in governing the attributes of heme oxygen intermediates that modulate their reactivities. For example, in heme enzymes where dioxygen activation leads to O–O bond cleavage giving high-valent intermediates such as Compound-I (i.e., $(P^{\bullet+})Fe^{IV}=O$ (Cmpd-I); formed via heterolytic O–O bond scission) or Compound-II (i.e., $(P)Fe^{IV}=O$ (Cmpd-II); formed via homolytic O–O bond scission or reduction of Cmpd-I), strongly donating anionic ligands typically occupy the heme proximal site (e.g., cysteinate, tyrosinate, or histidinate/imidazolate (Figure 1A, C and D)).[1, 6, 7] In contrast, in oxygen carrier proteins (e.g., hemoglobin or myoglobin) or heme dioxygenase enzymes (e.g., indoleamine/tryptophan 2,3-dioxygenases), where O–O bond cleavage is initially unwarranted, a neutral ligand (e.g., histidine (Figure 1B)) resides at the proximal site.[1-3, 8-11] Moreover, non-covalent interactions with these proximally ligated amino acids further modulate their electronic properties, which Nature has evolutionarily optimized to fine-tune the chemistry carried out at a specific heme center (see Figure 1A-D dotted lines).[12-16] Correspondingly, intrinsic dissimilarities in the kinetics and thermodynamics of formation as well as fundamental structural, spectroscopic, and reactivity properties exist across various heme-oxygen intermediates, often paralleling the donor ability of the proximally ligating amino acid side chains.[17-23] In light of these trends, the influence of various axial ligands on the geometric and electronic properties of high-valent heme intermediates, such as Cmpd-I or Cmpd-II, has been well-established utilizing both enzymatic systems as well as their synthetic models.[24-34] Nonetheless, how those same parameters influence the reactivities of mid-valent heme oxygen intermediates (i.e., Fe(III) containing adducts such as heme superoxo, peroxo, hydroperoxo, or alkylperoxo) are far

[a] Department of Chemistry and Biochemistry, University of Alabama, Tuscaloosa, AL 35401, United States. E-mail: gwijeratne@ua.edu
[b] Department of Chemistry and Biochemistry, University of California, Los Angeles, Los Angeles, CA 90095, United States. E-mail: shafaat@ucla.edu
[c] Current address: Department of Chemical Sciences, Indian Institute of Science Education and Research, Mohali, Punjab 140306, India.
Electronic Supplementary Information (ESI) available: Detailed experimental procedure, spectroscopic characterization, and computational procedures. See DOI: 10.1039/x0xx00000x

View Article Online
DOI: 10.1039/D4SC08704A

less understood.[35-41] This lack of systematic understanding of structure-function relationships is notable, particularly in light of the growing body of evidence on heme systems where heme peroxo species are either active oxidants or key intermediates being pivotal to challenging disease situations in humans (e.g., COVID-19, autoimmune and/or neurodegenerative conditions, and cancer).[42-46] These include nitric oxide synthase (NOS),[47] aromatase (CYP19A1),[48] sterol 14α-demethylase (CYP51),[49] cytochrome P450 17α-hydroxylase-17,20-lyase (CYP17A1),[50] and non-canonical heme oxygenase (IsdG-type),[51] which have emerged as multifaceted therapeutic targets in recent years; consequently, identifying potential inhibitory pathways of these systems are of prime interest for rational drug design.

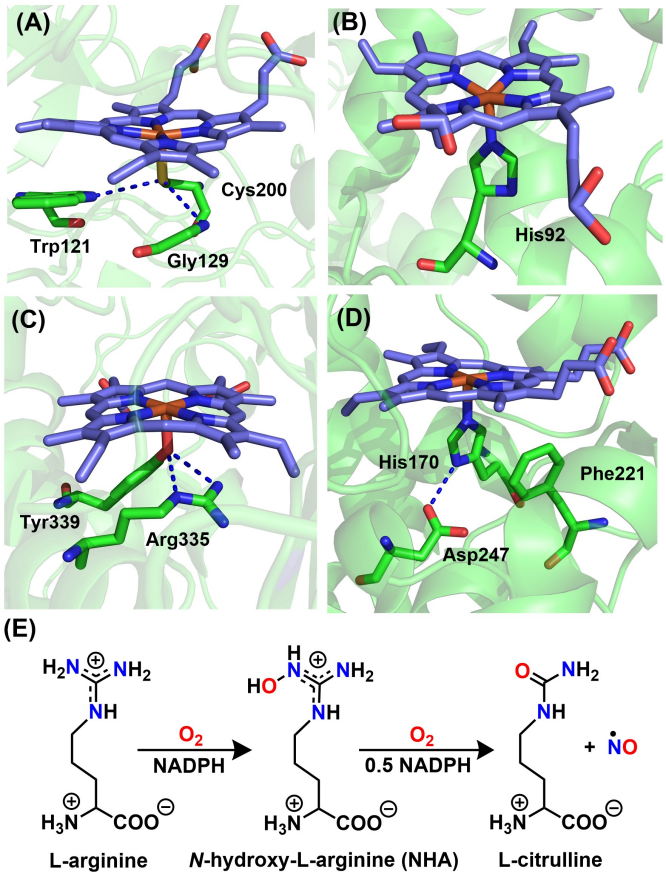

Figure 1. Active site structures of (A) nitric oxide synthase (PDB: 1NSI[52]), (B) deoxy-hemoglobin (PDB: 4HHB[53]), (C) catalase (PDB: 2IQF[54]), and (D) peroxidase (PDB: 1ATJ[55]) which encompass cysteinate, histidine, tyrosinate, and histidinate/imidazolate axially ligated amino acid residues, respectively. (E) Sequential reactions proposed to be catalyzed by nitric oxide synthase, transforming L-arginine into L-citrulline and •NO.

In particular, NOS has been implicated in a wide variety of pathogenic situations, from neurodegenerative disorders (e.g., Alzheimer's,[56] Parkinson's,[57] Huntington's[58, 59] diseases, amyotrophic lateral sclerosis[60]) to a variety of cancers (e.g., breast,[61, 62] prostate,[63] colorectal,[64] cervical,[65] lung,[66] brain,[67, 68] colon,[69] ovarian[70]), both due to its proposed direct involvement in prognosis and/or the detrimental effects imparted by its main reaction product, nitric oxide (•NO).[71, 72] Indeed, NOS is central to the primary pathway that generates •NO in humans via arginine degradation under aerobic conditions.[73] •NO serves as a crucial signaling agent within the physiological space, with paramount roles in blood pressure regulation and cell signaling, among others.[74] Nonetheless, elevated •NO concentrations can impart a multitude of harmful effects via the elevation of nitrative and nitrosative stress, leading to undesirable protein nitration and disruption of key cell signaling pathways, often resulting in apoptosis.[75] Accordingly, NOS inhibitors have acquired significant momentum in recent years as highly potent therapeutic agents.[76-78] However, their rational design is impeded by the lack of a precise understanding into the NOS mechanism.[79] Some proposals exist wherein NOS has been proposed to operate via a two-step mechanism; the first involves the monooxygenation of L-arginine to *N*-hydroxy-L-arginine (NHA), followed by further oxidation of NHA to L-citrulline in the second step, with the concomitant production of •NO (Figure 1E).[47, 74, 80-83] Exact details pertaining to the latter step have been under debate, where several mechanistic propositions have been put forward, implicating largely different heme-based active oxidants. These involve both high-valent and mid-valent oxidants, although heme ferric peroxo or heme superoxo (i.e., mid-valent) based proposals have been heavily reproduced in the literature, while also being corroborated by distinct experimental observations.[1, 84-91] Interestingly, when heme peroxo is the active oxidant, the final NO_x product is nitroxide (NO^-). We have recently utilized synthetic model systems of both heme peroxo (heme-PO) and superoxo intermediates to shine light on the relevant mechanistic ambiguities, where we demonstrated that heme-PO adducts can indeed oxidize oxime substrates (i.e., as NHA mimics) in a bioinspired fashion, producing the corresponding ketone and nitroxide anions (NO^-).[92] Moreover, the rate-limiting step of this reaction landscape was found to be the initial nucleophilic attack mediated by the heme-PO adduct on the oxime substrate. Nonetheless, key unknowns still exist with respect to the exact structure-activity relationships of both the NOS heme center as well as the substrate that precisely choreograph the feasibility and efficiency of this unique mechanistic step.

Synthetic model complexes can be powerful tools in addressing such mechanistic uncertainties, mainly owing to a medley of unique advantages (e.g., the feasibility of (i) precise structural alterations and (ii) detailed mechanistic investigations under cryogenic conditions, etc.) inherent to such systems compared to their biological/enzymatic counterparts.[93] In this study, we evaluate the effect of proximal ligands on the reactivity patterns of heme-PO adducts, especially highlighting the details that pertain to the second mechanistic step of NOS. In that, we utilize a series of axially ligated (either neutral or anionic ligands) synthetic heme-PO oxidants, wherein the donor groups are biologically relevant. Therein, we utilize acetophenone oxime as the NHA mimic substrate (Scheme 1). Intriguingly, the nucleophilic reactivity between heme-PO adducts and oxime substrate was observed to be tightly regulated by the identity of the proximal ligand on heme, where increased donor abilities (i.e., the "push effect") led to faster kinetic rates. Furthermore,

View Article Online
DOI: 10.1039/D4SC08704A

we herein demonstrate for the first time how key thermodynamic and kinetic parameters of heme-PO driven reactivities are affected by various axial ligands, in turn resulting in measurable differences in substrate reaction rates. Systematic studies that evaluate the effect of axial ligands on bio-relevant reactivity landscapes of heme-PO intermediates (in either heme or non-heme biomimetic platforms) are sorely lacking in the contemporary literature, which underscores the importance of this current study.

Scheme 1. Generalized oxime oxidation reaction scheme facilitated by heme peroxo intermediates and the divergent exogenously added axial ligands evaluated in this study.

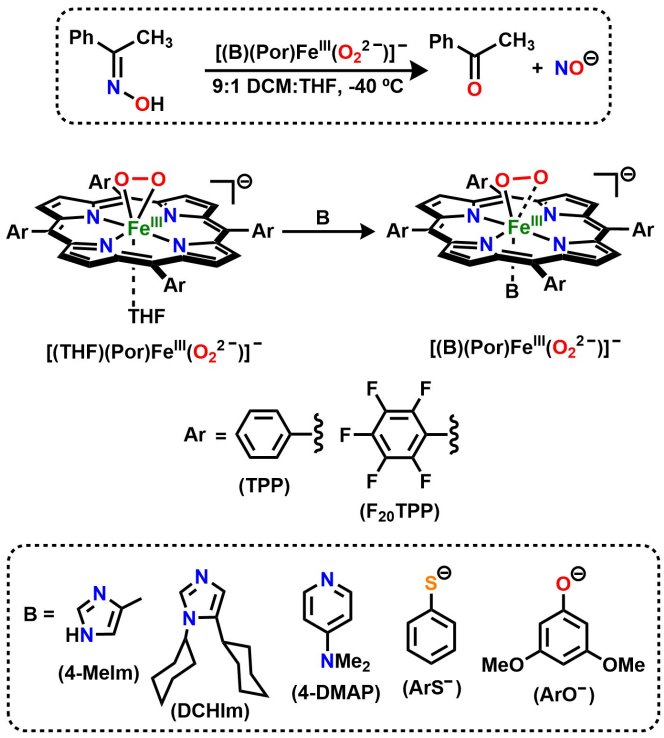

Results and Discussion

Formation of Axially Ligated Heme Peroxo Adducts

In order to survey the effects of various axial ligands on heme-PO driven nucleophilic reactivities, herein we utilize the ferric peroxo complex, [(THF)(TPP)Fe^{III}(O$_2^{2-}$)]$^-$, where TPP = 5,10,15,20-tetraphenylporphyrin.[92] The preparation and spectroscopic characterization of the side-on ferric peroxo species, [(THF)(TPP)Fe^{III}(O$_2^{2-}$)]$^-$ were carried out as previously described,[10, 92] and the spectroscopic characterization details are in excellent agreement with those reports. In particular, the prominent electronic absorption features of the starting ferrous complex, [(THF)$_2$(TPP)Fe^{II}], centered at 426 (Soret; ε = 3.4×10^5 M^{-1}cm^{-1}), 538 (ε = 1.08×10^4 M^{-1}cm^{-1}) and 558 (ε = 1.1×10^4 M^{-1}cm^{-1}) nm shifted to 416 (Soret; ε = 2.0×10^5 M^{-1}cm^{-1}) and 540 (ε = 1.58×10^4 M^{-1}cm^{-1}) nm upon its dioxygenation, converting into [(THF)(TPP)Fe^{III}(O$_2^{-\bullet}$)] at -40 °C in 9:1 DCM:THF solvent mixture (Figure 2A). Its subsequent reduction with 1 equiv of cobaltocene led to the formation of the corresponding side-on ferric peroxo species, [(THF)(TPP)Fe^{III}(O$_2^{2-}$)]$^-$, with electronic absorption features at 436 (Soret; ε = 2.7×10^5 M^{-1}cm^{-1}) and 564 (ε = 2.1×10^4 M^{-1}cm^{-1}) nm. The neutral or anionic axial ligands (e.g., 4-methylimidazole (4-MeIm), 1,5-dicyclohexylimidazole (DCHIm), 4-dimethylaminopyridine (4-DMAP), thiophenolate (ArS$^-$), and 3,5-dimethoxyphenolate (ArO$^-$); see Scheme 1) were then introduced into [(THF)(TPP)Fe^{III}(O$_2^{2-}$)]$^-$ in order to prepare the axially ligated heme-PO adducts.[94] In that, the addition of 2 equiv of 4-MeIm into a solution of [(THF)(TPP)Fe^{III}(O$_2^{2-}$)]$^-$ in 9:1 DCM:THF at –40 °C led to the formation of the corresponding axially ligated ferric peroxo species, [(4-MeIm)(TPP)Fe^{III}(O$_2^{2-}$)]$^-$, which was accompanied by only minor electronic absorption perturbations with main features observed at 436 (Soret; ε = 2.5×10^5 M^{-1}cm^{-1}) and 565 (ε = 2.0×10^4 M^{-1}cm^{-1}) nm. EPR spectroscopic analysis of [(4-MeIm)(TPP)Fe^{III}(O$_2^{2-}$)]$^-$ resulted in a prominent feature at g = 4.2, which again resembles that of the parent heme-PO species, [(THF)(TPP)Fe^{III}(O$_2^{2-}$)]$^-$ (Figure S2); this is indicative of a high-spin rhombic heme Fe(III) center in [(4-MeIm)(TPP)Fe^{III}(O$_2^{2-}$)]$^-$. Nonetheless, the isotope-sensitive *ν*(Fe–O) and *ν*(O–O) resonance Raman features of [(THF)(TPP)Fe^{III}(O$_2^{2-}$)]$^-$ shifted from 472 ($\Delta^{18}O_2$ = –21) cm^{-1} and 807 ($\Delta^{18}O_2$ = –44) cm^{-1} (Figure S3A) to 479 ($\Delta^{18}O_2$ = –23) cm^{-1} and 803 ($\Delta^{18}O_2$ = –47) cm^{-1}, respectively (Figure 2B), upon the axial ligation of 4-MeIm, implicating an effective strengthening of the Fe–O bond of heme-PO, and a corresponding slight weakening of the O–O bond. This change in bonding character reflects an inflow of electron density into the $\pi^*_{O-O(peroxo)}$ manifold (i.e., backbonding from the heme Fe center) upon axial ligation.[95] We argue that despite these subtle electronic perturbations, the heme-PO unit still remains side-on bound to the heme center, particularly due to the lack of any isotope-sensitive Fe-O stretching frequencies in the 550-600 cm^{-1} region,[96-98] which would be indicative of an end-on configuration. Our spectroscopic findings align closely with the previous heme-PO model complex, [(TMPIm)Fe^{III}(O$_2^{2-}$)]$^-$ (TMPIm = 3-Imidazol-1-ylmethyl-N-{2-[10,15,20-tris-(2,4,6-trimethyl-phenyl)-porphyrin-5-yl]-phenyl}-benzamidel),[95] which encompassed a covalently linked imidazole axial ligand, and was described as a seven-coordinate side-on heme-PO species with a high-spin (*S* = 5/2) ferric center (Table S1).[95]

The high-spin nature of the axially ligated heme-PO adduct, [(4-MeIm)(TPP)Fe^{III}(O$_2^{2-}$)]$^-$, contrasts with heme/copper peroxo adducts of cytochrome *c* oxidase model compounds, where the addition of axial ligands (e.g., DCHIm) flips the spin state of the heme iron center from high-spin to low-spin, with the concomitant interconversion of side-on bound peroxo moiety (with respect to heme) to end-on.[99] Nonetheless, these differences should be viewed within the caveat that the copper(II) center in those model systems presumably imparts a significant "pull effect", which is absent in heme-only systems. This phenomenon has also been discussed by Naruta and co-workers,[98] where *both* heme (1) secondary sphere interactions (i.e., "pull effect"), as well as (2) axial ligation/donation ("push effect") were deemed to play a key role in the formation of truly end-on low-spin heme-PO adducts (Table S1). This finding nicely complements the analogous biological systems, where the intricate interplay between the primary and secondary

coordination sphere fine-tunes the salient geometric and electronic parameters vital for their functionality.[1] Moreover, in previous heme-PO models with tethered axial ligands (i.e., TMPIm *vs* F_8TPPIm (or P^{Im})), the spin state of the iron center was observed to be influenced by the electronic properties of the *meso*-substituents, wherein electron-donating groups gave rise to high-spin peroxo complexes,[95] while electron-deficient *meso*-substituents have predominantly led to low-spin systems (Table S1).[97] Despite the lack of large perturbations in the peroxo binding mode of $[(4\text{-MeIm})(TPP)Fe^{III}(O_2^{2-})]^-$, sizable electronic modifications within the heme peroxo moiety were clearly evident in NMR spectroscopy. The pyrrole-position deuterated TPP-d_8 porphyrinate system was utilized to evaluate these heme-PO systems by ^{2}H NMR spectroscopy, where the parent heme-PO adduct, $[(THF)(TPP\text{-}d_8)Fe^{III}(O_2^{2-})]^-$, exhibited a single ^{2}H NMR feature at $\delta_{pyrrole}$ = 38.5 ppm. This feature completely shifted upfield to $\delta_{pyrrole}$ = 9.1 ppm (Figure 2C) upon axial ligation of 4-MeIm. Similar changes in NMR were also observed upon 4-DMAP and DCHIm ligation, where the final ^{2}H NMR features were observed at $\delta_{pyrrole}$ = 12.5 ppm and 9.0 ppm, respectively (Figure S4). Given the relevance of proximal thiolate ligation in NOS, we also utilized strongly-donating thiophenolate as an axial ligand (Scheme 1), where the electronic absorption features of $[(ArS^-)(TPP)Fe^{III}(O_2^{2-})]^{2-}$ were centered at 436 nm (Soret; ε = 2.5×10^5 M^{-1}cm^{-1}) and 564 nm (ε = 1.6×10^4 M^{-1}cm^{-1}; Figure S5A). Intriguingly, attributes of $[(ArS^-)(TPP)Fe^{III}(O_2^{2-})]^{2-}$ was observed to be somewhat unique, exhibiting EPR spectroscopic features consistent with a mixture of high- and low-spin ferric sites. As shown in Figure S5B, two high spin ferric sites (S = 5/2) can be identified at low field. The sharp feature at g ~ 6 (■) represents the $g_\perp$-region of a near axial (E/D = 0.005) heme site. This feature is most prominent at low temperature as this resonance originates from the ground doublet of a S = 5/2 manifold. The second transition observed at g ~ 4.2 (□) is attributed to a highly rhombic (E/D = 0.27) high-spin ferric site. This signal originates from a transition within the middle doublet of the S = 5/2 spin system. Consequently, the decrease in its signal intensity with increasing temperature is much less pronounced relative to the axial site. The temperature dependent signal intensity is diagnostic of the Boltzmann population distribution for each doublet. Therefore, the magnitude of the axial zero field splitting parameter (D) was determined for both species by matching the simulated and experimental signal intensity observed across multiple temperatures between 4 and 20 K (Figure S5B). Among the other spectroscopic parameters provided in Table S2, the D-values for the axial (■) and rhombic (□) high-spin ferric sites were determined to be 8.0 ± 1.0 and 0.9 ± 0.1 cm^{-1}, respectively. Notably, the high-spin axial EPR signature at g ~ 6 (■) parallels previous reports describing heme ferric hydroxide species, and the rhombic g ~ 4.2 (□) is the starting heme peroxo complex. Taking this into consideration, we can state that the parent heme peroxo complex accounts for over 30% of the observed iron whereas the ferric hydroxide species accounts for less than 4%. The two rhombic signals near g ~ 2 are consistent with low-spin (S = 1/2) ferric sites (Figure S5B), which originate from the low-spin heme peroxo complex (●; g = 2.28, 2.13, and 1.97; Table S1 and *vide infra*) and its decay product (○; g = 2.46, 2.03, 1.91),[95] where the former accounts for 40% of the observable iron in the sample. This speciation observed in EPR of $[(ArS^-)(TPP)Fe^{III}(O_2^{2-})]^{2-}$ reflects the high reactivity of this complex. Thus, we infer that the donor ability of axial ligands is key, wherein the superior donor in the series, ArS^-, results in the strongest ligand-field at the heme iron center, accordingly resulting in an equilibrium mixture of high-spin and low-spin heme-PO species.

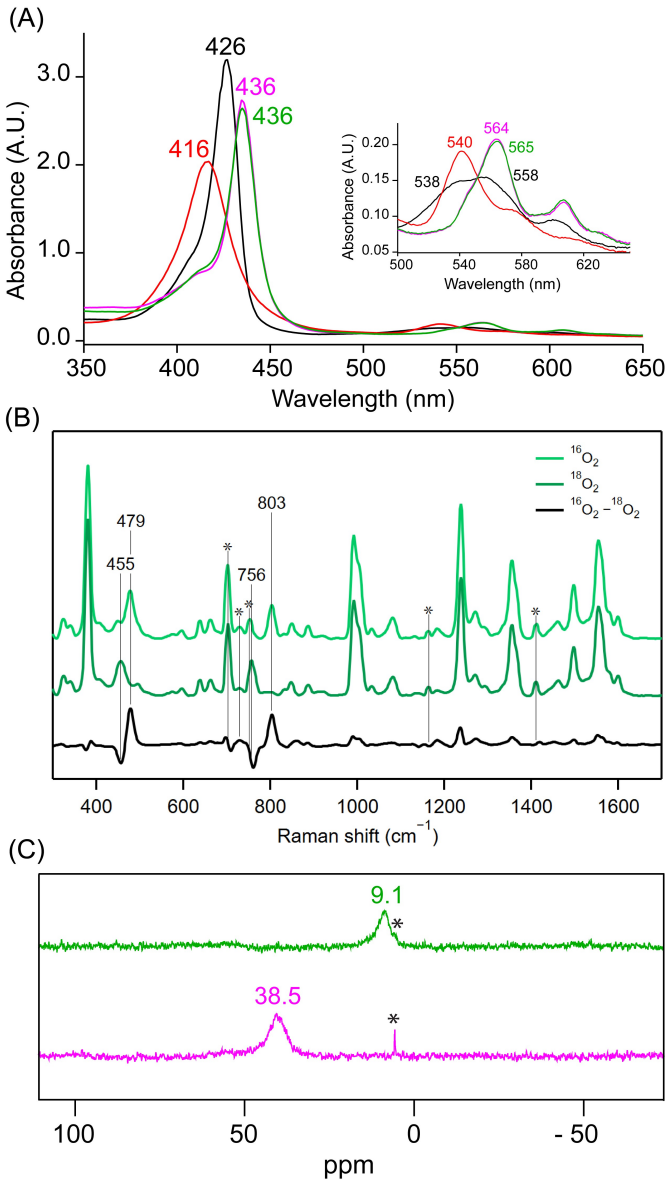

Figure 2. (A) UV–vis spectra (in 9:1 DCM:THF at −40 °C) for 50 μM solutions of $[(THF)_2(TPP)Fe^{II}]$ (black), $[(THF)(TPP)Fe^{III}(O_2^{-\bullet})]$ (red), $[(THF)(TPP)Fe^{III}(O_2^{2-})]^-$ (pink), and $[(4\text{-MeIm})(TPP)Fe^{III}(O_2^{2-})]^-$ (green). Inset shows the expanded Q-band region. (B) Resonance Raman spectra (λ_{ex}= 457 nm) collected for a 2 mM 9:1 DCM:THF frozen solution sample of $[(4\text{-MeIm})(TPP)Fe^{III}(O_2^{2-})]^-$ prepared with $^{16}O_{2(g)}$ (light green) and $^{18}O_{2(g)}$ (dark green); the difference spectrum is shown in black. (C) ^{2}H NMR spectra (in 9:1 DCM:THF at −40 °C) for $[(THF)(TPP\text{-}d_8)Fe^{III}(O_2^{2-})]^-$ (pink), and $[(4\text{-MeIm})(TPP\text{-}d_8)Fe^{III}(O_2^{2-})]^-$ (green); *peaks correspond to the solvent.

Resonance Raman characterization of $[(ArS^-)(TPP)Fe^{III}(O_2^{2-})]^{2-}$ is consistent this finding, where the isotope-sensitive ν(Fe–O)

View Article Online
DOI: 10.1039/D4SC08701A

feature was observed at 484 cm^{-1} ($\Delta^{18}O_2$ = –21 cm^{-1}) (Figure S3B), indicative of greater Fe-O interaction when compared to the parent THF-bound species. In further support of relative increases in Fe-O bond strength, the ν(Fe–O) features of $[(ArO^-)(TPP)Fe^{III}(O_2^{2-})]^{2-}$ and $[(ArO^-)(F_{20}TPP)Fe^{III}(O_2^{2-})]^{2-}$ were observed at 474 ($\Delta^{18}O_2$ = –23) cm^{-1} and 492 ($\Delta^{18}O_2$ = –18) cm^{-1}, respectively. Unfortunately for spectroscopic characterization purposes, the addition of anionic axial ligands destabilizes the peroxo adducts, preventing the precise assignment of their isotope-sensitive ν(O–O) bands (Figure S3B-D). This trend in axial ligand donor abilities clearly dictates the observed second-order reaction rates of corresponding heme-PO adducts (*vide-infra*), where stronger axial donors lead to more nucleophilic peroxo units, and thereby resulting in faster reaction rates.

Oxime Oxidation Reactivities of Axially Ligated Heme Peroxo Adducts

Our recent work has demonstrated that heme-PO intermediates can oxidize oxime substrates leading to the corresponding ketone with the simultaneous production of nitroxide anion (i.e., NO^-), which marks the only functional heme model for the second mechanistic step of NOS.[92] In this work, we set out to interrogate how this unique reactivity between heme-PO adducts and the oxime is modulated by the ligation of aforementioned axial ligands, and thereby define how key reactivity parameters are altered accordingly. Thus, we carried out rigorous reactivity studies into the nucleophilic reactivities of a series of $[(B)(TPP)Fe^{III}(O_2^{2-})]^-$ adducts (where B = axially coordinated ligands shown in Scheme 1), with acetophenone oxime as the NHA mimic substrate. When 200 equiv of acetophenone oxime was introduced into a 50 µM solution of $[(4\text{-MeIm})(TPP)Fe^{III}(O_2^{2-})]^-$ in 9:1 DCM:THF at –40 °C, prominent changes in electronic absorption were observed from 436 to 421 nm (Soret; ε = 1.4×10^5 $M^{-1}cm^{-1}$) and 565 to 550 nm (ε = 2.5×10^3 $M^{-1}cm^{-1}$; Figures 3A). The final heme product of this reaction was characterized to be the corresponding six-coordinate heme ferric hydroxo adduct, $[(4\text{-MeIm})(TPP)Fe^{III}(OH)]$ (Figure 3A). When other axial ligands were employed, the final heme species was observed to be the five-coordinate heme ferric hydroxo adduct, $[(TPP)Fe^{III}(OH)]$ (Figure 3B & S6). Spectroscopic features of the five-coordinate $[(TPP)Fe^{III}(OH)]$ final species are in close agreement with those of an authentic standard reported previously (Figure S7).[92] EPR spectroscopy confirms the low-spin rhombic ferric center of $[(4\text{-MeIm})(TPP)Fe^{III}(OH)]$ with features centered at g = 2.38, 2.17 and 1.90 (Figure S8A). ^{2}H NMR analysis of this $[(4\text{-MeIm})(TPP\text{-}d_8)Fe^{III}(OH)]$ final product resulted in a single resonance at $\delta_{pyrrole}$= –18 ppm (Figure S8B). These characterization details are in excellent agreement with those of an authentically prepared standard of $[(4\text{-MeIm})(TPP\text{-}d_8)Fe^{III}(OH)]$ (Figure S9), further solidifying its identity. The final organic product, acetophenone, was characterized via ^{1}H NMR and GC-MS (Figure S10 and S11A), revealing a yield of ~34%. $[(4\text{-DMAP})(TPP)Fe^{III}(O_2^{2-})]^-$ and $[(ArO^-)(TPP)Fe^{III}(O_2^{2-})]^{2-}$ resulted in similar acetophenone yields of 34% and 37%, respectively (Figure S11B). Notably, these yields of acetophenone are comparable to those observed for the parent heme-PO complex under identical reaction conditions.[92] Finally, the formation of nitroxide (NO^-) was determined by carrying out oxime oxidation in the presence of an excess of PPh_3,[88, 92] where LC-MS analysis confirmed the formation of both triphenylphosphine oxide (O=PPh_3; ~20% yield (Figures S12B and S12C)) and triphenylphosphine aza-ylide (HN=PPh_3; Figure S12A).

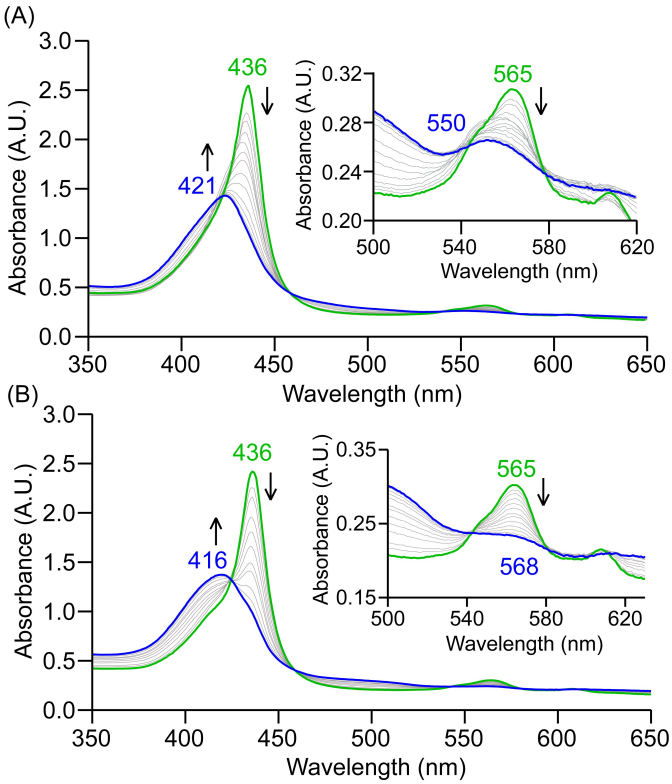

Figure 3. (A) Electronic absorption spectral changes observed (in 9:1 DCM: THF at –40 °C) during the reaction of a 50 µM solution of (A) $[(4\text{-MeIm})(TPP)Fe^{III}(O_2^{2-})]^-$ and (B) $[(4\text{-DMAP})(TPP)Fe^{III}(O_2^{2-})]^-$ with 200 equiv of acetophenone oxime (green: initial six coordinate heme-PO complex; blue: final ferric product). Insets show the expanded Q-band regions, and arrows indicate the direction of peak transition.

In light of our previous findings describing an initial nucleophilic attack mediated by the heme-PO adduct on oxime substrate being rate-limiting, one would expect axially ligated heme-PO adducts to mediate oxime oxidation reactions much faster compared to their parent peroxo compound (i.e., with only weak solvent ligation).[35] To test this hypothesis, we carried out kinetic analysis into acetophenone oxime oxidation reactions facilitated by the series of $[(B)(TPP)Fe^{III}(O_2^{2-})]^-$ adducts. In that, the pseudo-first-order kinetic rates were computed upon the addition of 200–500 equiv of the substrate in DCM:THF 9:1 at –40 °C. In all cases, the reaction rates (k_{obs}) were observed to increase linearly as a function of substrate concentration (Figure S13), indicating the rate-limiting nature of initial heme-PO attack on the oxime substrate. Hence, the reaction mechanism presumably remains unaltered as compared with the parent heme-PO adduct. Nonetheless, the second-order kinetic rates (k_2) resulting from these studies illustrated an unequivocal relationship with the axial ligand donor abilities,

View Article Online
DOI: 10.1039/D4SC08701A

wherein the stronger anionic donor ligands led to faster oxime oxidation rates (Table 1). Particularly, the neutral axial ligands, 4-MeIm, DCHIm, and 4-DMAP (Scheme 1), wherein the donor abilities are known to increase in the same order, exhibited second-order oxime oxidation reaction rates of 0.79±0.06, 0.87±0.02, and 1.11±0.08 $M^{-1}s^{-1}$, respectively (Figure S13). Interestingly, all of these rates are faster than that of the parent heme-PO adduct reported under identical conditions (0.26±0.01 $M^{-1}s^{-1}$). When anionic axial ligands, ArO^- and ArS^- (Scheme 1) were utilized, these rates escalated even further, up to 1.45±0.07 and 1.53±0.04 $M^{-1}s^{-1}$, respectively (Figure S13). Thus, the strongest axial donor within the series, ArS^- (soft base) most enhanced the nucleophilicity of the heme-PO moiety, resulting in the fastest oxime oxidation reaction within the series.

Table 1. A comparison of second-order rate constants (k_2) for $[(B)[(TPP)Fe^{III}(O_2^{2-})]^-$ at −40 °C and the pK_a values of conjugate acids of B ligands.

Axial Ligand (B)	pK_a of conjugate acid	Second Order Rate (k_2 in $M^{-1}s^{-1}$)	Ref.
THF	-2.05	0.26±0.01	100
4-MeIm	7.12	0.79±0.06	101
DCHIm	7.67	0.87±0.02	102
4-DMAP	9.7	1.11±0.08	103
ArO^-	9.3	1.45±0.07	104
ArS^-	6.5	1.53±0.04	105

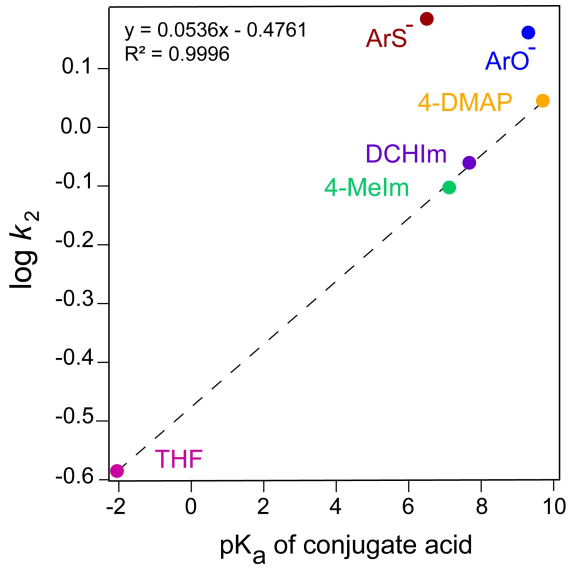

Figure 4. The correlation between log k_2 values for $[(B)(TPP)Fe^{III}(O_2^{2-})]^-$ mediated acetophenone oxime oxidation reactions (in 9:1 DCM:THF at –40 °C) and the p*K*a values of conjugate acids of the axially ligating B ligands, where B = THF (magenta), 4-MeIm (green), DCHIm (purple), 4-DMAP (orange), ArO^- (blue) and ArS^- (brick red).

This "push effect" of the axial ligand can be further clarified in terms of the orbital overlap between the donor and the acceptor (i.e., axial ligand and Fe center, respectively).[106] Metal-ligand interactions can be either σ, π, or a combination of both in nature, and the pK_a of the conjugate acid provides a reasonable handle for surveying the extent of σ-donation resulting from a given ligand. The observed increase in oxime oxidation rates in this case show a nice correlation with the corresponding pK_a values of the axially ligating neutral (i.e., only σ-donor) ligands (Figure 4 and Table 1). Moreover, the anionic axial ligands have π-donor properties as well, where the lone pairs on the donor atom (i.e., O and S in ArO^- and ArS^-, respectively) can be donated to the metal center via a p_x-d_π type overlap (Figure 4; Figure S13 and Table 1).[107] Our theoretical analysis lends credence to such a π-donation from the thiophenolate axial ligand, where it employs an orientation (with respect to the heme ring) that maximizes a p_x-d_π type overlap, while minimizing steric interactions with the *meso*-phenyl substituents on heme (Figure 7; *vide infra*). Variable temperature kinetic (Eyring) analysis for acetophenone oxime oxidation by the parent heme-PO, $[(THF)(TPP)Fe^{III}(O_2^{2-})]^-$, as well as the axially ligated heme-PO adducts, $[(4\text{-}MeIm)(TPP)Fe^{III}(O_2^{2-})]^-$ and $[(ArO^-)(TPP)Fe^{III}(O_2^{2-})]^{2-}$, was then conducted in a 9:1 DCM:THF solvent mixture (Figure S14). Evidently, both enthalpy and entropy of activation (i.e., $\Delta H^{\neq}$ and $\Delta S^{\neq}$) increase upon axial ligation of 4-MeIm and ArO^- to $[(TPP)Fe^{III}(O_2^{2-})]^-$ (Figures 5 and S15). A similar study was recently conducted for a Cmpd-I analog, where axial ligation of an anionic cyanide ligand led to more positive $\Delta S^{\neq}$ and lowered $\Delta H^{\neq}$ values, ultimately resulting in a diminished activation barrier when compared to its five-coordinate analog toward oxygen atom transfer substrates.[108]

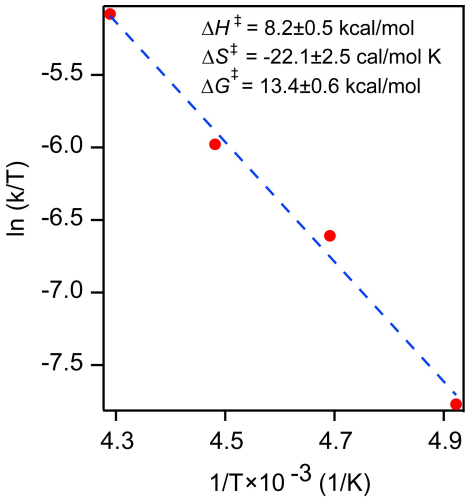

Figure 5. Eyring analysis data showing the dependence of ln(k/T) on 1/T for the reaction between a 50 μM solution of $[(ArO^-)(TPP)Fe^{III}(O_2^{2-})]^{2-}$ and acetophenone oxime at −40, −50, −60 and -70 °C. Solvent = 9:1 DCM:THF.

Electronic Structure Characterization of Axially Ligated Heme-PO Adducts

Given the significant reactivity perturbations observed in heme-PO adducts upon axial ligation, we investigated whether such modifications could be utilized to 'turn-on' the nucleophilic reactivity of an otherwise inert,[35, 92] electron-deficient heme-PO adduct, $[(THF)(F_{20}TPP)Fe^{III}(O_2^{2-})]^-$ (where $F_{20}TPP$ = 5,10,15,20-tetra(pentafluorophenyl)porphyrin). To this end, we prepared various axially ligated $[(B)(F_{20}TPP)Fe^{III}(O_2^{2-})]^-$ complexes, where

View Article Online
DOI: 10.1039/D4SC08704A

B = 4-MeIm, DCHIm, 4-DMAP, ArS^- (Figure S16). Interestingly, EPR investigations into this series revealed that the [(4-MeIm)(F_{20}TPP)$Fe^{III}(O_2^{2-})$]$^-$ adduct maintains its rhombic high-spin iron center even after the axial ligation of 4-MeIm (Figure S17A). In contrast, the neutral yet stronger donor ligands, 4-DMAP and DCHIm, as well as the anionic ArS^- all led to a mixture of two distinct high-spin and low-spin species as observed by EPR (Figures S17B, S17C, and 6A). Both low field transitions observed in Figure 6A (i.e., for [(ArS^-)(F_{20}TPP-d_8)$Fe^{III}(O_2^{2-})$]$^{2-}$) can be attributed to the high-spin side-on Fe(III)-η^2-peroxo species. Accordingly, the weak resonance observed at g ~ 9.2 and the intense signal at 4.2 are assigned to transitions within the ground and middle doublet of a S = 5/2 spin manifold, respectively. In the absence of inter-doublet mixing, the observed position of these g-values is consistent with a highly rhombic zero-field splitting (E/D ~ 0.24) term. As the side-on (η^2) coordination of the peroxo ligand is expected to have considerable overlap with Fe(III) d_p-orbitals (d_{xz} and d_{yz}), the high rhombicity of [(ArS^-)(F_{20}TPP-d_8)$Fe^{III}(O_2^{2-})$]$^{2-}$ is not unexpected.[109-112] Indeed, similar rhombicity and high-spin electronic configuration appears to be a shared characteristic among crystallographically and spectroscopically characterized Fe(III)-η^2-peroxo complexes.[95, 113] Similar to the aforementioned EPR characterization of [(ArS^-)(TPP)$Fe^{III}(O_2^{2-}$)]$^{2-}$, the axial zero-field splitting term for the high-spin fraction of [(ArS^-)(F_{20}TPP-d_8)$Fe^{III}(O_2^{2-})$]$^{2-}$ (D = 0.6 ± 0.1 cm^{-1}) was obtained by simultaneous simulation of EPR spectra collected at temperatures ranging from 4 to 20 K (Figure S18). Within this temperature regime, EPR simulations faithfully reproduce the relative intensity of transitions within the ground and first excited state. The quantitative simulations (Figure 6A, *Sim*) indicate that the high-spin ferric site accounts for 82% of the observable spin concentration (i.e., ~1.6 mM). The low-spin (S = 1/2) [(ArS^-)(F_{20}TPP-d_8)$Fe^{III}(O_2^{2-})$]$^{2-}$ complex has nearly axial symmetry, with observed g-values of 2.31, 2.29, and 1.92. Analytical simulations of the low-spin Fe(III)-site account for ~18% of the observed spin concentration (0.4 mM). Relative to the rhombic g-values observed for the low-spin side-on peroxo complexes produced with TPP (2.28, 2.13, and 1.97), the axial g-values observed for [(ArS^-)(F_{20}TPP-d_8)$Fe^{III}(O_2^{2-})$]$^{2-}$ suggest a change in the F_{20}TPP ligand field strength, thereby altering the relative energies of Fe(III) t_{2g} d-orbitals.[114-116] This is consistent with the differing D-values measured for the high-spin Fe(III)-η^2-peroxo species for TPP and F_{20}-TPP. The ^{2}H NMR spectrum of [(THF)(F_{20}TPP-d_8)$Fe^{III}(O_2^{2-})$]$^-$ in DCM:THF 9:1 at –40 °C exhibited a single feature at $\delta_{pyrrole}$ = 38.7 ppm, which shifted upfield to $\delta_{pyrrole}$ = 8.8 ppm upon ligation of 4-MeIm (Figure S19). On the contrary, [(ArS^-)(F_{20}TPP-d_8)$Fe^{III}(O_2^{2-})$]$^{2-}$ indicated a mixture of ^{2}H NMR features at $\delta_{pyrrole}$ = 38.7 and -2.1 ppm (Figure 6B), which closely parallels our EPR characterization. Furthermore, such $\delta_{pyrrole}$ ^{2}H NMR features below 0 ppm are indicative of low-spin heme ferric systems, as described in our previous work.[10] These findings, therefore, suggest clear 'activation' of the electron-deficient heme-PO adduct upon the ligation of strong axial donor ligands. Oxime oxidation reactivity studies of this series of [(B)(F_{20}TPP)$Fe^{III}(O_2^{2-})$]$^-$ adducts nicely echo our spectroscopy-based interpretation, where [(4-MeIm)(F_{20}TPP)$Fe^{III}(O_2^{2-})$]$^-$ was found to be inert toward acetophenone oxime, while both [(DCHIm)(F_{20}TPP)$Fe^{III}(O_2^{2-})$]$^-$ and [(ArS^-)(F_{20}TPP)$Fe^{III}(O_2^{2-})$]$^{2-}$ reacted (Figure S20), with the latter leading to a reaction rate of 0.03 s^{-1} at –40 °C with 500 equiv of substrate (Figure S20B). Similar 'turn-on' of reactivity of [(F_{20}TPP)$Fe^{III}(O_2^{2-})$]$^-$ has previously been reported by Valentine and co-workers with regard to alkene epoxidation reactivity, where axial ligation of DMSO solvent was postulated.[35]

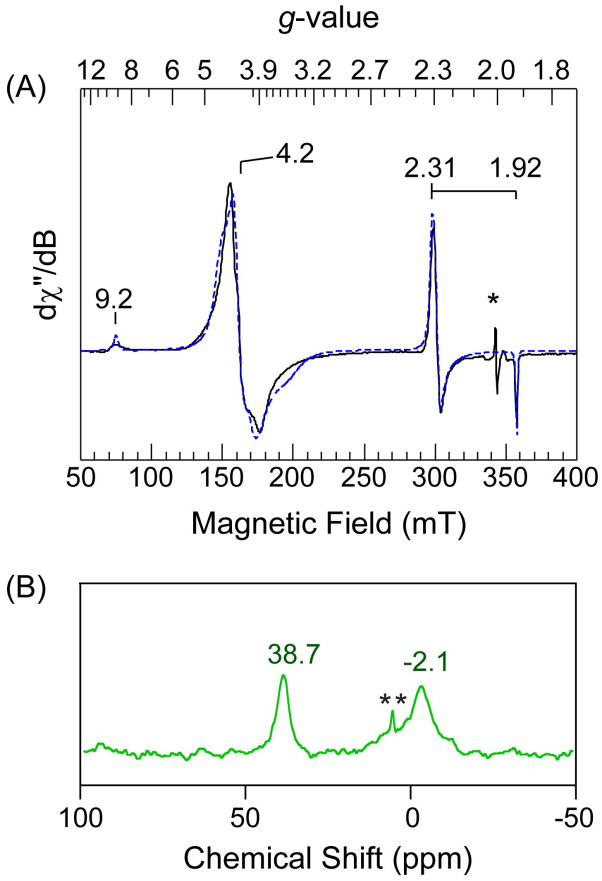

Figure 6. (A) 7 K CW EPR spectra of [(ArS^-)(F_{20}TPP)$Fe^{III}(O_2^{2-})$]$^{2-}$ (2 mM) dissolved in 9:1 DCM:THF (light green), and quantitative EPR simulations for high- and low-spin ferric sites (*Sim; dashed blue*). The isotropic feature (*) at g ~ 2 is from residual (< 1 μM) cobaltacene. (B) ^{2}H NMR spectrum (in 9:1 DCM:THF at –40 °C) for [(ArS^-)(F_{20}TPP-d_8)$Fe^{III}(O_2^{2-})$]$^{2-}$ indicating the presence of both high- and low-spin heme-PO adducts (**peaks correspond to the solvent).

View Article Online
DOI: 10.1039/D4SC06701A

Table 2. Experimentally and Theoretically Determined Properties of [(THF)(TPP)$Fe^{III}(O_2^{2-})$]$^-$, [(4-MeIm)(TPP)$Fe^{III}(O_2^{2-})$]$^-$, and [(ArS^-)(TPP)$Fe^{III}(O_2^{2-})$]$^{2-}$.

	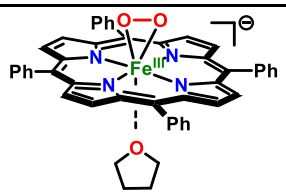	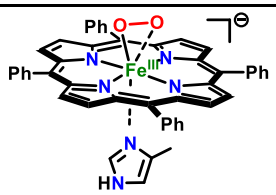	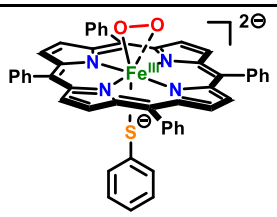
UV-vis[a]	436, 565	436, 565	436, 564
EPR[b]	4.2	4.2	4.2 & 2.28, 2.13, 1.97
^{2}H NMR[c]	38.5	9.1	-
rRaman[d]	ν(Fe–O) 472 (Δ^{18}O = -21) ν(O–O) 807 (Δ^{18}O = -44)	ν(Fe–O) 479 (Δ^{18}O = -23) ν(O–O) 803 (Δ^{18}O = -47)	ν(Fe–O) 484 (Δ^{18}O = -21)
Fe–O length[e]	1.978	1.968	1.898
rRaman (DFT)[d]	ν(Fe–O) 407 (Δ^{18}O = -14) ν(O–O) 899 (Δ^{18}O = -52)	ν(Fe–O) 414 (Δ^{18}O = -15) ν(O–O) 896 (Δ^{18}O = -51)	ν(Fe–O) 465 (Δ^{18}O = -14) ν(O–O) 1015 (Δ^{18}O = -63)
k_2[f]	0.26±0.01	0.79±0.06	1.53±0.04
$\Delta H^{\neq}$[g]	7.6±0.7	9.0±0.9	-
$\Delta S^{\neq}$[h]	-27.7±3.0	-20.2±3.8	-
$\Delta G^{\neq}$[m]	14.0±0.8	13.7±1.2	-

[a] λ_{max} values in nm; [b] g_{app}-values measured at 7 K; [c] $\delta_{pyrrole}$ chemical shifts (in ppm) in 9:1 DCM:THF at - 40 °C; [d] in cm^{-1} at 77 K; [e] computed with DFT shown in Å; [f] in M^{-1} s^{-1} at –40 °C; [g] in kcal mol^{-1}; [h] in cal K^{-1} mol^{-1}; [m] in kcal mol^{-1} at -40 °C.

Computational Studies

To further clarify the precise geometric and electronic modifications imposed on heme-PO adducts upon axial ligand coordination, we carried out theoretical investigations using Density Functional Theory (DFT). Therein, optimized ground state geometries of [(THF)(TPP)$Fe^{III}(O_2^{2-})$]$^-$, and a series of axially ligated [(B)(TPP)$Fe^{III}(O_2^{2-})$]$^-$ complexes (where B = THF, 4-MeIm, ArO^- or ArS^-; see Figures 7 and S21) over three spin surfaces (S = 5/2, 3/2, 1/2) were probed. Figure S22 illustrates all spin state energies organized with respect to the energy of the S = 5/2 spin state in each case. For the parent peroxo species, [(THF)(TPP)$Fe^{III}(O_2^{2-})$]$^-$, the high-spin complex (i.e., S = 5/2) was found to be the clear ground state.[117] Importantly, the calculated ground states for the axially ligated heme-PO complexes varied depending on the extent of σ- and/or π-donation from the axial ligand. In that, the neutral axial ligands (THF, 4-MeIm) were found to only weakly interact with the heme center (Fe•••O_{THF} and Fe•••N_{Im} distances of 4.4 and 3.2 Å, respectively). Regardless, the energy disparity between the high-spin (i.e., S = 5/2) and low-spin (i.e., S = 1/2) states decreased dramatically upon the ligation of those axial ligands. For example, in the case of 4-MeIm, the high-spin state remains the ground state, however, the difference in energy for the high- and low-spin states shrinks to ~2.9 kcal/mol (i.e., from ~16.3 kcal/mol for [(THF)(TPP)$Fe^{III}(O_2^{2-})$]$^-$). With anionic ligands, the low-spin state becomes slightly more favored, and for [(ArS^-)(TPP)$Fe^{III}(O_2^{2-})$]$^{2-}$ the gap is only -1.8 kcal/mol, supporting its experimentally observed equilibrium mixture of high- and low-spin Fe-species.

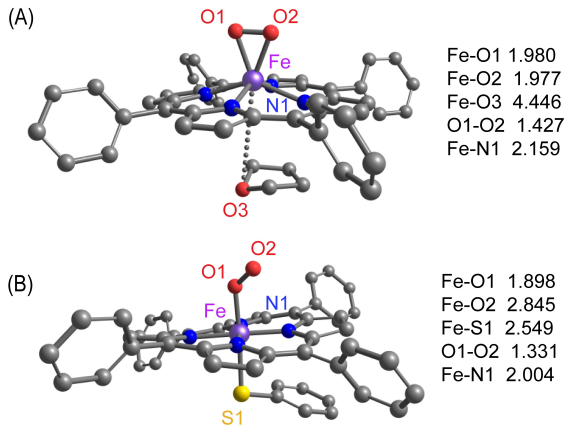

Figure 7. Optimized geometries of (A) [(THF)(TPP)$Fe^{III}(O_2^{2-})$]$^-$, and (B) [ArS^- (TPP)$Fe^{III}(O_2^{2-})$]$^{2-}$ with calculated bond lengths shown in Å.

The trend in theoretically estimated Fe–O_{peroxo} bond lengths aligns well with the experimentally predicted (i.e., by resonance Raman data; Table 2), where ligation of 4-MeIm was observed to result in a shorter Fe-O_{peroxo} bond compared to the parent complex (1.968 Å vs. 1.978 Å, respectively; see Table S4[118]). This change in bond length is accompanied by a minor decrease in the natural atomic charge at the iron center from 0.937 to 0.929 upon 4-MeIm coordination. Moreover, the trend in theoretically predicted ν(Fe–O) and ν(O–O) Raman stretching frequencies for the parent peroxo complex, [(THF)(TPP)$Fe^{III}(O_2^{2-})$]$^-$, and [(4-MeIm)(TPP)$Fe^{III}(O_2^{2-})$]$^-$ are in agreement with the experimental observations (i.e., increased and decreased

View Article Online
DOI: 10.1039/D4SC08701A

ν(Fe–O) and ν(O–O) frequencies, respectively; Tables 2 and S5). Furthermore, the calculated ^{18}O isotope shifts, for ν(Fe–O) and ν(O–O), respectively, are in line with experimental observations (Table 2).

Our experimental (*vide supra*) and theoretical findings therefore in concert illustrate that upon ligating of anionic axial ligands, the accessibility of the low-spin heme-PO adducts increases. The calculated Fe–O_{peroxo} bond lengths for [(ArO$^-$)(TPP)Fe^{III}(O_2^{2-})]$^{2-}$ and [(ArS$^-$)(TPP)Fe^{III}(O_2^{2-})]$^{2-}$ were shorter compared to other complexes, measuring up to 1.875 Å and 1.898 Å, respectively (Table S4). This shortening of the Fe–O_{peroxo} bond is further corroborated by the higher Fe–O_{peroxo} Raman stretching frequencies observed/computed for [(ArO$^-$)(TPP)Fe^{III}(O_2^{2-})]$^{2-}$ and [(ArS$^-$)(TPP)Fe^{III}(O_2^{2-})]$^{2-}$ (Figure S3; Tables 2 and S5). However, though our theoretical predictions suggest the formation of end-on heme-PO adducts upon anionic axial ligation, we see no experimental evidence to support that notion. For example, we see no evidence for an isotope-sensitive Fe-O feature within the 550-600 cm^{-1} region in resonance Raman that would be indicative of an end-on peroxo species. Nonetheless, we do observe increased decomposition products upon the addition of anionic ligands to the peroxo adducts (*vide supra*), and whether those result from a highly reactive but destabilized end-on peroxo adduct is unclear. Moreover, the enhanced electron-donation by these anionic ligands is evident by the dramatic decrease in the natural atomic charge of the iron center upon their ligation (0.214 and 0.047 for phenolate and thiophenolate, respectively, compared to 0.937 in the parent complex; see Table S4). To this end, this work unequivocally demonstrates the fundamental reasonings behind Nature evolutionarily favoring a thiolate proximal ligand for NOS oxygenase domain, which effectively enhances the feasibility of rate-limiting events of its second mechanistic step.

Conclusions

Herein, we conduct a detailed discussion into how the primary coordination sphere, especially the proximal heme ligation, modulates the nucleophilic reactivity patterns of heme-PO species, with relevance to their proposed reactivity landscape in the second mechanistic step of NOS. We utilized acetophenone oxime as an NHA substrate mimic, and surveyed its reactivity toward a series of electronically divergent heme-PO adducts with and without the axial ligation of bioinspired neutral and anionic ligands. Spectroscopic and theoretical characterization reveals that axial ligation leads to the formation of high-spin/low-spin mixtures, while the heme-PO structure remains bound side-on. In support, DFT interrogations reveal a trend in the energy gap between the high-spin (S = 5/2) and low-spin (S = 1/2) heme-PO species decreasing with increased axial ligand donor ability (i.e., the "push" effect). The lack of transition into a low-spin, end-on heme-PO merely upon axial ligation (i.e., the "push" effect) can be attributed to the absence of a non-covalently interacting (e.g., hydrogen bonding) secondary sphere in these systems (i.e., the "pull" effect). The nucleophilic reactivities of these heme-PO systems vary as expected with respect to their axial ligand donor abilities; that is, in the order of anionic axial ligands > neutral axial ligands > parent complex (Table 1), which supports the claim that heme-PO nucleophilic attack on the oxime substrate is rate-limiting. Moreover, the nucleophilically inert, electron-deficient heme-PO adduct, [(THF)(F_{20}TPP)Fe^{III}(O_2^{2-})]$^-$, could be competently activated toward oxime substrate oxidation upon the axial ligation of bioinspired anionic ligands. Variable temperature kinetic (Eyring) analyses of these systems illustrate that upon axial ligation both $\Delta H^{\neq}$ and $\Delta S^{\neq}$ increase for the oxime oxidation reaction (Table 2). This study, therefore, marks the first instance where modulation of kinetic and thermodynamic parameters of heme-PO mediated nucleophilic reactivities with respect to proximal ligation has been clearly demonstrated, wherein pivotal structure-activity relationships can be elucidated. The distinct structure-activity relations described in this work will not only aid in comprehending relevant biological implications, but will also unveil new knowledge to be integrated into the rational design of novel (e.g., mechanism-based) drug targets.

Conflicts of interest

There are no conflicts to declare.

Data availability

The data supporting this article have been included as part of the Supplementary Information.

Acknowledgements

This work was supported by the National Science Foundation CAREER Award CHE-2045005 (to G.B.W.) G.B.W. also acknowledges The University of Alabama and The University of Alabama at Birmingham for startup funds, as well as the UAB FDGP program. S.R. would like to thank the Alabama EPSCoR Graduate Research Scholar Program. H.S.S. would like to acknowledge NIH GM128852 (to H.S.S. and Y.L.), and B.S.P. NIH 2R15GM117511-04 for support. The authors also thank Dr. Ken Belmore and Dr. Qiaoli Liang for assistance with ^{2}H NMR and mass spectrometry/LC-MS experiments. EPR experiments were performed at the UA Chemistry & Biochemistry facility. Computational investigations were made possible in part by the high-performance computing resources and technical support provided by the Alabama Supercomputer Authority.

Notes and references

1. T. L. Poulos, Heme Enzyme Structure and Function, *Chem. Rev.*, 2014, **114**, 3919-3962.
2. S. M. Adam, G. B. Wijeratne, P. J. Rogler, D. E. Diaz, D. A. Quist, J. J. Liu and K. D. Karlin, Synthetic Fe/Cu Complexes: Toward Understanding Heme-Copper Oxidase Structure and Function, *Chem. Rev.*, 2018, **118**, 10840-11022.

3. J. P. T. Zaragoza and D. P. Goldberg, in *Dioxygen-dependent Heme Enzymes*, eds. M. Ikeda-Saito and E. Raven, The Royal Society of Chemistry, 2018, vol. 13, pp. 3-36.
4. T. L. Poulos, The role of the proximal ligand in heme enzymes, *J. Biol. Inorg. Chem.*, 1996, **1**, 356-359.
5. J. Dawson, Probing structure-function relations in heme-containing oxygenases and peroxidases, *Science*, 1988, **240**, 433-439.
6. M. T. Green, J. H. Dawson and H. B. Gray, Oxoiron(IV) in Chloroperoxidase Compound II Is Basic: Implications for P450 Chemistry, *Science*, 2004, **304**, 1653-1656.
7. T. H. Yosca, J. Rittle, C. M. Krest, E. L. Onderko, A. Silakov, J. C. Calixto, R. K. Behan and M. T. Green, Iron(IV)hydroxide pK_a and the Role of Thiolate Ligation in C-H Bond Activation by Cytochrome P450, *Science*, 2013, **342**, 825-829.
8. X. Huang and J. T. Groves, Oxygen Activation and Radical Transformations in Heme Proteins and Metalloporphyrins, *Chem. Rev.*, 2018, **118**, 2491-2553.
9. P. Mondal and G. B. Wijeratne, Modeling Tryptophan/Indoleamine 2,3-Dioxygenase with Heme Superoxide Mimics: Is Ferryl the Key Intermediate?, *J. Am. Chem. Soc.*, 2020, **142**, 1846-1856.
10. P. Mondal, I. Ishigami, E. F. Gérard, C. Lim, S.-R. Yeh, S. P. de Visser and G. B. Wijeratne, Proton-coupled electron transfer reactivities of electronically divergent heme superoxide intermediates: a kinetic, thermodynamic, and theoretical study, *Chem. Sci.*, 2021, **12**, 8872-8883.
11. G. B. Tolbert, S. B. Jayawardana, Y. Lee, J. Sun, F. Qu, L. M. Whitt, H. Shafaat and G. B. Wijeratne, Secondary Sphere Lewis Acid Activated Heme Superoxo Adducts Mimic Crucial Non-Covalent Interactions in IDO/TDO Heme Dioxygenases, *Chem. Eur. J.*, 2024, **n/a**, e202402310.
12. M. Sono, M. P. Roach, E. D. Coulter and J. H. Dawson, Heme-Containing Oxygenases, *Chem. Rev.*, 1996, **96**, 2841-2888.
13. A. P. Hunt, S. Samanta, M. R. Dent, M. W. Milbauer, J. N. Burstyn and N. Lehnert, Model Complexes Elucidate the Role of the Proximal Hydrogen-Bonding Network in Cytochrome P450s, *Inorg. Chem.*, 2020, **59**, 8034-8043.
14. M. Couture, S. Adak, D. J. Stuehr and D. L. Rousseau, Regulation of the Properties of the Heme-NO Complexes in Nitric-oxide Synthase by Hydrogen Bonding to the Proximal Cysteine *, *J. Biol. Chem.*, 2001, **276**, 38280-38288.
15. J. Lang, J. Santolini and M. Couture, The Conserved Trp–Cys Hydrogen Bond Dampens the “Push Effect” of the Heme Cysteinate Proximal Ligand during the First Catalytic Cycle of Nitric Oxide Synthase, *Biochemistry*, 2011, **50**, 10069-10081.
16. J. Tejero, A. Biswas, Z.-Q. Wang, R. C. Page, M. M. Haque, C. Hemann, J. L. Zweier, S. Misra and D. J. Stuehr, Stabilization and Characterization of a Heme-Oxy Reaction Intermediate in Inducible Nitric-oxide Synthase, *J. Biol. Chem.*, 2008, **283**, 33498-33507.
17. M. Aarabi, R. Omidyan, S. Soorkia, G. Grégoire, M. Broquier, M.-E. Crestoni, A. de la Lande, B. Soep and N. Shafizadeh, The dramatic effect of *N*-methylimidazole on trans axial ligand binding to ferric heme: experiment and theory, *Phys. Chem. Chem. Phys.*, 2019, **21**, 1750-1760.
18. P. K. Das, S. Chatterjee, S. Samanta and A. Dey, EPR, Resonance Raman, and DFT Calculations on Thiolate- and Imidazole-Bound Iron(III) Porphyrin Complexes: Role of the Axial Ligand in Tuning the Electronic Structure, *Inorg. Chem.*, 2012, **51**, 10704-10714.
19. A. P. Green, T. Hayashi, P. R. E. Mittl and D. Hilvert, A Chemically Programmed Proximal Ligand Enhances the Catalytic Properties of a Heme Enzyme, *J. Am. Chem. Soc.*, 2016, **138**, 11344–11352.
20. R. Perera, M. Sono, H. L. Voegtle and J. H. Dawson, Molecular basis for the inability of an oxygen atom donor ligand to replace the natural sulfur donor heme axial ligand in cytochrome P450 catalysis. Spectroscopic characterization of the Cys436Ser CYP2B4 mutant, *Arch. Biochem. Biophys.*, 2011, **507**, 119-125.
21. S. Samanta, P. K. Das, S. Chatterjee and A. Dey, Effect of axial ligands on electronic structure and O_2 reduction by iron porphyrin complexes: Towards a quantitative understanding of the "push effect", *J. Porphyr. Phthalocya.*, 2015, **19**, 92-108.
22. M. P. Roach, A. E. Pond, M. R. Thomas, S. G. Boxer and J. H. Dawson, The Role of the Distal and Proximal Protein Environments in Controlling the Ferric Spin State and in Stabilizing Thiolate Ligation in Heme Systems: Thiolate Adducts of the Myoglobin H93G Cavity Mutant, *J. Am. Chem. Soc.*, 1999, **121**, 12088-12093.
23. S. Yoshioka, S. Takahashi, K. Ishimori and I. Morishima, Roles of the axial push effect in cytochrome P450cam studied with the site-directed mutagenesis at the heme proximal site, *J. Inorg. Biochem.*, 2000, **81**, 141-151.
24. Z. Gross, The effect of axial ligands on the reactivity and stability of the oxoferryl moiety in model complexes of Compound I of heme-dependent enzymes, *J. Biol. Inorg. Chem.*, 1996, **1**, 368-371.
25. A. Takahashi, T. Kurahashi and H. Fujii, Effect of Imidazole and Phenolate Axial Ligands on the Electronic Structure and Reactivity of Oxoiron(IV) Porphyrin π-Cation Radical Complexes: Drastic Increase in Oxo-Transfer and Hydrogen Abstraction Reactivities, *Inorg. Chem.*, 2009, **48**, 2614-2625.
26. E. L. Onderko, A. Silakov, T. H. Yosca and M. T. Green, Characterization of a selenocysteine-ligated P450 compound I reveals direct link between electron donation and reactivity, *Nat. Chem.*, 2017, **9**, 623-628.
27. T. H. Yosca, R. K. Behan, C. M. Krest, E. L. Onderko, M. C. Langston and M. T. Green, Setting an Upper Limit on the Myoglobin Iron(IV)Hydroxide pKa: Insight into Axial Ligand Tuning in Heme Protein Catalysis, *J. Am. Chem. Soc.*, 2014, **136**, 9124-9131.
28. T. H. Yosca, A. P. Ledray, J. Ngo and M. T. Green, A new look at the role of thiolate ligation in cytochrome P450, *J. Biol. Inorg. Chem.*, 2017, **22**, 209-220.
29. W. Nam, M. H. Lim and S.-Y. Oh, Effect of Anionic Axial Ligands on the Formation of Oxoiron(IV) Porphyrin Intermediates, *Inorg. Chem.*, 2000, **39**, 5572-5575.
30. J. Thomas, T. Mokkawes, L. Senft, A. Dey, J. B. Gordon, I. Ivanovic-Burmazovic, S. P. de Visser and D. P. Goldberg, Axial Ligation Impedes Proton-Coupled Electron-Transfer Reactivity of a Synthetic Compound-I Analogue, *J. Am. Chem. Soc.*, 2024, **146**, 12338-12354.
31. N. Hessenauer-Ilicheva, A. Franke, M. Wolak, T. Higuchi and R. van Eldik, Spectroscopic and Mechanistic Studies on Oxidation Reactions Catalyzed by the Functional Model SR Complex for Cytochrome P450: Influence of Oxidant, Substrate, and Solvent, *Chem. Eur. J.*, 2009, **15**, 12447-12459.
32. Y. Kang, H. Chen, Y. J. Jeong, W. Lai, E. H. Bae, S. Shaik and W. Nam, Enhanced Reactivities of Iron(IV)-Oxo Porphyrin π-Cation Radicals in Oxygenation Reactions by Electron-Donating Axial Ligands, *Chem. Eur. J.*, 2009, **15**, 10039-10046.
33. M. A. Ehudin, L. B. Gee, S. Sabuncu, A. Braun, P. Moënne-Loccoz, B. Hedman, K. O. Hodgson, E. I. Solomon and K. D. Karlin, Tuning

the Geometric and Electronic Structure of Synthetic High-Valent Heme Iron(IV)-Oxo Models in the Presence of a Lewis Acid and Various Axial Ligands, *J. Am. Chem. Soc.*, 2019, **141**, 5942-5960.
34. M. Ortmayer, K. Fisher, J. Basran, E. M. Wolde-Michael, D. J. Heyes, C. Levy, S. L. Lovelock, J. L. R. Anderson, E. L. Raven, S. Hay, S. E. J. Rigby and A. P. Green, Rewiring the "Push-Pull" Catalytic Machinery of a Heme Enzyme Using an Expanded Genetic Code, *ACS Catalysis*, 2020, **10**, 2735-2746.
35. M. Selke and J. S. Valentine, Switching on the Nucleophilic Reactivity of a Ferric Porphyrin Peroxo Complex, *J. Am. Chem. Soc.*, 1998, **120**, 2652-2653.
36. W. Nam, M. H. Lim, S.-Y. Oh, J. H. Lee, H. J. Lee, S. K. Woo, C. Kim and W. Shin, Remarkable Anionic Axial Ligand Effects of Iron(III) Porphyrin Complexes on the Catalytic Oxygenations of Hydrocarbons by H_2O_2 and the Formation of Oxoiron(IV) Porphyrin Intermediates by m-Chloroperoxybenzoic Acid, *Angew. Chem.*, 2000, **112**, 3792-3795.
37. A. Franke, C. Fertinger and R. van Eldik, Axial Ligand and Spin-State Influence on the Formation and Reactivity of Hydroperoxo–Iron(III) Porphyrin Complexes, *Chem. Eur. J.*, 2012, **18**, 6935-6949.
38. S. Yokota, Y. Suzuki, S. Yanagisawa, T. Ogura, S. Nozawa, M. Hada and H. Fujii, How Do the Axial and Equatorial Ligands Modulate the Reactivity of a Metal-Bound Terminal Oxidant? An Answer from the Hypochlorite Adduct of Iron(III) Porphyrin, *ACS Catalysis*, 2022, **12**, 10857-10871..
39. P. K. Das, K. Mittra and A. Dey, Spectroscopic characterization of a phenolate bound Fe^{II}–O_2 adduct: gauging the relative "push" effect of a phenolate axial ligand, *Chem. Commun.*, 2014, **50**, 5218-5220.
40. S. Sivaramakrishnan, H. Ouellet, H. Matsumura, S. Guan, P. Moënne-Loccoz, A. L. Burlingame and P. R. Ortiz de Montellano, Proximal Ligand Electron Donation and Reactivity of the Cytochrome P450 Ferric–Peroxo Anion, *J. Am. Chem. Soc.*, 2012, **134**, 6673-6684.
41. R. L. Khade, Y. Yang, Y. Shi and Y. Zhang, HNO-Binding in Heme Proteins: Effects of Iron Oxidation State, Axial Ligand, and Protein Environment, *Angew. Chem. Int. Ed.*, 2016, **55**, 15058-15061.
42. D. Singh, H. Wasan and K. H. Reeta, Heme oxygenase-1 modulation: A potential therapeutic target for COVID-19 and associated complications, *Free Radical Biology and Medicine*, 2020, **161**, 263-271.
43. L. Hornyák, N. Dobos, G. Koncz, Z. Karányi, D. Páll, Z. Szabó, G. Halmos and L. Székvölgyi, The Role of Indoleamine-2,3-Dioxygenase in Cancer Development, Diagnostics, and Therapy, *Front. Immunol.*, 2018, **9**, 1-8.
44. J. A. Locke, L. Fazli, H. Adomat, J. Smyl, K. Weins, A. A. Lubik, D. B. Hales, C. C. Nelson, M. E. Gleave and E. S. Tomlinson Guns, A novel communication role for CYP17A1 in the progression of castration-resistant prostate cancer, *The Prostate*, 2009, **69**, 928-937.
45. S. Chumsri, T. Howes, T. Bao, G. Sabnis and A. Brodie, Aromatase, aromatase inhibitors, and breast cancer, *J. Steroid Biochem. Mol. Biol.*, 2011, **125**, 13-22.
46. T. Togo, O. Katsuse and E. Iseki, Nitric oxide pathways in Alzheimer's disease and other neurodegenerative dementias, *Neurol. Res.*, 2004, **26**, 563-566.
47. J. J. Woodward, M. M. Chang, N. I. Martin and M. A. Marletta, The Second Step of the Nitric Oxide Synthase Reaction: Evidence for Ferric-Peroxo as the Active Oxidant, *J. Am. Chem. Soc.*, 2009, **131**, 297-305.
48. S. L. Gantt, I. G. Denisov, Y. V. Grinkova and S. G. Sligar, The critical iron–oxygen intermediate in human aromatase, *Biochem. Biophys. Res. Commun.*, 2009, **387**, 169-173.
49. K. D. McCarty, Y. Tateishi, T. Y. Hargrove, G. I. Lepesheva and F. P. Guengerich, Oxygen-18 Labeling Reveals a Mixed Fe–O Mechanism in the Last Step of Cytochrome P450 51 Sterol 14α-Demethylation, *Angew. Chem. Int. Ed.*, 2024, **63**, e202317711.
50. P. J. Mak, M. C. Gregory, I. G. Denisov, S. G. Sligar and J. R. Kincaid, Unveiling the crucial intermediates in androgen production, *Proc. Nat. Acad. Sci.*, 2015, **112**, 15856-15861.
51. S.-i. J. Takayama, S. A. Loutet, A. G. Mauk and M. E. P. Murphy, A Ferric–Peroxo Intermediate in the Oxidation of Heme by IsdI, *Biochemistry*, 2015, **54**, 2613-2621.
52. H. Li, C. S. Raman, C. B. Glaser, E. Blasko, T. A. Young, J. F. Parkinson, M. Whitlow and T. L. Poulos, Crystal Structures of Zinc-free and -bound Heme Domain of Human Inducible Nitric-oxide Synthase: IMPLICATIONS FOR DIMER STABILITY AND COMPARISON WITH ENDOTHELIAL NITRIC-OXIDE SYNTHASE, *J. Biol. Chem.*, 1999, **274**, 21276-21284.
53. G. Fermi, M. F. Perutz, B. Shaanan and R. Fourme, The crystal structure of human deoxyhaemoglobin at 1.74 Å resolution, *J. Mol. Biol.*, 1984, **175**, 159-174.
54. M. Alfonso-Prieto, A. Borovik, X. Carpena, G. Murshudov, W. Melik-Adamyan, I. Fita, C. Rovira and P. C. Loewen, The Structures and Electronic Configuration of Compound I Intermediates of Helicobacter pylori and Penicillium vitale Catalases Determined by X-ray Crystallography and QM/MM Density Functional Theory Calculations, *J. Am. Chem. Soc.*, 2007, **129**, 4193-4205.
55. M. Gajhede, D. J. Schuller, A. Henriksen, A. T. Smith and T. L. Poulos, Crystal structure of horseradish peroxidase C at 2.15 Å resolution, *Nat. Struct. Mol. Biol.*, 1997, **4**, 1032-1038.
56. O.-M. Iova, G.-E. Marin, I. Lazar, I. Stanescu, G. Dogaru, C. A. Nicula and A. E. Bulboacă, Nitric Oxide/Nitric Oxide Synthase System in the Pathogenesis of Neurodegenerative Disorders—An Overview, *Antioxidants*, 2023, **12**, 753.
57. R. Kavya, R. Saluja, S. Singh and M. Dikshit, Nitric oxide synthase regulation and diversity: Implications in Parkinson's disease, *Nitric Oxide*, 2006, **15**, 280-294.
58. A. W. Deckel, Nitric oxide and nitric oxide synthase in Huntington's disease, *J. Neurosci. Res.*, 2001, **64**, 99-107.
59. M. K. Tripathi, M. Kartawy and H. Amal, The role of nitric oxide in brain disorders: Autism spectrum disorder and other psychiatric, neurological, and neurodegenerative disorders, *Redox Biology*, 2020, **34**, 101567.
60. D. A. Drechsel, A. G. Estévez, L. Barbeito and J. S. Beckman, Nitric Oxide-Mediated Oxidative Damage and the Progressive Demise of Motor Neurons in ALS, *Neurotox. Res.*, 2012, **22**, 251-264.
61. D. Basudhar, V. Somasundaram, G. A. de Oliveira, A. Kesarwala, J. L. Heinecke, R. Y. Cheng, S. A. Glynn, S. Ambs, D. A. Wink and L. A. Ridnour, Nitric Oxide Synthase-2-Derived Nitric Oxide Drives Multiple Pathways of Breast Cancer Progression, *Antiox. Redox Sign.*, 2016, **26**, 1044-1058.
62. S. Korde Choudhari, M. Chaudhary, S. Bagde, A. R. Gadbail and V. Joshi, Nitric oxide and cancer: a review, *World J. Surg. Oncol.*, 2013, **11**, 118.
63. Y. Soni, K. Softness, H. Arora and R. Ramasamy, The Yin Yang Role of Nitric Oxide in Prostate Cancer, *American Journal of Men's Health*, 2020, **14**, 1557988320903191.
64. K. Zafirellis, A. Zachaki, G. Agrogiannis and K. Gravani, Inducible nitric oxide synthase expression and its prognostic significance in colorectal cancer, *APMIS*, 2010, **118**, 115-124.

65. W.-C. Hung, T.-F. Wu, S.-C. Ng, Y. C. Lee, H.-P. Shen, S.-F. Yang and P.-H. Wang, Involvement of endothelial nitric oxide synthase gene variants in the aggressiveness of uterine cervical cancer, *J. Cancer*, 2019, **10**, 2594-2600.
66. G. G. Chen, T. W. Lee, H. Xu, J. H. Y. Yip, M. Li, T. S. K. Mok and A. P. C. Yim, Increased inducible nitric oxide synthase in lung carcinoma of smokers, *Cancer*, 2008, **112**, 372-381.
67. A. Bakshi, T. C. Nag, S. Wadhwa, A. K. Mahapatra and C. Sarkar, The expression of nitric oxide synthases in human brain tumours and peritumoral areas, *J. Neurol. Sci.*, 1998, **155**, 196-203.
68. C. S. Cobbs, J. E. Brenman, K. D. Aldape, D. S. Bredt and M. A. Israel, Expression of Nitric Oxide Synthase in Human Central Nervous System Tumors1, *Cancer Res.*, 1995, **55**, 727-730.
69. F. Cianchi, C. Cortesini, O. Fantappiè, L. Messerini, N. Schiavone, A. Vannacci, S. Nistri, I. Sardi, G. Baroni, C. Marzocca, F. Perna, R. Mazzanti, P. Bechi and E. Masini, Inducible Nitric Oxide Synthase Expression in Human Colorectal Cancer: Correlation with Tumor Angiogenesis, *Am. J. Patho.*, 2003, **162**, 793-801.
70. R. S. Nomelini, L. C. d. A. Ribeiro, B. M. Tavares-Murta, S. J. Adad and E. F. C. Murta, Production of Nitric Oxide and Expression of Inducible Nitric Oxide Synthase in Ovarian Cystic Tumors, *Mediators Inflamm.*, 2008, **2008**, 186584.
71. U. Förstermann and W. C. Sessa, Nitric oxide synthases: regulation and function, *Eur. Heart J.*, 2012, **33**, 829-837.
72. B. Salimian Rizi, A. Achreja and D. Nagrath, Nitric Oxide: The Forgotten Child of Tumor Metabolism, *Trends in Cancer*, 2017, **3**, 659-672.
73. S. Daff, NO synthase: structures and mechanisms, *Nitric Oxide*, 2010, **23**, 1-11.
74. N. Lehnert, E. Kim, H. T. Dong, J. B. Harland, A. P. Hunt, E. C. Manickas, K. M. Oakley, J. Pham, G. C. Reed and V. S. Alfaro, The Biologically Relevant Coordination Chemistry of Iron and Nitric Oxide: Electronic Structure and Reactivity, *Chem. Rev.*, 2021, **121**, 14682-14905.
75. A. Aicardo, D. M. Martinez, N. Campolo, S. Bartesaghi and R. Radi, in *Biochemistry of Oxidative Stress: Physiopathology and Clinical Aspects*, eds. R. J. Gelpi, A. Boveris and J. J. Poderoso, Springer International Publishing, Cham, 2016, vol. 16, pp. 49-77.
76. M. A. Cinelli, H. T. Do, G. P. Miley and R. B. Silverman, Inducible nitric oxide synthase: Regulation, structure, and inhibition, *Med. Res. Rev.*, 2020, **40**, 158-189.
77. S. Tong, M. A. Cinelli, N. S. El-Sayed, H. Huang, A. Patel, R. B. Silverman and S. Yang, Inhibition of interferon-gamma-stimulated melanoma progression by targeting neuronal nitric oxide synthase (nNOS), *Sci. Rep.*, 2022, **12**, 1701.
78. A. D. Vaz, S. J. Pernecky, G. M. Raner and M. J. Coon, Peroxo-iron and oxenoid-iron species as alternative oxygenating agents in cytochrome P450-catalyzed reactions: switching by threonine-302 to alanine mutagenesis of cytochrome P450 2B4, *Proc. Nat. Acad. Sci.*, 1996, **93**, 4644-4648.
79. R. Minhas, Y. Bansal and G. Bansal, Inducible nitric oxide synthase inhibitors: A comprehensive update, *Med. Res. Rev.*, 2020, **40**, 823-855.
80. J. T. Groves and C. C. Y. Wang, Nitric oxide synthase: models and mechanisms, *Curr. Opin. Chem. Biol.*, 2000, **4**, 687-695.
81. H. Huang, J.-M. Hah and R. B. Silverman, Mechanism of Nitric Oxide Synthase. Evidence that Direct Hydrogen Atom Abstraction from the O−H Bond of NG-Hydroxyarginine Is Not Relevant to the Mechanism, *J. Am. Chem. Soc.*, 2001, **123**, 2674-2676.
82. Y. Zhu and R. B. Silverman, Revisiting Heme Mechanisms. A Perspective on the Mechanisms of Nitric Oxide Synthase (NOS), Heme Oxygenase (HO), and Cytochrome P450s (CYP450s), *Biochemistry*, 2008, **47**, 2231-2243.
83. T. Doukov, H. Li, M. Soltis and T. L. Poulos, Single Crystal Structural and Absorption Spectral Characterizations of Nitric Oxide Synthase Complexed with Nω-Hydroxy-l-arginine and Diatomic Ligands, *Biochemistry*, 2009, **48**, 10246-10254.
84. R. Davydov, J. Sudhamsu, N. S. Lees, B. R. Crane and B. M. Hoffman, EPR and ENDOR Characterization of the Reactive Intermediates in the Generation of NO by Cryoreduced Oxy-Nitric Oxide Synthase from *Geobacillus stearothermophilus*, *J. Am. Chem. Soc.*, 2009, **131**, 14493-14507.
85. J. Santolini, The molecular mechanism of mammalian NO-synthases: A story of electrons and protons, *J. Inorg. Biochem.*, 2011, **105**, 127-141.
86. R. Davydov, K. J. Labby, S. E. Chobot, D. A. Lukoyanov, B. R. Crane, R. B. Silverman and B. M. Hoffman, Enzymatic and Cryoreduction EPR Studies of the Hydroxylation of Methylated Nω-Hydroxy-l-arginine Analogues by Nitric Oxide Synthase from *Geobacillus stearothermophilus*, *Biochemistry*, 2014, **53**, 6511-6519.
87. K. Jansen Labby, H. Li, L. J. Roman, P. Martásek, T. L. Poulos and R. B. Silverman, Methylated Nω-Hydroxy-l-arginine Analogues as Mechanistic Probes for the Second Step of the Nitric Oxide Synthase-Catalyzed Reaction, *Biochemistry*, 2013, **52**, 3062-3073.
88. S. Bhattacharya, T. R. Lakshman, S. Sutradhar, C. K. Tiwari and T. K. Paine, Bioinspired oxidation of oximes to nitric oxide with dioxygen by a nonheme iron(II) complex, *J. Biol. Inorg. Chem.*, 2020, **25**, 3-11.
89. C. C. Y. Wang, D. M. Ho and J. T. Groves, Models of Nitric Oxide Synthase: Iron(III) Porphyrin-Catalyzed Oxidation of Fluorenone Oxime to Nitric Oxide and Fluorenone, *J. Am. Chem. Soc.*, 1999, **121**, 12094-12103.
90. A. Maldotti, A. Molinari, I. Vitali, E. Ganzaroli, P. Battioni, D. Mathieu and D. Mansuy, Oxidation of N-(4-Chlorophenyl)-N'-hydroxyguanidine to N-(4-Chlorophenyl)urea and Nitric Oxide by Photoexcited Iron Porphyrins, *Eur. J. Inorg. Chem.*, 2004, **2004**, 3127-3135.
91. N. Jain, A. Kumar and S. M. S. Chauhan, Metalloporphyrin and heteropoly acid catalyzed oxidation of C=NOH bonds in an ionic liquid: biomimetic models of nitric oxide synthase, *Tetrahedron Lett.*, 2005, **46**, 2599-2602.
92. P. Mondal, I. Ishigami, S.-R. Yeh and G. B. Wijeratne, The Role of Heme Peroxo Oxidants in the Rational Mechanistic Modeling of Nitric Oxide Synthase: Characterization of Key Intermediates and Elucidation of the Mechanism, *Angew. Chem. Int. Ed.*, 2022, **61**, e202211521.
93. K. D. Karlin, Model offers intermediate insight, *Nature*, 2010, **463**, 168.
94. The addition of axial ligands did not result in significant alterations in self-decay rates of heme-PO adducts (Figure S1).
95. J.-G. Liu, T. Ohta, S. Yamaguchi, T. Ogura, S. Sakamoto, Y. Maeda and Y. Naruta, Spectroscopic Characterization of a Hydroperoxo–Heme Intermediate: Conversion of a Side-On Peroxo to an End-On Hydroperoxo Complex, *Angew. Chem. Int. Ed.*, 2009, **48**, 9262-9267.
96. I. Garcia-Bosch, S. M. Adam, A. W. Schaefer, S. K. Sharma, R. L. Peterson, E. I. Solomon and K. D. Karlin, A "Naked" Fe^{III}-(O_2^{2-})-Cu^{II} Species Allows for Structural and Spectroscopic Tuning of

Low-Spin Heme-Peroxo-Cu Complexes, *J. Am. Chem. Soc.*, 2015, **137**, 1032-1035.
97. H. Kim, P. J. Rogler, S. K. Sharma, A. W. Schaefer, E. I. Solomon and K. D. Karlin, Ferric Heme Superoxide Reductive Transformations to Ferric Heme (Hydro)Peroxide Species: Spectroscopic Characterization and Thermodynamic Implications for H-Atom Transfer (HAT), *Angew. Chem. Int. Ed.*, 2021, **60**, 5907-5912.
98. J.-G. Liu, Y. Shimizu, T. Ohta and Y. Naruta, Formation of an End-On Ferric Peroxo Intermediate upon One-Electron Reduction of a Ferric Superoxo Heme, *J. Am. Chem. Soc.*, 2010, **132**, 3672-3673.
99. S. Panda, H. Phan and K. D. Karlin, Heme-copper and Heme O_2-derived synthetic (bioinorganic) chemistry toward an understanding of cytochrome c oxidase dioxygen chemistry, *J. Inorg. Biochem.*, 2023, **249**, 112367.
100. E. M. Arnett and C. Y. Wu, Base Strengths of Some Saturated Cyclic Ethers in Aqueous Sulfuric Acid, *J. Am. Chem. Soc.*, 1962, **84**, 1684-1688.
101. J. D. Vaughan, V. L. Vaughan, S. S. Daly and W. A. Smith, Jr., Kinetics of iodination of 4-methylimidazole and 2-methylimidazole, *J. Org. Chem.*, 1980, **45**, 3108-3111.
102. Calculated using Advanced Chemistry Development (ACD/Labs) Software (© 1994-2024 ACD/Labs)
103. J. J. Christensen, L. D. Hansen and R. M. Izatt, *Handbook of proton ionization heats and related thermodynamic quantities*, Wiley, 1976.
104. P. Bolton, F. Hall and J. Kudrynski, Thermodynamic functions of ionization of t-butyl-substituted and methoxysubstituted phenols, *Aust. J. Chem.*, 1972, **25**, 75-80.
105. F. G. Bordwell and D. L. Hughes, Thiol acidities and thiolate ion reactivities toward butyl chloride in dimethyl sulfoxide solution. The question of curvature in Broensted plots, *J. Org. Chem.*, 1982, **47**, 3224-3232.
106. K. Nakamoto and H. Oshio, Effect of thiolate vs. nitrogen-base ligands on oxygen stretching frequencies of (oxytetraphenylporphyrinato)cobalt, *J. Am. Chem. Soc.*, 1985, **107**, 6518-6521.
107. P. Anzenbacher, J. H. Dawson and T. Kitagawa, Towards a unified concept of oxygen activation by heme enzymes: the role of the proximal ligand, *J. Mol. Struct.*, 1989, **214**, 149-158.
108. H. M. Neu, M. G. Quesne, T. Yang, K. A. Prokop-Prigge, K. M. Lancaster, J. Donohoe, S. DeBeer, S. P. de Visser and D. P. Goldberg, Dramatic Influence of an Anionic Donor on the Oxygen-Atom Transfer Reactivity of a MnV–Oxo Complex, *Chem. Eur. J.*, 2014, **20**, 14584-14588.
109. G. Palmer, in *The Porphyrins*, Academic Press, 1979, pp. 313-353.
110. J. Peisach, W. E. Blumberg, S. Ogawa, E. A. Rachmilewitz and R. Oltzik, The Effects of Protein Conformation on the Heme Symmetry in High Spin Ferric Heme Proteins as Studied by Electron Paramagnetic Resonance, *J. Biol. Chem.*, 1971, **246**, 3342-3355.
111. J. Peisach, W. E. Blumberg, B. A. Wittenberg, J. B. Wittenberg and L. Kampa, HEMOGLOBIN A: AN ELECTRON PARAMAGNETIC RESONANCE STUDY OF THE EFFECTS OF INTERCHAIN CONTACTS ON THE HEME SYMMETRY OF HIGH-SPIN AND LOW-SPIN DERIVATIVES OF FERRIC ALPHA CHAINS, *Proc. Natl. Acad. Sci. U. S. A.*, 1969, **63**, 934-939.
112. H. C. Lee, J. Peisach, Y. Dou and M. Ikeda-Saito, Electron-Nuclear Coupling to the Proximal Histidine in Oxycobalt-Substituted Distal Histidine Mutants of Human Myoglobin, *Biochemistry*, 1994, **33**, 7609-7618.
113. G. Roelfes, V. Vrajmasu, K. Chen, R. Y. N. Ho, J.-U. Rohde, C. Zondervan, R. M. la Crois, E. P. Schudde, M. Lutz, A. L. Spek, R. Hage, B. L. Feringa, E. Münck and L. J. Que, End-On and Side-On Peroxo Derivatives of Non-Heme Iron Complexes with Pentadentate Ligands: Models for Putative Intermediates in Biological Iron/Dioxygen Chemistry, *Inorg. Chem.*, 2003, **42**, 2639-2653.
114. N. J. York, M. M. Lockart and B. S. Pierce, Low-Spin Cyanide Complexes of 3-Mercaptopropionic Acid Dioxygenase (MDO) Reveal the Impact of Outer-Sphere SHY-Motif Residues, *Inorg. Chem.*, 2021, **60**, 18639-18651.
115. J. S. Griffith, Theory of E.P.R. in low-spin ferric haemoproteins, *Mol Phys.*, 1971, **21**, 135-139.
116. C. P. S. Taylor, The EPR of Low Spin Heme Complexes: relation of the t_2g hole model to the directional properties of the g-tensor and a new method for calculating the ligand field parameters, *Biochim Biophys Acta.*, 1977, **491**, 137-149.
117. K. Duerr, J. Olah, R. Davydov, M. Kleimann, J. Li, N. Lang, R. Puchta, E. Hubner, T. Drewello, J. N. Harvey, N. Jux and I. Ivanovic-Burmazovic, Studies on an iron(iii)-peroxo porphyrin. Iron(iii)-peroxo or iron(ii)-superoxo?, *Dalton Trans.*, 2010, **39**, 2049-2056.
118. The change in O–O_{peroxo} bond length is negligible.

View Article Online
DOI: 10.1039/D4SC08701A

Data availability

The data supporting this article have been included as part of the Supplementary Information.

Supporting Information for

Modulation of Heme Peroxo Nucleophilicities with Axial Ligands Reveal Key Insights into the Mechanistic Landscape of Nitric Oxide Synthase

Shanuk Rajapakse,[a] Yuri Lee,[b] Samith B. Jayawardana,[a] Joshua Helms,[a] Pritam Mondal,[a] Akhil Singh,[a] Brad S. Pierce,[a,*] Hannah S. Shafaat,[b,*] and Gayan B. Wijeratne[a,*]

[a] Department of Chemistry and Biochemistry, University of Alabama, Tuscaloosa, AL 35401, United States. E-mail: gwijeratne@ua.edu

[b] Department of Chemistry and Biochemistry, University of California, Los Angeles, Los Angeles, CA 90095, United States. Email: shafaat@ucla.edu

*To whom correspondence should be addressed:
Gayan B. Wijeratne
gwijeratne@ua.edu

Experimental Section

1. Materials and Methods

All commercially available chemicals were purchased at the highest available purity and used as received unless otherwise stated. Air-sensitive compounds were handled either under an argon atmosphere using standard Schlenk techniques, or in an MBraun Unilab Pro SP (<0.1 ppm O_2, <0.1 ppm H_2O) nitrogen-filled glovebox. All organic solvents were purchased at HPLC-grade or better and degassed (bubbling argon gas for 40 min at room temperature) and dried (passing through a 60 cm alumina column) using an Inert Pure Solv MD 5 (2018) solvent purification system. These solvents were then stored in dark glass bottles inside the glovebox over 4 Å molecular sieves at least for 72 hrs prior to use. Benchtop UV-vis experiments were carried out using Agilent Cary 60 spectrophotometer equipped with a liquid nitrogen chilled Unisoku CoolSpek UV USP-203-B cryostat. A 2 mm path length quartz cell cuvette modified with an extended glass neck with a female 14/19 joint and stopcock was used to perform all UV–vis experiments. Low-temperature ^2H NMR spectroscopic studies were carried out on a Bruker AV 360 MHz NMR Spectrometer. ^1H NMR spectra were recorded on a Bruker 500 MHz NMR spectrometer. All spectra were recorded in 5-mm (outer diameter) NMR tubes. The chemical shifts were reported as δ (ppm) values calibrated to natural abundance deuterium or proton solvent peaks. For LC-MS analysis, Spectra were obtained in Waters Xevo G2-XS QTOF instrument and Bruker Rapiflex instrument. GC-FID analyses were performed on a Agilent Technologies 8860 GC, using an Agilent DB-1701 (30 m, 0.32 mm, 1.0 μm) column. GC-MS was carried out using an Agilent Technologies 6890N GC, using an Agilent DB-5ms (30 m, 0.25 mm, 0.25 μm) column. The yield determinations were conducted with the GC-FID using calibration curves with n-dodecane as an internal standard. CW EPR experiments were performed at the UA EPR facility using a Bruker ELEXSYS E540 X-band spectrometer (Bruker-Biospin Billerica, MA). Cryogenic measurements were made using a ColdEdge Stinger closed-loop liquid helium cryosystem inserted into an Oxford ESR900 cryostat. A LakeShore 336 temperature controller was used to regulate sample temperature. EPR simulations were calculated using SpinCount developed by Professor Michael Hendrich at Carnegie Mellon University by utilizing the general spin Hamiltonian as shown in Equation **A**.[1-3]

Eq. A $$\hat{H} = \boldsymbol{D}\left(\hat{S}_Z^2 - \frac{\hat{S}^2}{3}\right) + \boldsymbol{E}\left(\hat{S}_X^2 - \hat{S}_Y^2\right) + \beta_e \boldsymbol{S_c} \cdot \boldsymbol{g} \cdot \mathbf{B}$$

In this expression, $\boldsymbol{g}$ is the *g*-tensor for the coupled spin-system ($\boldsymbol{S_c}$), and the axial and rhombic zero-field splitting (*zfs*) parameters are represented by $\boldsymbol{D}$ and $\boldsymbol{E}$, respectively. This program computes the powder pattern for a uniform spherical distribution of the magnetic field vector $\boldsymbol{B}$, and the transition intensities are calculated using '*Fermi's golden rule*'.[4] All simulations were generated with consideration of all intensity factors, both theoretical and experimental, to allow for determination of species concentration. The only unknown factor relating the spin concentration to signal intensity was an instrumental factor that is specific to the microwave detection system. However, this was determined by the spin standard, 1 mM Cu(EDTA), prepared from a copper atomic absorption standard solution purchased from Sigma-Aldrich. Resonance Raman spectra were collected using a setup described previously.[5] All resonance Raman spectra were collected at 77 K on samples held within a liquid nitrogen finger dewar. Raman spectra were collected using 457 nm excitation from a Cobolt Twist diode laser. The excitation beam was focused onto the sample using a 100 mm focal length UV plano-convex lens (Thorlabs), and the scattered light was collected using a UV-fused aspheric lens (Edmund Physics). Elastic scattering of the Rayleigh line was rejected using the corresponding long-pass edge filter (Semrock RazorEdge). The Raman scattered light was imaged onto a spectrograph (Princeton Instruments Isoplane) furnished with an 1800 gr/mm 500-nm blazed grating and measured with a Peltier-cooled CCD detector (Princeton Instruments Pixis 100B). 5,10,15,20 tetraphenylporphyrin iron(III) chloride, [(TPP)Fe^{III}Cl], 4-Methylimidazole (4-MeIm), 4-Dimethylaminopyridine (DMAP), 1,5-Dicyclohexylimidazole (DCHIm), Sodium thiophenolate (ArS-) was purchased from commercial sources. The syntheses of $H_2(F_{20}TPP)$,[6] H_2(TPP-d_8),[7] $H_2(F_{20}TPP\text{-}d_8)$,[8] naked [(TPP)$Fe^{III}$]$SbF_6$,[9] Sodium 3,5-dimethoxyphenolate (ArO^-),[10] Tetrabutylammonium thiophenolate,[11] were carried out according to previously published methods. Metalation of the porphyrinates to generate [(F_{20}TPP)Fe^{III}Cl], and [(TPP-d_8)Fe^{III}Cl], and the subsequent reduction to [$(THF)_2$(Por)Fe^{II}] complexes were carried out by following previously reported procedures.[12] Formation of the heme peroxo [(B)(Por)$Fe^{III}(O_2^{2-})]^-$ complexes, where Por = the porphyrinate supporting ligand: (where Por = TPP, F_{20}TPP) and B = axial ligands, was carried out following a previously reported procedure.[13, 14]

2. Formation of axial ligated heme peroxo, $[(B)(Por)Fe^{III}(O_2^{2-})]^-$ complexes, where Por = porphyrinate supporting ligand, and B = axial ligands: Generation of the heme peroxo complexes, $[(Por)Fe^{III}(O_2^{2-})]^-$, was carried out following a literature-adapted procedure.[13, 14] In a typical experiment, a 50 μM THF solution (1 mL) of $[(THF)_2(Por)Fe^{II}]$ was added into a 2 mm pathlength Schlenk cuvette inside the glovebox and was sealed using a rubber septum. Upon cooling down inside the UV-vis cryostat stabilized at –40 ºC, this solution was bubbled with dry dioxygen gas using a needle, and excess O_2(g) was removed by three vacuum/Ar purge cycles. The complete formation of the superoxide complexes, $[(Por)Fe^{III}(O_2^{-\bullet})]$, was monitored by UV–vis spectroscopy (Figure 2A). Subsequently, 1 equiv of cobaltocene (in 50 μL of DCM) was added to generate the peroxo complex $[(Por)Fe^{III}(O_2^{2-})]^-$. To which 2 equiv of axial ligand (in 50 μL of DCM) was added to form the axial ligated heme peroxo complex, $[(B)(Por)Fe^{III}(O_2^{2-})]^-$ (Scheme 1.) (Figure 2A). Due to solubility issues, 2 equiv of 15-crown-5 was added to sodium 3,5-dimethoxyphenolate and sodium thiophenolate.

3. Resonance Raman and EPR sample preparation: In a typical resonance Raman sample preparation, 100 μL of the ferrous heme complex, $[(THF)_2(TPP)Fe^{II}]$ (4 mM in 9:1 DCM:THF), was placed in a 250 mm EPR tube (4 mm O.D.) and was sealed with a rubber septum inside the glovebox. Following cooling to −40 °C (using liquid nitrogen/acetone cold bath), dry O_2(g) (or $^{18}O_2$(g)) was bubbled through the solution using a three-way gastight syringe to generate the corresponding superoxo complex, $[(TPP)Fe^{III}(O_2^{-\bullet})]$. Subsequently, 1 equiv of cobaltocene (50 μL) was added in, and the reaction mixture was quickly homogenized with dry Ar bubbling to generate the corresponding $[(TPP)Fe^{III}(O_2^{2-})]^-$ complexes. To which 2 equiv of 4-MeIm (50 μL) (or other axial ligands) was added to form the axial ligated heme peroxo complex, $[(4\text{-MeIm})(TPP)Fe^{III}(O_2^{2-})]^-$. Immediately following the generation of the complexes, the final mixtures were frozen in liquid N_2. EPR sample preparation was also carried out using the same methodology. Tetrabutylammonium thiophenolate/phenolate was used to overcome solubility issues in EPR/rR sample preparation.

4. Low-temperature ^{2}H NMR spectroscopic studies: For a typical ^{2}H NMR experiment, $[(THF)_2(TPP\text{-}d_8)Fe^{II}]$ (15 mg, 0.023 mmol) was dissolved in 0.4 mL of 9:1 DCM:THF, and was

sealed in a 5 mm (outer diameter) NMR tube within the glovebox. This tube was then stabilized at –40 °C using a liquid nitrogen/acetone cold bath, followed by the addition of O_2(g) by means of a 9" needle to generate the [(TPP-d_8)$Fe^{III}(O_2^{-\bullet})$] complex. Subsequently, 1 equiv of cobaltocene (50 μL) was added using a Hamilton gas-tight syringe, and was quickly mixed with Ar bubbling to form the corresponding [(TPP-d_8)$Fe^{III}(O_2^{2-})]^-$ complex. To which 2 equiv of 4-MeIm (50 μL) (or other axial ligands) was added to form the axial ligated heme peroxo complex, [(4-MeIm)(TPP-d_8)$Fe^{III}(O_2^{2-})]^-$. The tube was then immediately transferred into the cryostat of the NMR spectrometer held at –40 °C.

5. Spectroscopic reactivity and kinetic studies of [(B)(Por)$Fe^{III}(O_2^{2-})]^-$ with oxime substrates: For each kinetic experiment, 50 μM 9:1 DCM:THF solution of [(B)(Por)$Fe^{III}(O_2^{2-})]^-$ complex (1 mL) was generated in a 2 mm pathlength Schlenk cuvette as previously described (*vide supra*). Subsequently, 200-500 equiv of acetophenone oxime substrates (50 μL in DCM) was added into the cuvette using a gas-tight syringe, and the reaction mixture was quickly mixed with dry argon bubbling. The reaction was monitored by the progression of Soret band spectral changes centered at 436 nm (for [(B)(TPP)$Fe^{III}(O_2^{2-})]^-$) or 432 nm ([(B)(F_{20}TPP)$Fe^{III}(O_2^{2-})]^-$) until plateaued. Kinetic studies were carried out, under pseudo-first-order conditions, by the addition of 200–500 equiv of acetophenone oxime to a 50 μM 1 mL 9:1 DCM:THF solution of [(B)(TPP)$Fe^{III}(O_2^{2-})]^-$ at –40 °C and 500 equiv of acetophenone Oxime was used for [(F_{20}TPP)$Fe^{III}(O_2^{2-})]^-$. Kinetic experiments at variable temperatures (at –30, –40, –50, -60 °C) were performed using [(TPP)$Fe^{III}(O_2^{2-})]^-$ and variable temperatures (at –40, –50, –60, -70 °C) for [(ArO^-)(TPP)$Fe^{III}(O_2^{2-})]^{2-}$ for acetophenone oxime substrate (200–500 equiv) following the same procedure as described, allowing the cuvette to achieve thermal equilibrium (10 min) in the cryostat, prior to the addition of the substrate. The pseudo first-order rate constants, k_{obs} were calculated from plots of ln[($A-A_f$)/(A_i-A_f)] vs time(s), where A_i and A_f are initial and final absorbances, respectively. The second-order rate constants (k_2) were obtained from the slope of the best-fit line from a plot of k_{obs} values vs substrate concentration.

6. Bulk oxidation reactions and characterization of organic products: The bulk oxidation reaction of acetophenone oxime substrates using [(4-MeIm)(TPP)$Fe^{III}(O_2^{2-})]^-$ was carried out by a generalized procedure as follows: A 100 mL Schlenk flask, equipped with a magnetic stir bar,

containing [$(THF)_2(TPP)Fe^{II}$] (200 mg, 0.3 mmol) in 9:1 DCM:THF (25 mL) was cooled in a liquid N_2/ acetone bath adjusted to −40 °C. Upon temperature equilibration, dioxygen gas ($O_2(g)$) was bubbled through to form [$(THF)(TPP)Fe^{III}(O_2^{-\bullet})$]. Subsequently, 1 equiv of cobaltocene (in 1 mL DCM) was added to form [$(THF)(TPP)Fe^{III}(O_2^{2-})]^-$. To which 2 equiv of 4-MeIm (1 mL) was added to form the axial ligated heme peroxo complex, [$(4\text{-}MeIm)(TPP)Fe^{III}(O_2^{2-})]^-$. Then acetophenone oxime (2 g, 15 mmol; in 5 mL of DCM) was added to it, and the reaction mixture was stirred for another 2 hr at –40 °C before it was dried in vacuum. The final (organic) product, acetophenone, was purified by silica gel column chromatography using DCM:hexane (1:1) as an eluent. GC-FID analysis for yield quantification of acetophenone was conducted using 1.5 mM solutions of [$(B)(TPP)Fe^{III}(O_2^{2-})]^-$ (B= 4-DMAP, ArO^-) complexes. The nitroxyl (NO^-) identification experiment was carried out following the above procedure using [$(4\text{-}MeIm)(TPP)Fe^{III}(O_2^{2-})]^-$ and acetophenone oxime as a substrate in the presence of 50 equiv PPh_3. The final reaction mixture was dried in a vacuum, and the phosphorus-containing products were characterized using LC-MS spectroscopy. Yield quantification of triphenylphosphine oxide (TPPO) was performed with a 0.5 mM concentration of [$(4\text{-}MeIm)(TPP)Fe^{III}(O_2^{2-})]^-$, which was further diluted for LC-MS analysis.

Acetophenone yield: 14 mg (34%); ^{1}H NMR (400 MHz, $CDCl_3$) δ 7.98-7.96 (m, 2H), 7.59-7.55 (m, 1H), 7.49-7.45 (m, 2H), 2.61 (s, 3H); GC-MS: m/z = 120.04 (calc. 120.0).

7. Computational Studies:

All calculations were performed with the package of Gaussian 16, revision C.01.7.[15] Geometry optimizations were carried out using uB97D within the spin-unrestricted formalism.[16, 17] The basis set was def2-TZVP for all atoms.[18] Counter ions (in phenolate and thiophenolate) were removed and not included in the calculations. Vibrational frequencies were obtained for all optimized geometries to ensure the latter did not lead to any imaginary frequencies. Complexes [$(THF)(TPP)Fe^{III}(O_2^{2-})$], [$(4\text{-}MeIm)(TPP)Fe^{III}(O_2^{2-})$] were optimized as charge -1 and sextet, quartet and doublet spin multiplicities while [$(ArO^-)(TPP)Fe^{III}(O_2^{2-})$] and [$(ArS^-)(TPP)Fe^{III}(O_2^{2-})$] were optimized as -2 charge and all possible spin multiplicities. A solvent correction (self-consistent reaction field) using the continuum polarized conductor model with a dielectric constant mimicking dichloromethane and zero-point energies has been included in the energy comparison

of different spin states.[19] Bonding and orbital analysis were done by using Chemcraft software.[20] The natural charges of the atoms were calculated using natural bond orbital (NBO) analysis.[21]

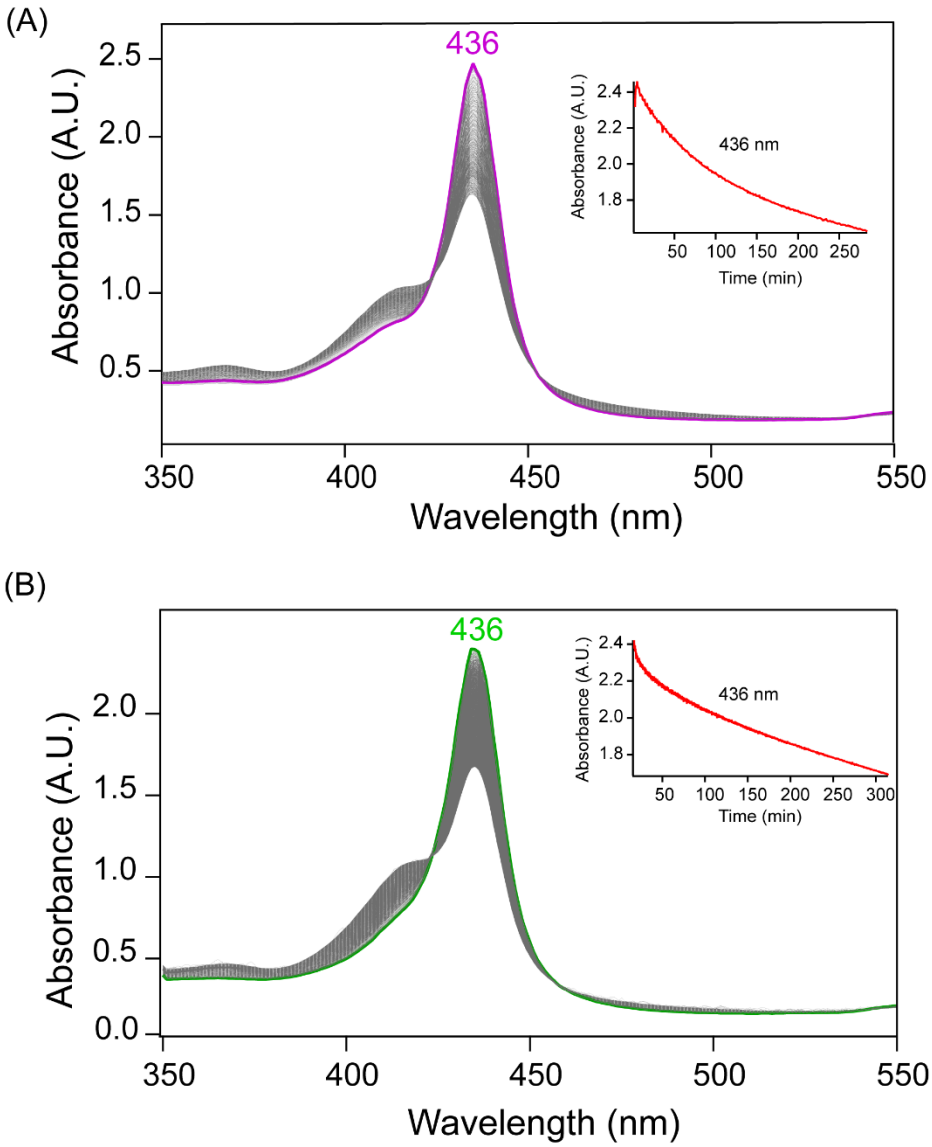

Figure S1. Electronic absorption spectral changes (in 9:1 DCM:THF at –40 ºC) of the self-decay of (A) parent heme-PO complex $[(THF)(TPP)Fe^{III}(O_2^{2-})]^-$ (Purple) and (B) thiophenolate ligated $[(ArS^-)(TPP)Fe^{III}(O_2^{2-})]^{2-}$ (Green). Insets show the kinetic time traces at 436 nm.

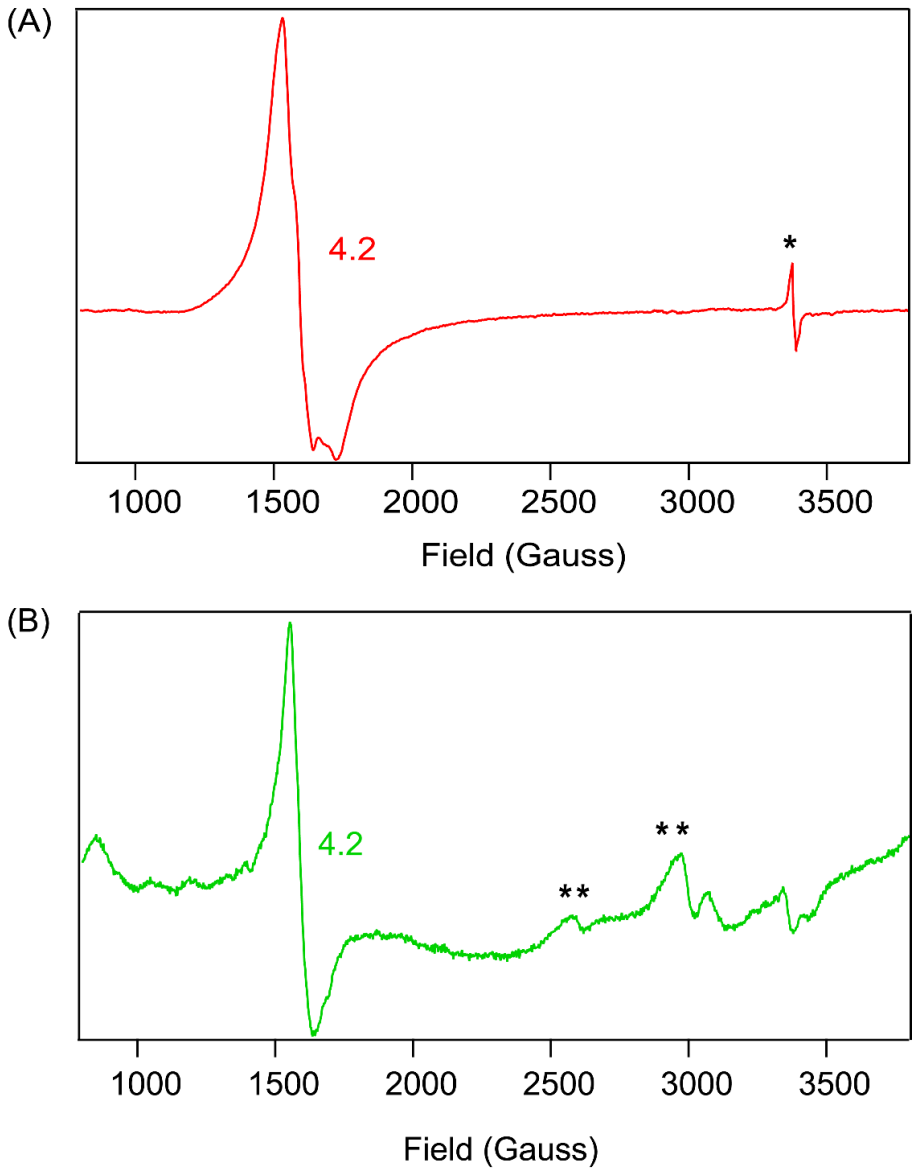

Figure S2. EPR spectral features (in frozen 9:1 DCM:THF at 7 K) for 2 mM solutions of (A) $[(THF)(TPP)Fe^{III}(O_2^{2-})]^-$, *feature (g = 1.99) corresponds to an excess of cobaltocene, and (B) $[(4\text{-}MeIm)(TPP)Fe^{III}(O_2^{2-})]^-$ (g = 4.2); **features (g = 2.6, 2.1) corresponds to the ferric bis-imidazole complex.

(A)

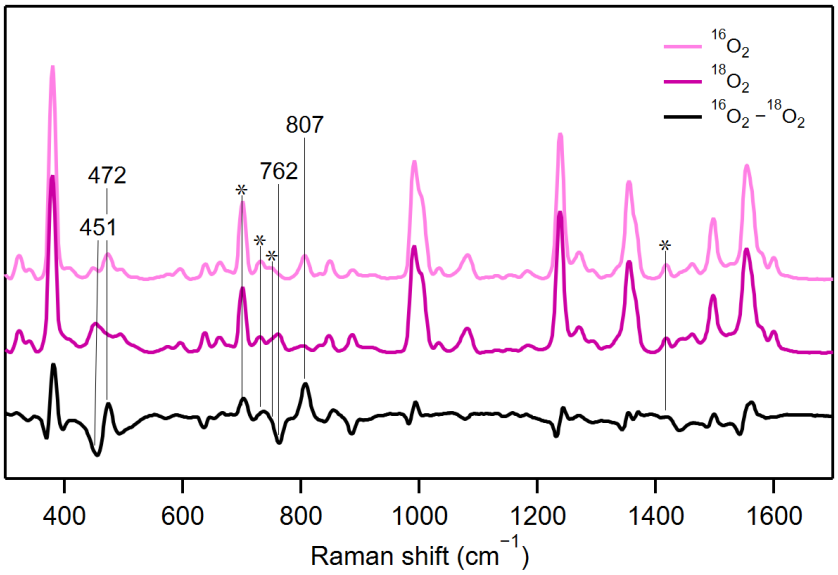
$^{16}O_2$
$^{18}O_2$
$^{16}O_2 - ^{18}O_2$
807
762
472
451
*
*
*
*
400
600
800
1000
1200
1400
1600
Raman shift (cm^{-1})

(B)

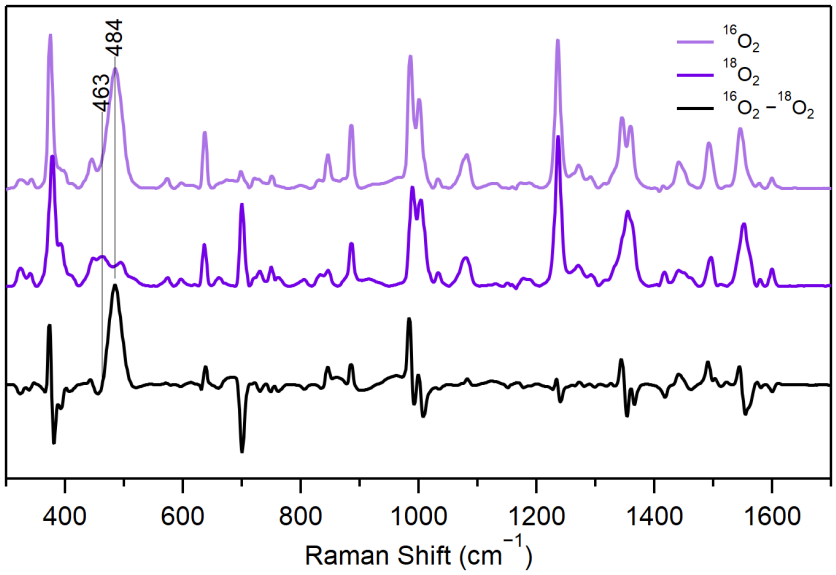
$^{16}O_2$
$^{18}O_2$
$^{16}O_2 - ^{18}O_2$
484
463
400
600
800
1000
1200
1400
1600
Raman Shift (cm^{-1})

(C)

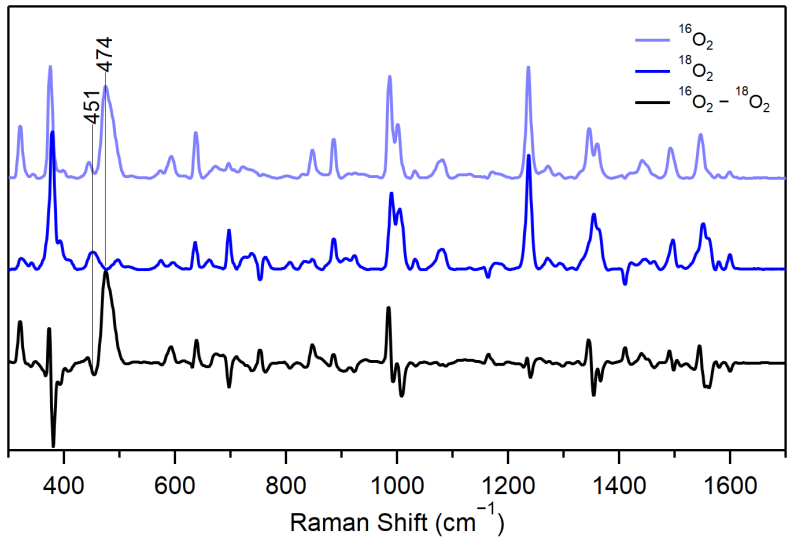

(D)

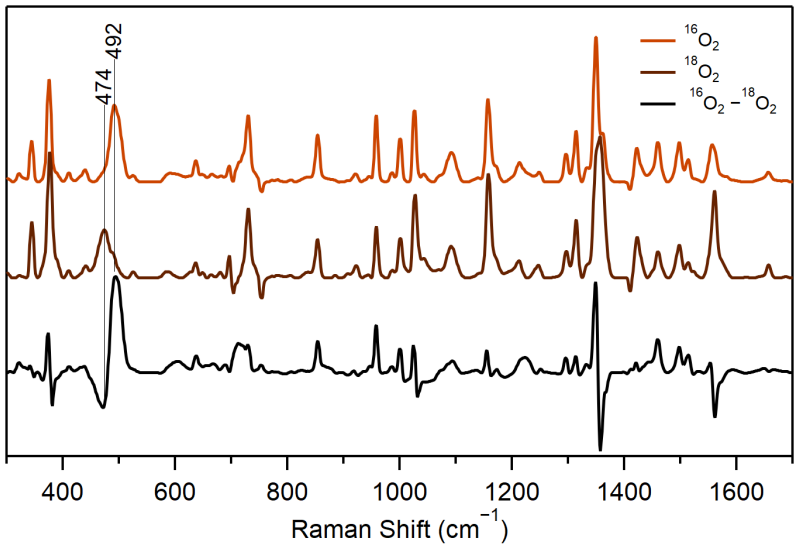

Figure S3. Resonance Raman spectra (λ_{ex}= 457 nm) collected from 2 mM frozen solution samples in 9:1 DCM:THF of (A) $[(THF)(TPP)Fe^{III}(O_2^{2-})]^-$ (B) $[(ArS^-)(TPP)Fe^{III}(O_2^{2-})]^{2-}$ (C) $[(ArO^-)(TPP)Fe^{III}(O_2^{2-})]^{2-}$ (D)$[(ArO^-)(F_{20}TPP)Fe^{III}(O_2^{2-})]^{2-}$ prepared with $^{16}O_2$(g) (light color) and $^{18}O_2$(g) (dark color); difference spectrum is shown in black.

Table S1. Spectroscopic characterization details of axially ligated ferric heme peroxo complexes.

Heme-PO Complex	UV-vis (Soret) (nm)	UV-vis (Q-Bands) (nm)	rR ν(Fe–O) (cm^{-1})	rR ν(O–O) (cm^{-1})	Binding Mode	EPR (g)	Ref
$[(THF)(TPP)Fe^{III}(O_2^{2-})]^-$	436 (-40 °C; 9:1 DCM:THF)	564 (-40 °C; 9:1 DCM:THF)	472 ($\Delta^{18}O_2$ = –21)	807 ($\Delta^{18}O_2$ = –45)	Side-on	4.2	This work
$[(THF)(F_{20}TPP)Fe^{III}(O_2^{2-})]^-$	432 (-80 °C; THF)	557 (-80 °C; THF)	469 ($\Delta^{18}O_2$ = –15)	808 ($\Delta^{18}O_2$ = –41)	Side-on	4.2	22
$[(4\text{-MeIm})(TPP)Fe^{III}(O_2^{2-})]^-$	436 (-40 °C; 9:1 DCM:THF)	565 (-40 °C; 9:1 DCM:THF)	479 ($\Delta^{18}O_2$ = –23)	803 ($\Delta^{18}O_2$ = –47)	Side-on	4.2	This work
$[(ArS^-)(TPP)Fe^{III}(O_2^{2-})]^{2-}$	436 (-40 °C; 9:1 DCM:THF)	564 (-40 °C; 9:1 DCM:THF)	484 ($\Delta^{18}O_2$ = –21)	-	Side-on	4.2 & 2.28, 2.13,1.97	This work
$[(ArO^-)(TPP)Fe^{III}(O_2^{2-})]^{2-}$	436 (-40 °C; 9:1 DCM:THF)	565 (-40 °C; 9:1 DCM:THF)	474 ($\Delta^{18}O_2$ = –21)	-	Side-on	-	This work
$[(ArO^-)(F_{20}TPP)Fe^{III}(O_2^{2-})]^{2-}$	432 (-40 °C; 9:1 DCM:THF)	556 (-40 °C; 9:1 DCM:THF)	492 ($\Delta^{18}O_2$ = –18)	-	Side-on	-	This work
$[(TMPIm)Fe^{III}(O_2^{2-})]^-$	440 (-30 °C; 1:4 MeCN:THF)	574 (-30 °C; 1:4 MeCN:THF)	475 ($\Delta^{18}O_2$ = –20)	807 ($\Delta^{18}O_2$ = –49)	Side-on	4.2	23
$[(DMSO)(TMP)Fe^{III}(O_2^{2-})]^-$	-	-	476 ($\Delta^{18}O_2$ = –21)	807 ($\Delta^{18}O_2$ = –45)	Side-on	-	23
$[(F_8TPPIm)Fe^{III}(O_2^{2-})]^-$	424 (-80 °C; THF)	535 & 567 (-80 °C; THF)	578 ($\Delta^{18}O_2$ = –26)	810 ($\Delta^{18}O_2$ = –34)	End-on	2.25, 2.14 & 1.95	24
$[(TMP_{Im}^{Xan})Fe^{III}(O_2^{2-})]^-$	430 (-70 °C; 1:4 MeCN:THF)	568 (-70 °C; 1:4 MeCN:THF)	585 ($\Delta^{18}O_2$ = –25)	808 ($\Delta^{18}O_2$ = –37)	End-on	2.27, 2.16 & 1.96	25
$[(THF)(F_{20}TPP)Fe^{III}(OOH)]$	415 (-80 °C; THF)	530, 553 (-80 °C; THF)	597 ($\Delta^{18}O_2$ = –30)	-	End-on	2.26, 2.15, 1.96	22

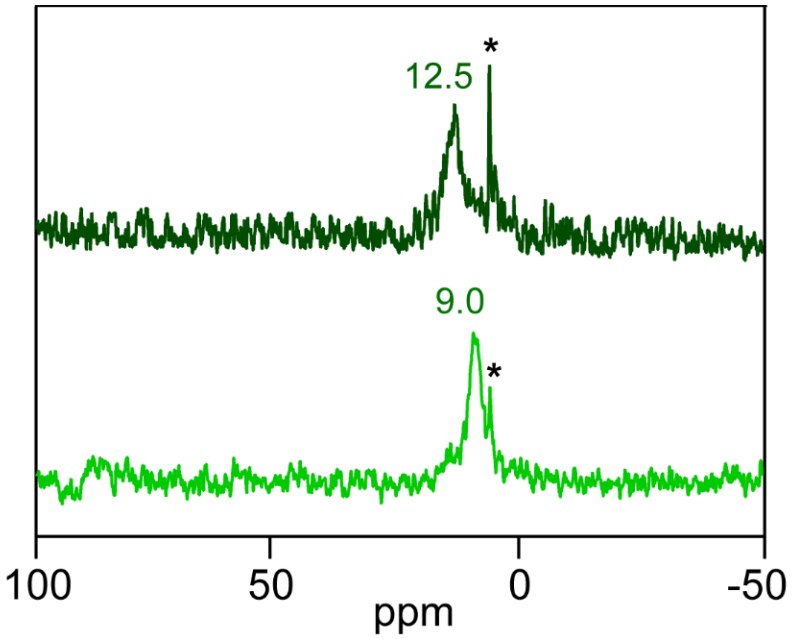

Figure S4. ^{2}H NMR spectra (in 9:1 DCM:THF at −40 °C) for [(4-DMAP)(TPP-*d*$_8$)Fe^{III}(O_2^{2-})]$^-$ (dark green, top), and (B) [(DCHIm)(TPP-*d*$_8$)Fe$^{III}O_2^{2-}$)]$^-$ (light green, bottom). *peaks correspond to the solvent.

(A)

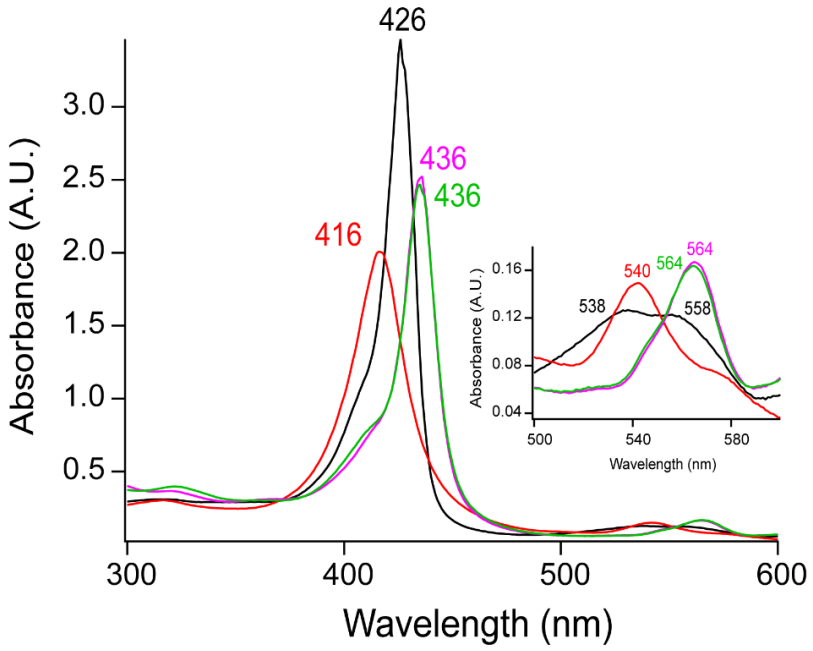

(B)

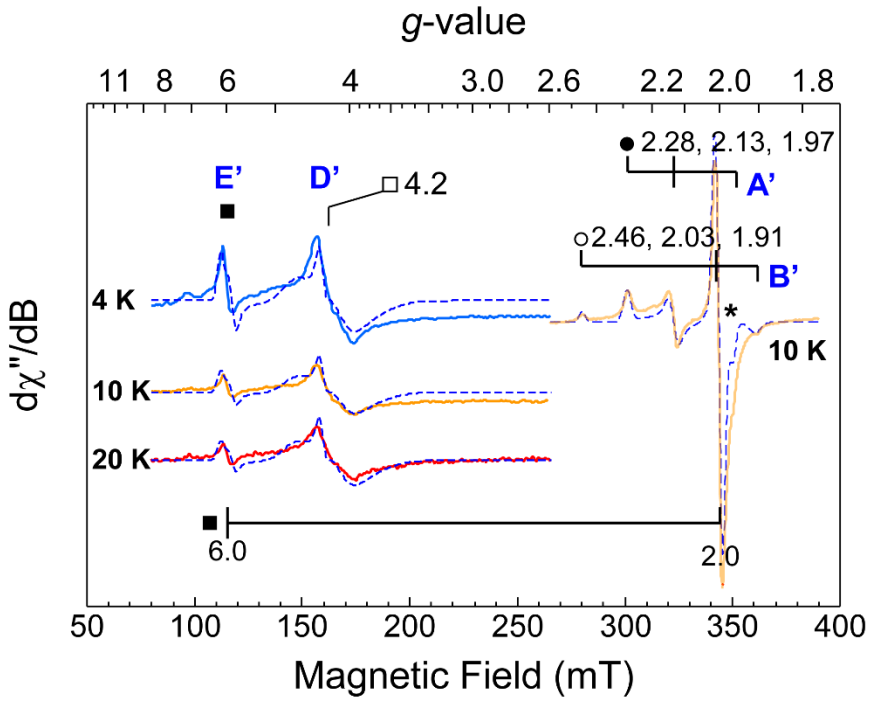

Figure S5. (A) UV−vis spectra (in 9:1 DCM:THF at −40 °C) for 50 μM solutions of $[(THF)_2(TPP)Fe^{II}]$ (black), $[(THF)(TPP)Fe^{III}(O_2^{-\bullet})]$ (red), $[(THF)(TPP)Fe^{III}(O_2^{2-})]^-$ (Pink), $[(ArS^-)(TPP)Fe^{III}(O_2^{2-})]^{2-}$ (Green). Inset shows the expanded Q-band region. (B) X-band CW EPR spectra for a 2 mM solution of $[(ArS^-)(TPP)Fe^{III}(O_2^{2-})]^{2-}$ (in frozen 9:1 DCM:THF) samples at selected temperatures, 4 K (blue), 10 K (orange), and 20 K (red). The axial zero field splitting

parameter (*D*) for **E'** (■) and **D'** (□) was determined by matching the experimental and simulated (*blue dashed lines*) signal intensity. Within this temperature regime (4 – 20 K), a single set of spectroscopic parameters (provided in **Table S2**) was used to match experimental signal intensity for species **E'** and **D'**. Low-spin (S = 1/2) ferric sites **A'** and **B'** follow Curie law behavior. *Instrumental parameters*: microwave frequency, 9.631 GHz, microwave power, 67 mW (4K) – 670 mW (20 K); modulation amplitude, 0.92 mT.

Table S2. EPR simulation parameters for **Figure S5**.

Species	Spin	$g_{1,2,3}$	D (cm^{-1})	E/D	[X] (%)
A' (●)	1/2	2.28, 2.13, 1.97	-	-	40 ± 3
B' (○)	1/2	2.46, 2.03, 1.91	-	-	20 ± 2
C' (*)	1/2	2.00, 2.00, 2.00	-	-	4 ± 2
D' (□)	5/2	2.0, 2.0, 2.0	0.9 ± 0.1	0.27	32 ± 4
E' (■)	5/2	2.0, 2.0, 2.0	8.0 ± 1.0	0.005	4 ± 2

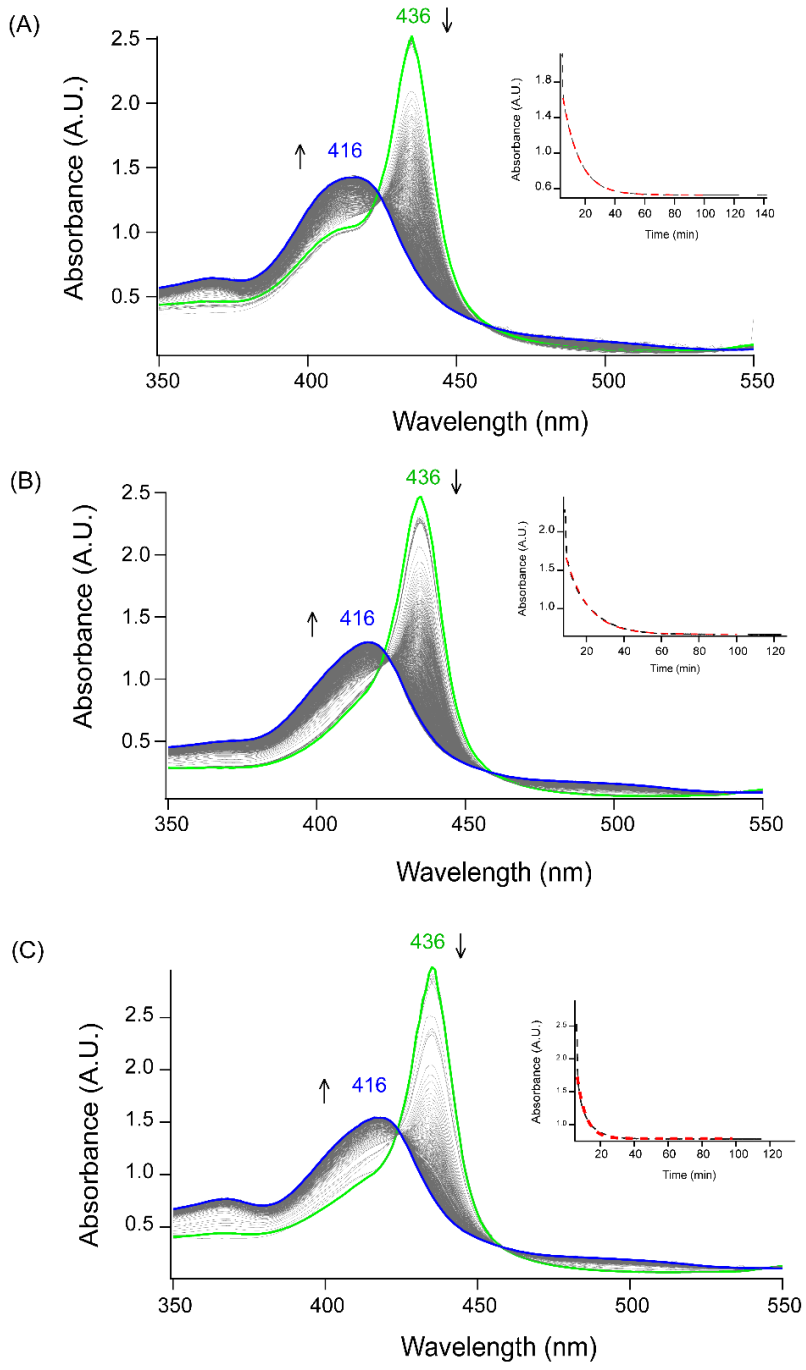

Figure S6. Electronic absorption spectral changes observed (in 9:1 DCM: THF at –40 °C) during the reaction of a 50 μM solution of (A) $[(DCHIm)(TPP)Fe^{III}(O_2^{2-})]^-$ (B) $[(ArO^-)(TPP)Fe^{III}(O_2^{2-})]^{2-}$ (C) $[(ArS^-)(TPP)Fe^{III}(O_2^{2-})]^{2-}$ with 200 equiv of acetophenone oxime (green: initial $[(B)(TPP)Fe^{III}(O_2^{2-})]^-$ complex; blue: final ferric product). Insets show the kinetic time traces (black) at 436 nm overlaid with the exponential fits (red).

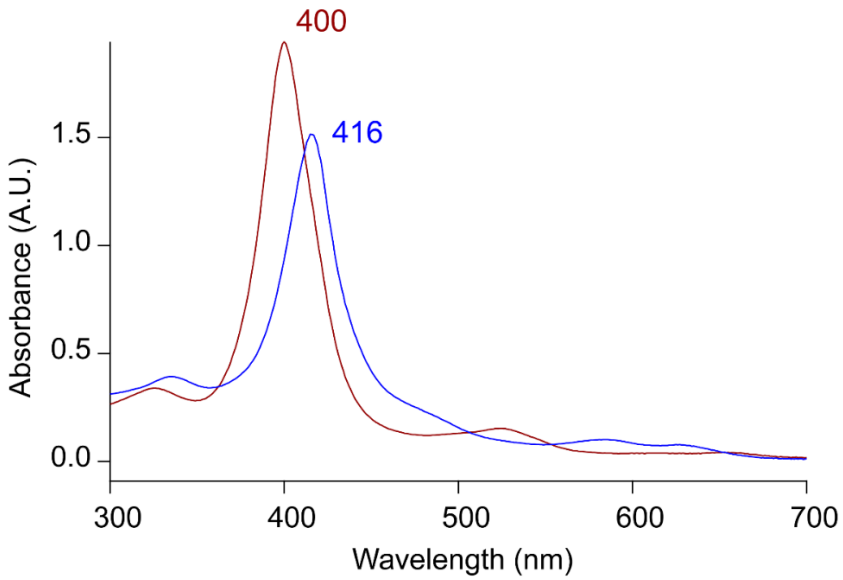

Figure S7. UV−vis spectra (in 9:1 DCM:THF at −40 °C) of naked [(TPP)Fe^{III}]SbF_6 (brown) and upon addition of 1 equiv of TBAOH to form [(TPP)Fe^{III}(OH)] (blue).

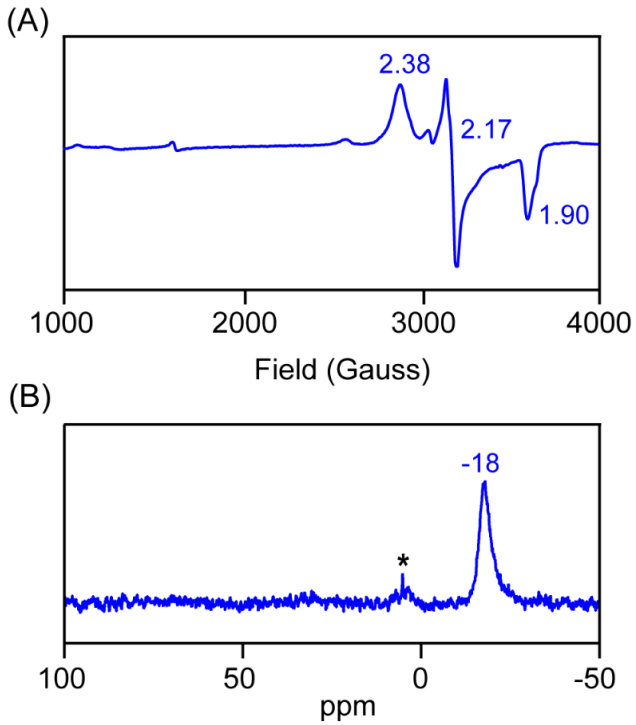

Figure S8. (A) EPR spectral features (in frozen 9:1 DCM:THF at 7 K) (g = 2.38, 2.17 & 1.90) and (B) ^{2}H NMR spectra (in 9:1 DCM:THF at −40 °C) of the final product from the reaction between [(4-MeIm)(TPP-d_8) $Fe^{III}(O_2^{2-})]^-$ and acetophenone oxime.

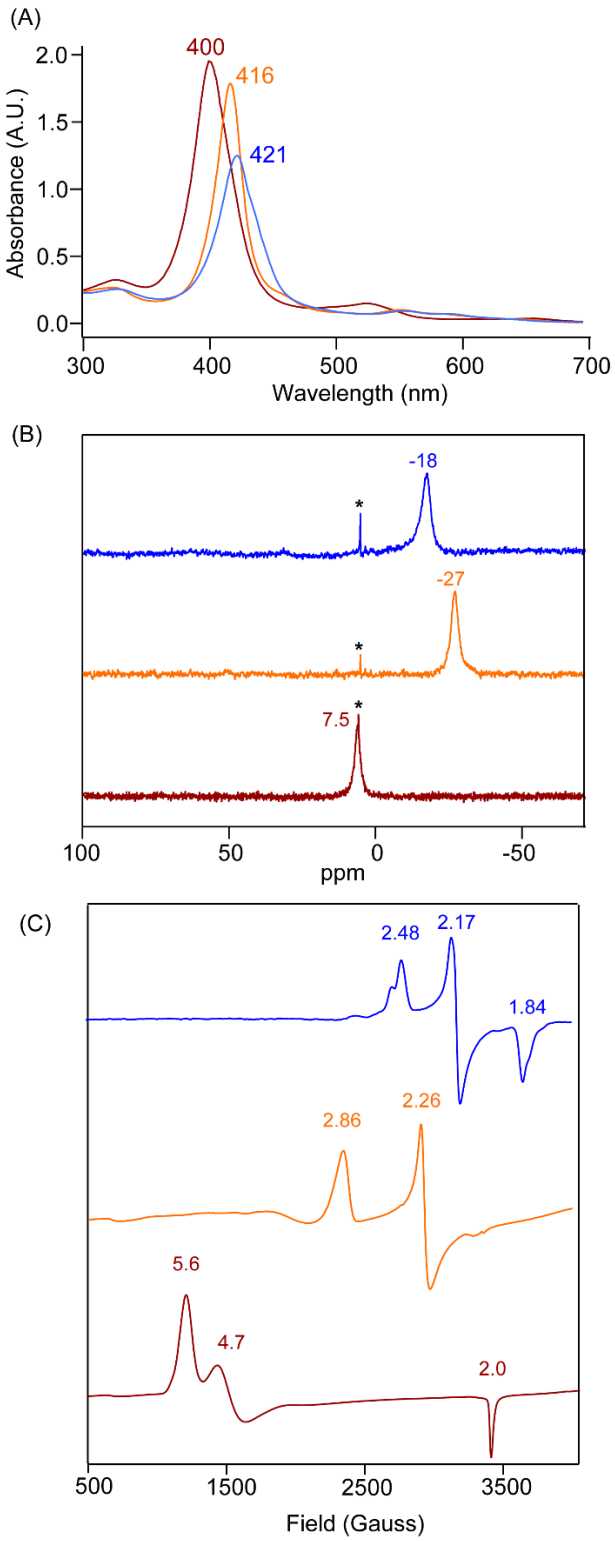

Figure S9. (A) UV−vis (−40 °C), (B) ^{2}H NMR (−40 °C), and (C) EPR (in 7 K) for naked [(TPP-d_8)Fe^{III}]SbF$_6$ (brown), [(4-MeIm)$_2$(TPP-d_8)Fe^{III}]$^+$ (orange), and [(4-MeIm)(TPP-d_8)Fe^{III}(OH)] (blue) in 9:1 DCM:THF; *peaks correspond to the solvent.

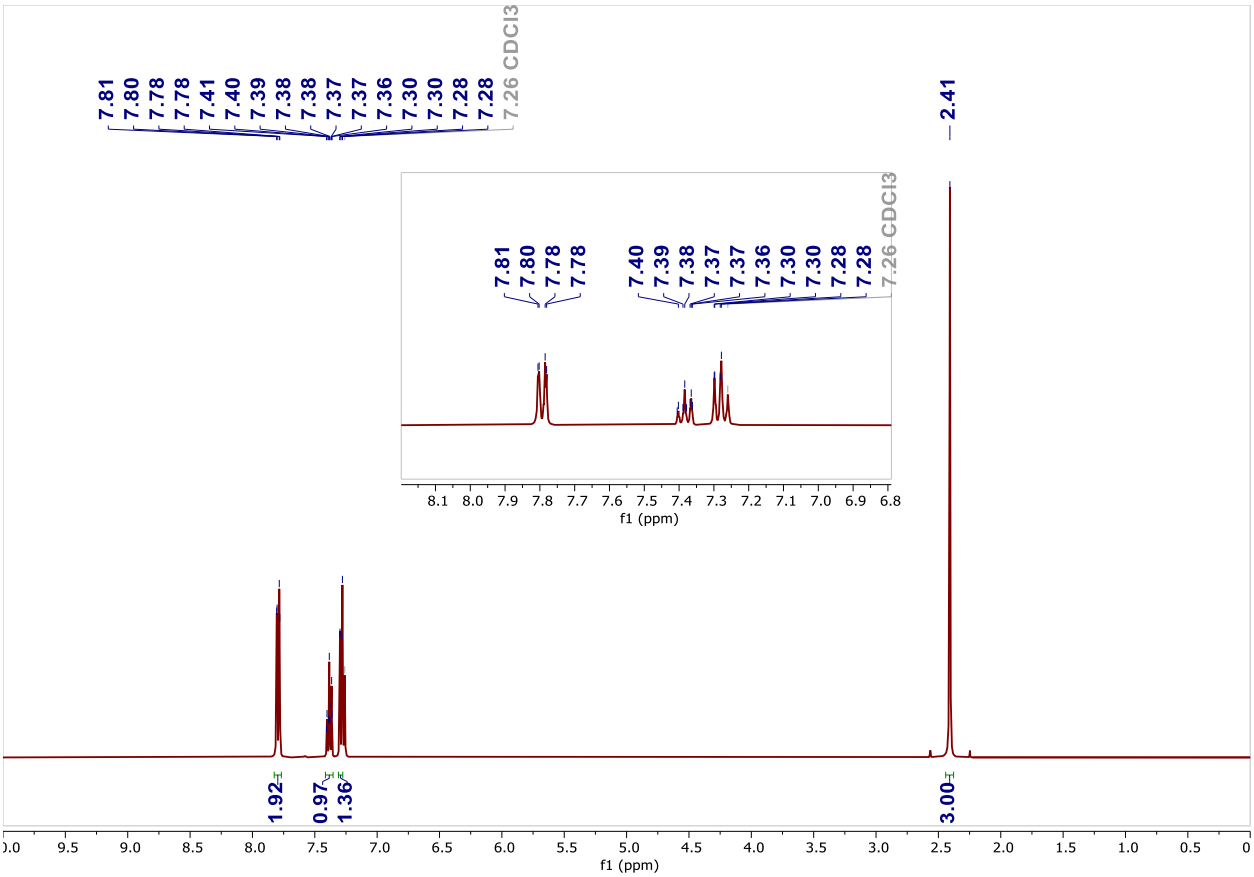

Figure S10. ^{1}H NMR spectrum (in $CDCl_3$ at 25 °C) of the acetophenone product resulted from a reaction between [(4-MeIm) (TPP)Fe^{III} (O_2^{2-})]$^{-}$ and acetophenone oxime.

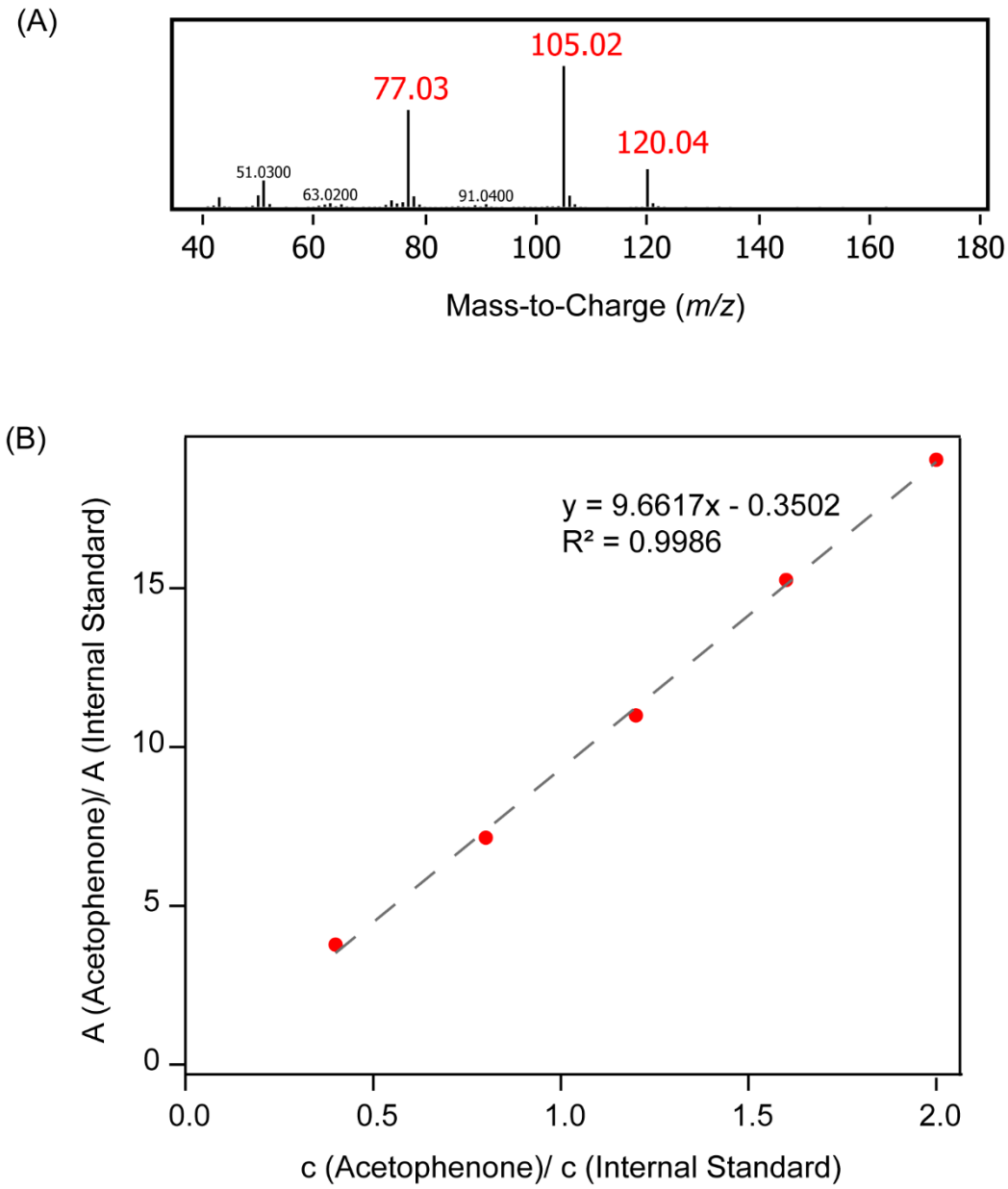

Figure S11. (A) GC-MS data for the acetophenone product resulted from a reaction between [(4-MeIm) (TPP)Fe^{III} (O_2^{2-})]$^-$ and acetophenone oxime showing $[M]^+$ *m/z* = 120.04 (calc. 120.0). (B) GC-FID generated calibration curve for acetophenone using n-dodecane as an internal standard.

(A)

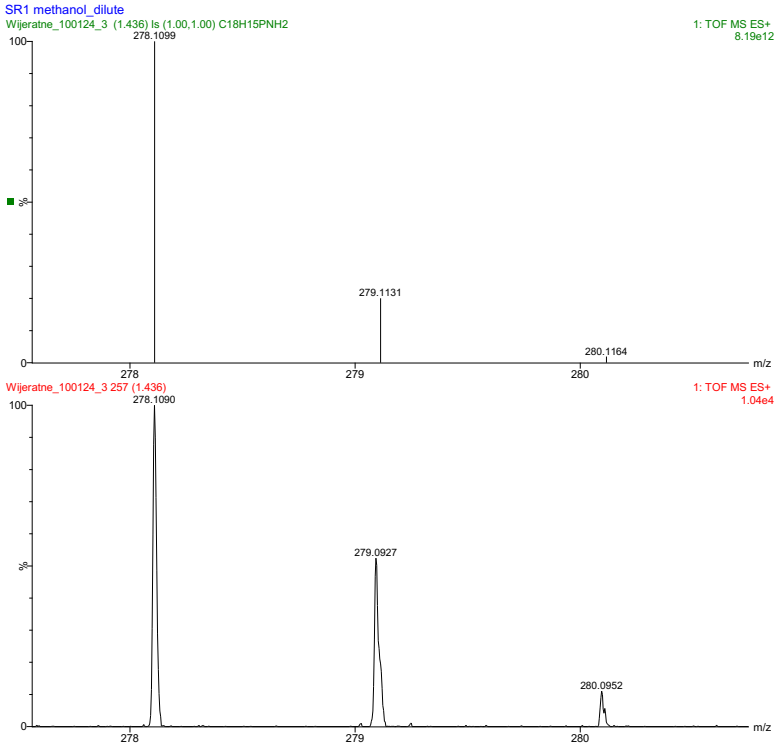
SR1 methanol_dilute
Wijeratne_100124_3 (1.436) Is (1.00,1.00) C18H15PNH2
1: TOF MS ES+
8.19e12
278.1099
279.1131
280.1164
Wijeratne_100124_3 257 (1.436)
1: TOF MS ES+
1.04e4
278.1090
279.0927
280.0952
m/z

(B)

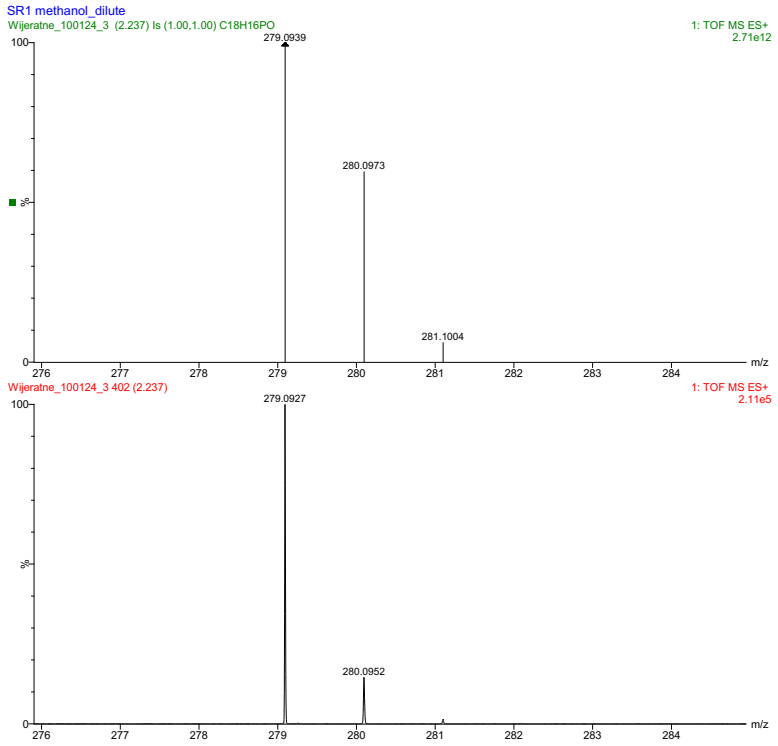
SR1 methanol_dilute
Wijeratne_100124_3 (2.237) Is (1.00,1.00) C18H16PO
1: TOF MS ES+
2.71e12
279.0939
280.0973
281.1004
Wijeratne_100124_3 402 (2.237)
1: TOF MS ES+
2.11e5
279.0927
280.0952
m/z

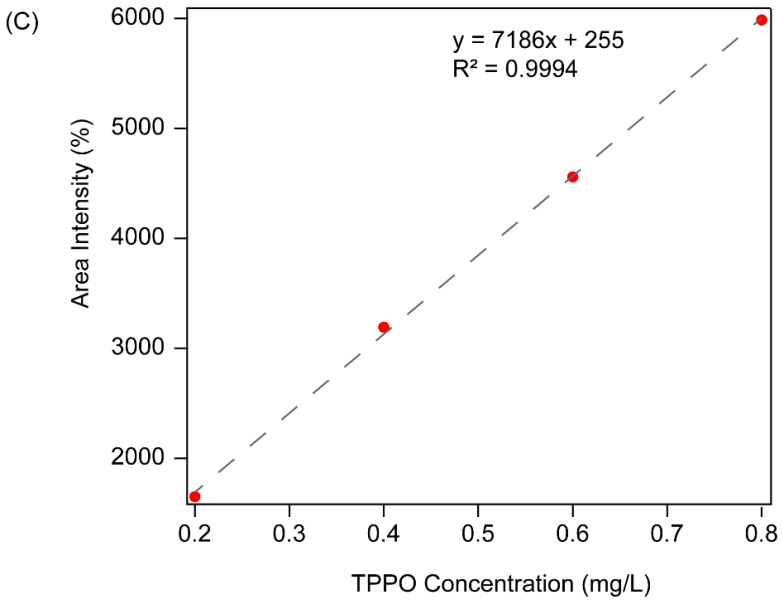

Figure S12. LC-MS data for (A) $Ph_3P{=}NH$ showing [M+H]+ m/z = 278.10 (calc. 278.10), and (B) $Ph_3P{=}O$ showing [M+H]+ m/z = 279.09 (calc. 279.09) obtained from the reaction between [(4-MeIm)(TPP)$Fe^{III}(O_2^{2-})$]$^-$ and acetophenone oxime in presence of 50 equiv. of PPh_3.(C) LC-MS generated calibration curve for $Ph_3P{=}O$ in MeCN/H_2O (70/30). Control experiments indicate <1% yield when heme is not present.

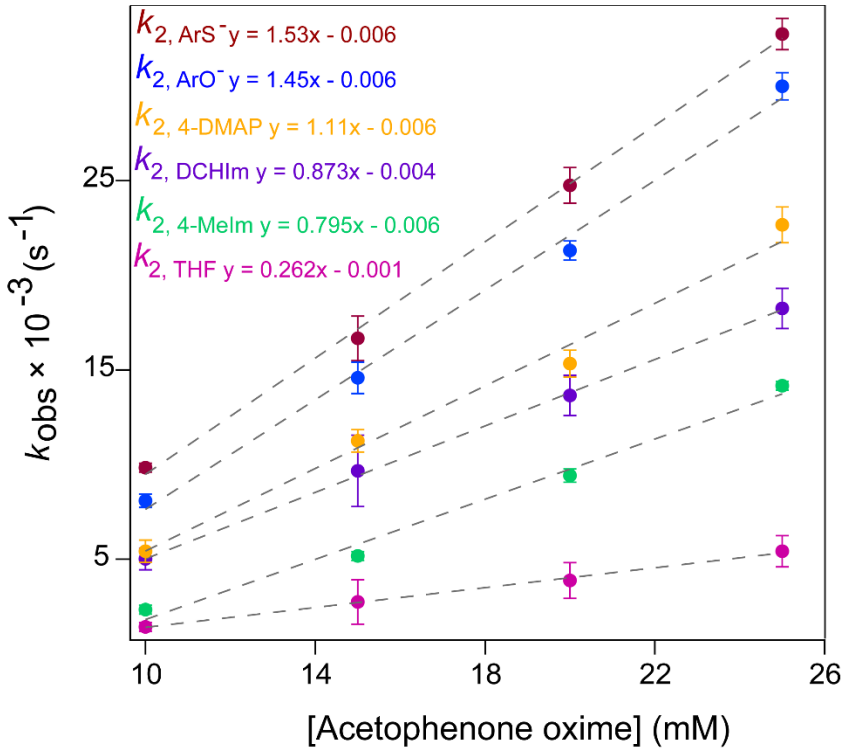

Figure S13. The dependence of pseudo-first-order rate constants (k_{obs}) on the acetophenone oxime concentration for a 50 μM [(B)[(TPP)Fe^{III}(O_2^{2-})]$^-$ in 9:1 DCM:THF at −40 °C. B = ArS^- (brick red), ArO^- (blue), 4-DMAP (orange), DCHIm (purple), 4-MeIm (green) or THF (magenta).

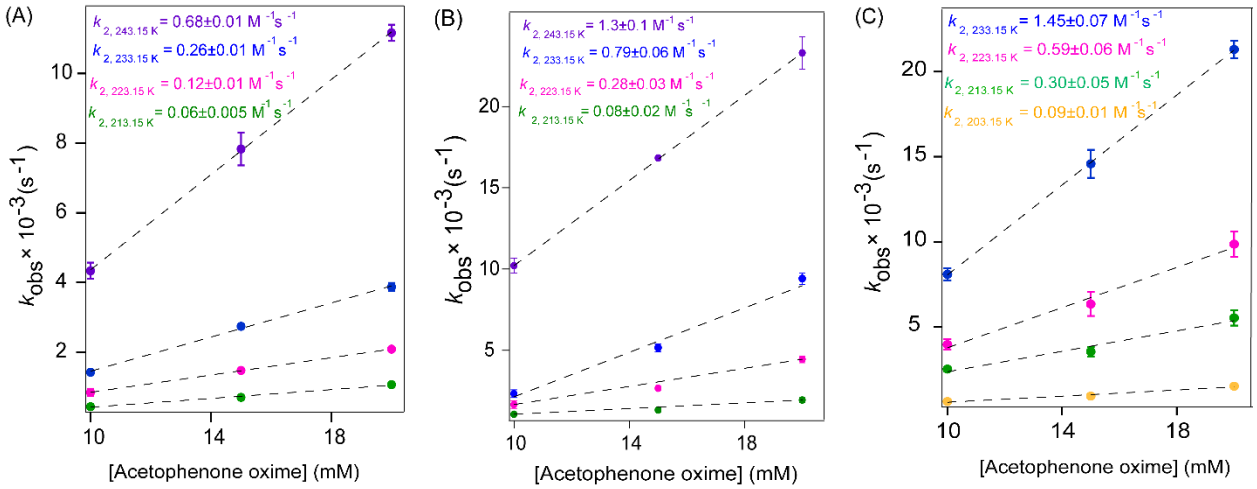

Figure S14. Variable-temperature kinetic plots showing the dependence of pseudo-first-order rate constants (k_{obs}) on acetophenone oxime concentration (with best fit lines) resulting from a 50 μM solution of (A) [(THF)(TPP)Fe^{III}(O_2^{2-})]$^-$, (B) [(4-MeIm)(TPP)Fe^{III}(O_2^{2-})]$^-$, and (C) [(ArO^-)(TPP)Fe^{III}(O_2^{2-})]$^{2-}$ in 9:1 DCM:THF.

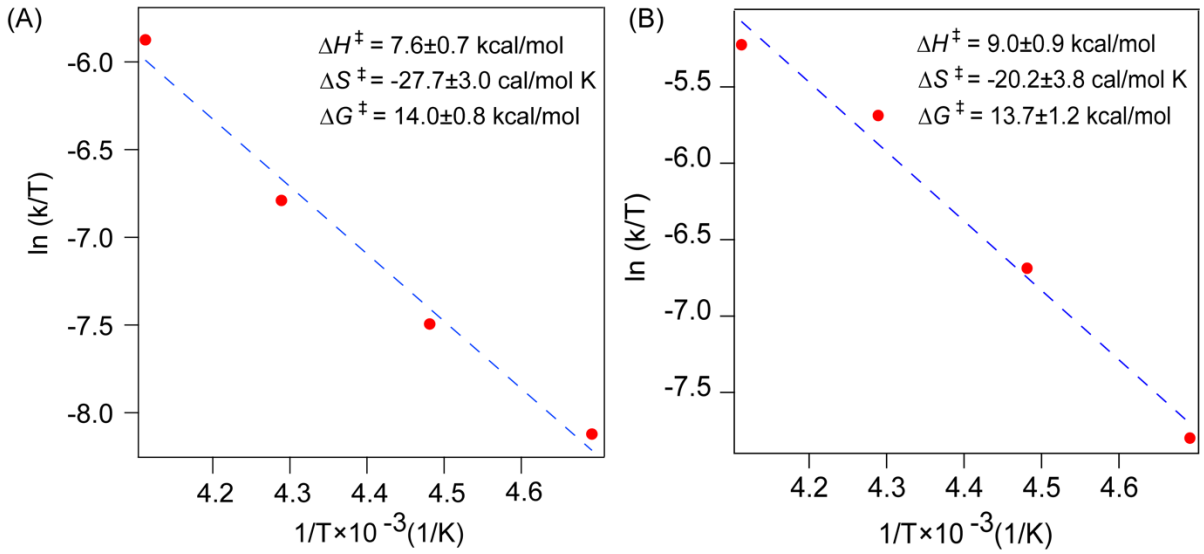

Figure S15. Eyring plot showing ln(k/T) versus 1/T for the reaction of a 50 μM solution of (A) $[(THF)(TPP)Fe^{III}(O_2^{2-})]^-$ and (B) $[(4\text{-MeIm})(TPP)Fe^{III}(O_2^{2-})]^-$ with acetophenone oxime substrate resulting from the data shown in Figure S18 (solvent = 9:1 DCM:THF).

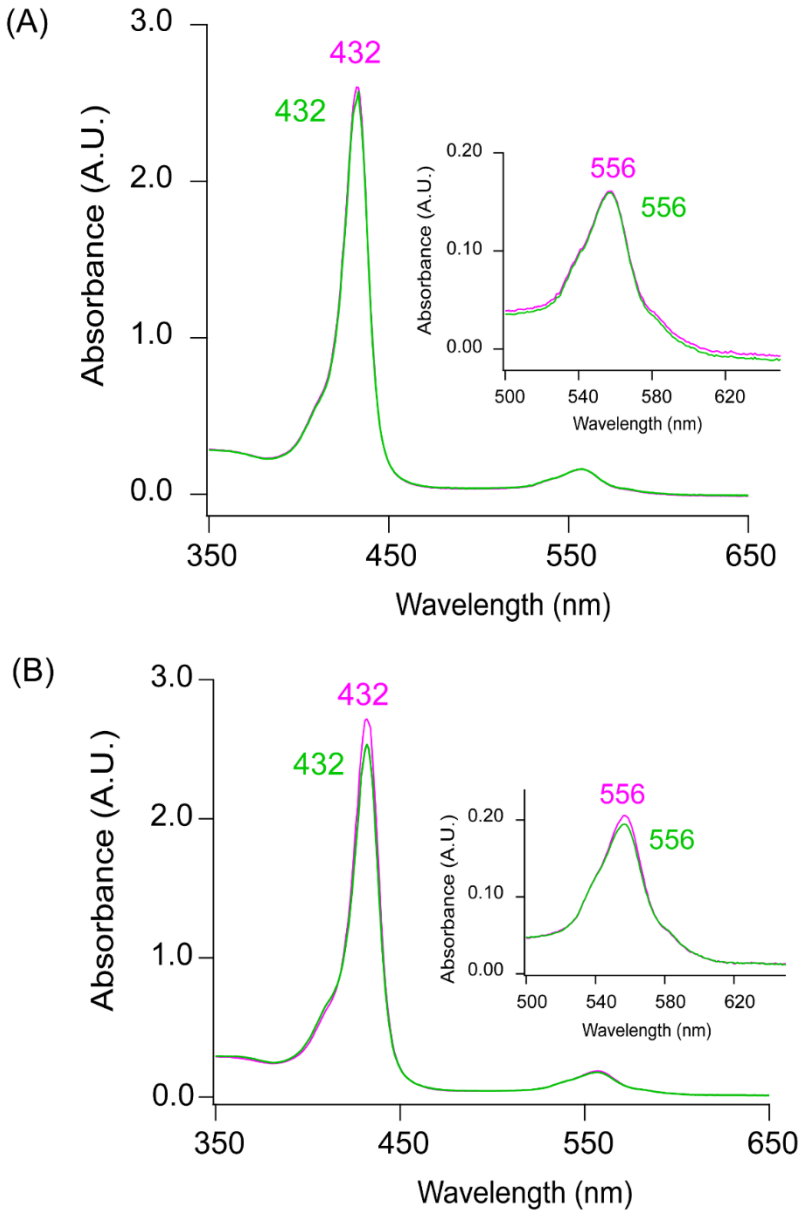

Figure S16. (A) UV−vis spectra (in 9:1 DCM:THF at −40 °C) for 50 μM solutions of $[(THF)(F_{20}TPP)Fe^{III}(O_2^{2-})]^-$ (Purple) and (A) $[(4\text{-MeIm})(F_{20}TPP)Fe^{III}(O_2^{2-})]^-$ (Green) and (B) $[(ArS^-)(F_{20}TPP)Fe^{III}(O_2^{2-})]^{2-}$ (Green). Inset shows the expanded Q-band region.

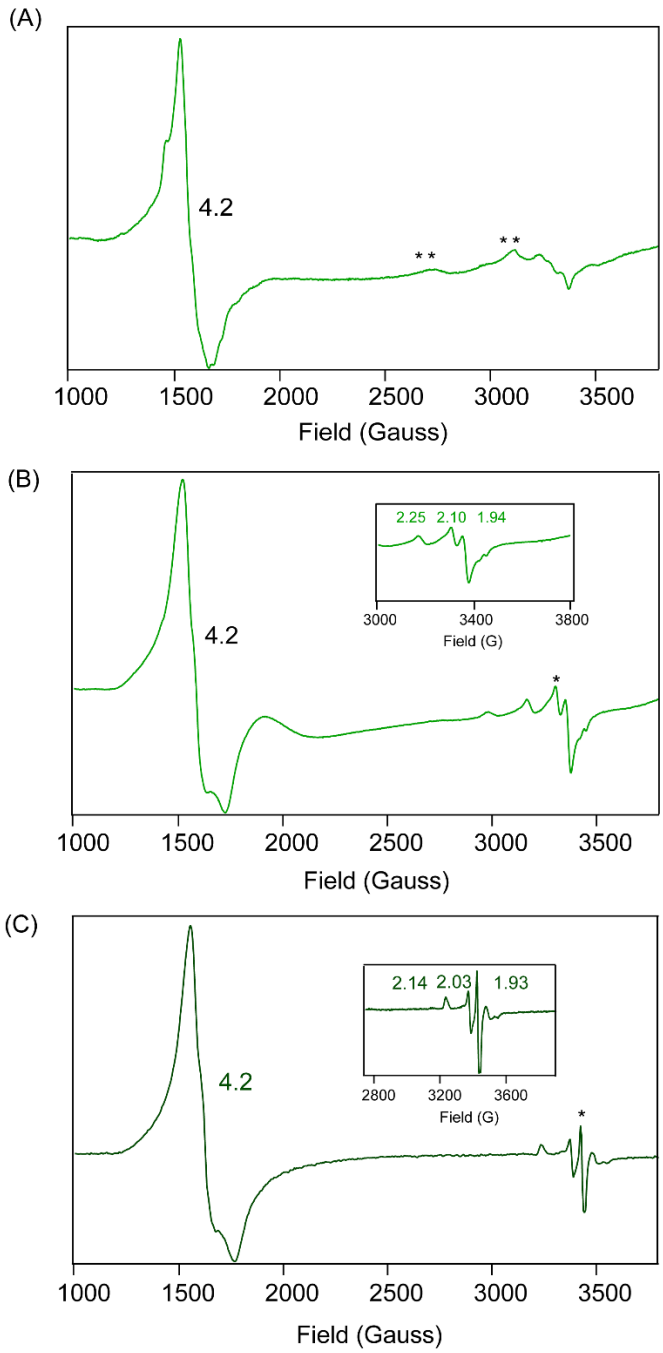

Figure S17. EPR spectral features (in frozen 9:1 DCM:THF at 7 K) for 2 mM solutions of (A) [(4-MeIm)(F_{20}TPP)$Fe^{III}(O_2^{2-})$]$^-$ (**low spin Fe feature (g = 2.4, 2.1) corresponds to decay product), (B) [(4-DMAP)(F_{20}TPP)$Fe^{III}(O_2^{2-})$]$^-$ and (C) [(DCHIm)(F_{20}TPP)$Fe^{III}(O_2^{2-})$]$^-$ (* feature (g = 1.99) corresponds to an excess of cobaltocene).

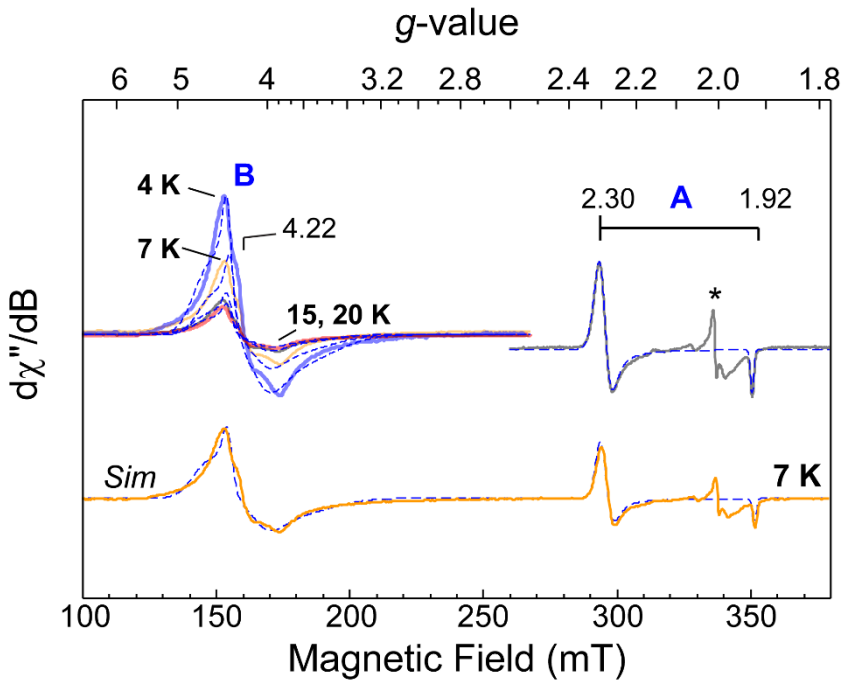

Figure S18. X-band CW EPR spectra of $[(ArS^{-})(F_{20}TPP)Fe^{III}(O_2^{2-})]^{2-}$ samples at selected temperatures, 4 K (blue), 7 K (orange), 10 K, (black), and 20 K (red). The axial zero field splitting parameter (D) for the high-spin species **B** was determined by matching the experimental and simulated (*blue dashed lines*) signal. Within this temperature regime (4 – 20 K), a single set of spectroscopic parameters was used to match the experimental signal intensity. The low-spin (S = 1/2) follows the Curie–Weiss law behavior and thus only a single spectrum collected under non-saturating conditions (7 K, 67 mW) was used for simulation. *Instrumental parameters*: microwave frequency, 9.626 GHz, microwave power, 21 mW (4K) – 211 mW (20 K); modulation amplitude, 0.92 mT. Simulation parameters and analytical quantitation of species are provided in **Table S3**. The sharp signal observed at $g \sim 2$ (*) is attributed to residual cobaltocene.

Table S3. EPR simulation parameters for **Figure S18**.

Species	Spin	$g_{1,2,3}$	D (cm^{-1})	E/D	[X] (%)
A	1/2	2.31, 2.29, 1.92	-	-	18 ± 2
B	5/2	2.0, 2.0, 2.0	0.6 ± 0.1	0.24	82 ± 7

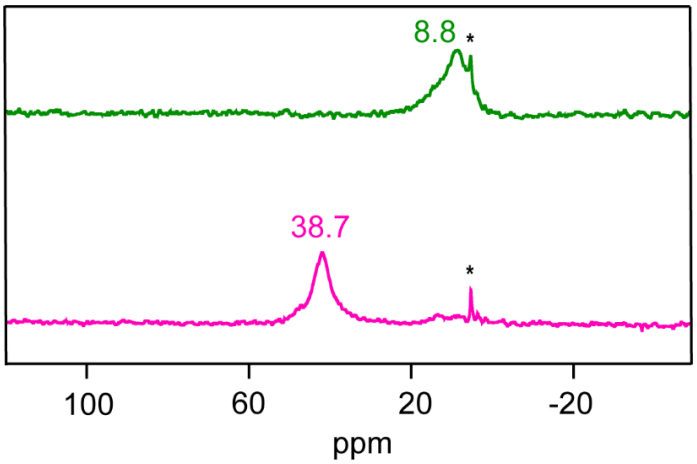

Figure S19. ^{2}H NMR spectra (in 9:1 DCM:THF at −40 °C) for [(F_{20}TPP-d_8) $Fe^{III}(O_2^{2-})]^-$ (pink), and [(4-MeIm)(F_{20}TPP-d_8)$Fe^{III}(O_2^{2-})]^-$ (green); *peaks correspond to the solvent.

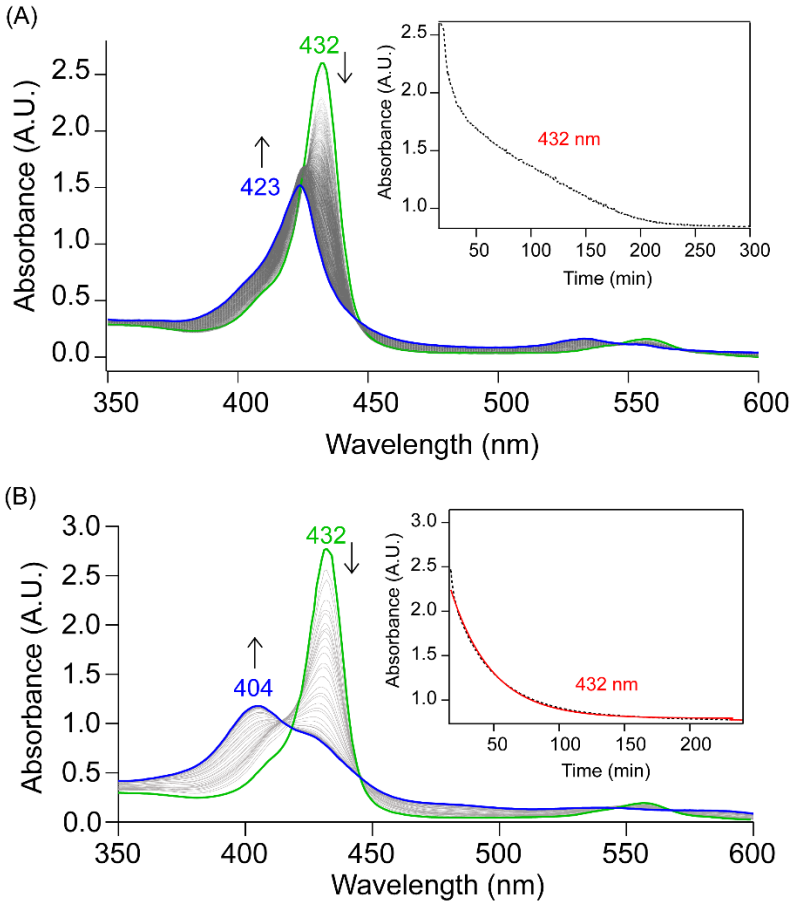

Figure S20. Electronic absorption spectral changes (in 9:1 DCM:THF at –40 °C) in the presence of 500 equiv of acetophenone oxime (A) [(DCHIm)(F_{20}TPP)$Fe^{III}(O_2^{2-})]^-$ and (B) [(ArS^-)(F_{20}TPP)$Fe^{III}(O_2^{2-})]^{2-}$ (green: initial [(B)(F_{20}TPP)$Fe^{III}(O_2^{2-})]^-$ and blue: final heme product). Insets show the kinetic time traces at 432 nm (red line shows the exponential fit).

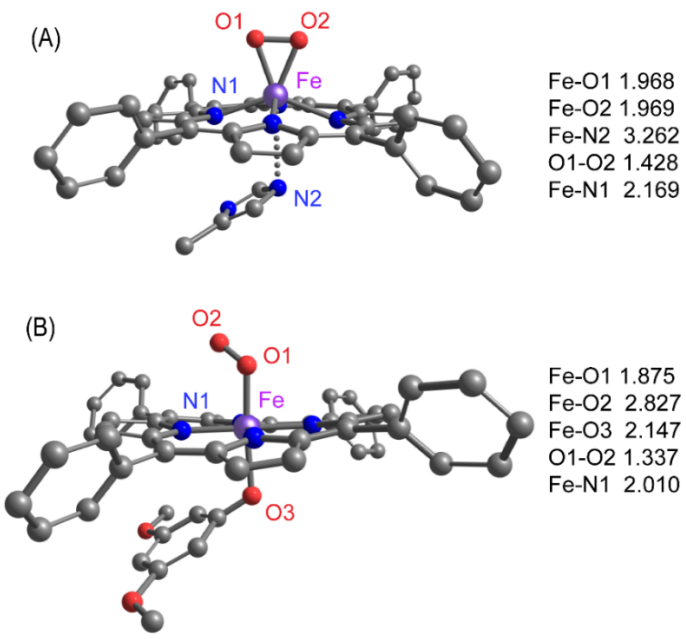

Figure S21. Optimized geometries of (A) $[(4\text{-MeIm})(TPP)Fe^{III}(O_2^{2-})]^{-}$, (B) $[(ArO^{-})(TPP)Fe^{III}(O_2^{2-})]^{2-}$; key bond lengths are shown next to each structure in Å.

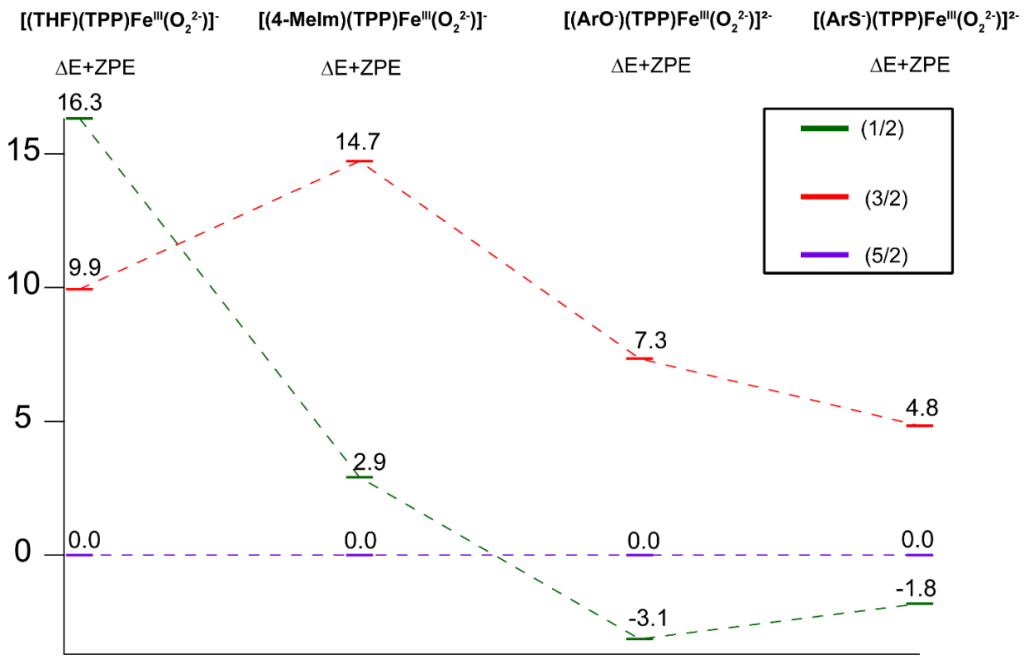

Figure S22. Sextet (purple)/quartet (red)/doublet (green) spin-state energies for the heme-PO complexes with different axial ligands. All energies are presented with respect to the sextet spin state in kcal mol^{-1}.

Table S4. Bond lengths (Å) and bond angles (degree) of the optimized heme-PO structures.

	[(THF)(TPP)Fe^{III}(O_2^{2-})]$^-$	**[(4-MeIm)(TPP)Fe^{III}(O_2^{2-})]$^-$**	**[(ArO^-)(TPP)Fe^{III}(O_2^{2-})]$^{2-}$**	**[(ArS^-)(TPP)Fe^{III}(O_2^{2-})]$^{2-}$**
Fe-O1[a]	1.980	1.968	1.875	1.898
Fe-O2[a]	1.977	1.969	2.827	2.845
O1-O2[a]	1.427	1.428	1.337	1.331
Fe-N_{Por}[b]	2.159	2.169	2.010	2.004
Fe-L[c]	4.446	3.262	2.147	2.549
Fe-O1-O2[d]	68.72	68.74	122.45	122.53

[a]bond distances in Å; [b]average value; [c]bond distances between Fe and axially coordinating atom of the ligand in Å; [d]value of the angle ∠Fe-O_{peroxo}-O_{peroxo}.

Table S5. *ν*(Fe-O) and ν(O-O) frequencies, and natural charges for the optimized heme-PO structures.

	[(THF)(TPP)Fe^{III}(O_2^{2-})]$^-$	[(4-MeIm)(TPP)Fe^{III}(O_2^{2-})]$^-$	[(ArO^-)(TPP)Fe^{III}(O_2^{2-})]$^{2-}$	[(ArS^-)(TPP)Fe^{III}(O_2^{2-})]$^{2-}$
ν(Fe-O) /cm^{-1}	407 ($\Delta^{18}O$ = 14)[a]	414 ($\Delta^{18}O$ =15)[a]	505 ($\Delta^{18}O$ =17)[a]	465 ($\Delta^{18}O$ =14)[a]
ν(O-O) /cm^{-1}	899 ($\Delta^{18}O$ = 52)[a]	896 ($\Delta^{18}O$ = 51)[a]	1003 ($\Delta^{18}O$ = 64)[a]	1015 ($\Delta^{18}O$ = 63)[a]
Natural Atomic Charge-Fe	0.937	0.929	0.214	0.047
Natural Atomic Charge-O1	-0.417	-0.411	-0.152	-0.149
Natural Atomic Charge-O2	-0.418	-0.410	-0.439	-0.420

[a]Isotopic substitution $\Delta^{18}O$ is included in the brackets.

Cartesian coordinates of optimized geometries

[(THF)(TPP)Fe^{III}(O_2^{2-})]$^-$ (uB97D-def2-TZVP) Charge: -1, Multiplicity: 6

26	-0.067379000	0.021975000	-0.991756000	6	-6.599912000	2.894896000	-1.035439000	1	3.062967000	4.043767000	1.792450000
7	1.914159000	0.609320000	-0.279867000	1	-5.111699000	1.675840000	-2.018331000	6	2.857821000	6.510813000	-1.194662000
7	0.532264000	-1.942112000	-0.401340000	6	-6.920912000	3.635470000	0.107564000	1	1.637890000	5.001858000	-2.143736000
7	-2.039369000	-0.582396000	-0.292584000	1	-6.239331000	4.295547000	2.049137000	6	3.588774000	6.862301000	-0.054410000
7	-0.656118000	1.973164000	-0.341919000	1	-7.312000000	2.818678000	-1.854783000	1	4.223848000	6.237170000	1.914505000
6	1.825592000	-2.404602000	-0.380319000	1	-7.884335000	4.135101000	0.183740000	1	2.798621000	7.195933000	-2.038054000
6	1.826979000	-3.847588000	-0.283259000	6	-2.389412000	-4.339185000	-0.067207000	1	4.096916000	7.823096000	-0.004540000
6	0.522032000	-4.243008000	-0.234861000	6	-2.235795000	-5.124457000	1.086900000	1	4.450866000	2.785673000	-0.234921000
6	-0.282949000	-3.042447000	-0.288877000	6	-3.227174000	-4.805849000	-1.092735000	1	5.233458000	0.213301000	-0.305866000
6	-1.689596000	-3.025969000	-0.197204000	6	-2.899872000	-6.347741000	1.212039000	1	2.710372000	-4.470721000	-0.236094000
6	-2.491997000	-1.868931000	-0.175986000	1	-1.593889000	-4.765716000	1.888242000	1	0.138457000	-5.251415000	-0.153716000
6	-3.926839000	-1.869488000	0.036313000	6	-3.891275000	-6.029859000	-0.971024000	1	-4.537543000	-2.750331000	0.187146000
6	-4.324042000	-0.565324000	0.034266000	1	-3.352216000	-4.202165000	-1.988903000	1	-5.322173000	-0.174323000	0.183799000
6	-3.131628000	0.233706000	-0.175860000	6	-3.729556000	-6.805324000	0.182219000	1	-2.821588000	4.508464000	-0.111895000
6	-3.109774000	1.642333000	-0.192900000	1	-2.772957000	-6.940985000	2.115537000	1	-0.246964000	5.282179000	-0.113306000
6	-1.946623000	2.436912000	-0.252950000	1	-4.532703000	-6.378610000	-1.777885000	8	-0.510395000	0.412681000	3.414831000
6	-1.942177000	3.881845000	-0.179186000	1	-4.246817000	-7.757705000	0.278298000	6	-0.371221000	-0.930177000	2.909120000
6	-0.635660000	4.274883000	-0.185355000	6	4.301795000	-2.323672000	-0.340900000	6	0.661533000	1.100820000	2.934579000
6	0.164824000	3.074173000	-0.284685000	6	5.145402000	-2.247701000	0.779580000	6	1.126683000	-1.281717000	3.045447000
6	1.574052000	3.056111000	-0.249757000	6	4.714267000	-3.090018000	-1.443270000	1	-1.034556000	-1.576009000	3.496768000
6	2.375527000	1.897162000	-0.246408000	6	6.371170000	-2.918658000	0.797888000	1	1.825449000	0.107703000	3.113760000
6	3.825918000	1.902213000	-0.246404000	1	4.829344000	-1.661397000	1.639380000	1	0.536192000	1.345936000	1.871176000
6	4.222488000	0.598604000	-0.283195000	6	5.940621000	-3.760287000	-1.428433000	1	0.767662000	2.023683000	3.517513000
6	3.014706000	-0.204120000	-0.301797000	1	4.066916000	-3.152625000	-2.314997000	1	2.574431000	0.232314000	2.325885000
6	2.990924000	-1.611061000	-0.355969000	6	6.773681000	-3.676969000	-0.307178000	1	2.310581000	0.248998000	4.086745000
8	0.623117000	0.254804000	-2.830026000	1	7.009630000	-2.852628000	1.676840000	1	1.466446000	-1.869906000	2.188313000
8	-0.744422000	-0.154738000	-2.844962000	1	6.246753000	-4.344489000	-2.293914000	1	1.315150000	-1.856168000	3.959913000
6	-4.424935000	2.341935000	-0.088977000	1	7.728166000	-4.199082000	-0.294390000	1	-0.673849000	-0.959926000	1.852932000
6	-4.758332000	3.085808000	1.054743000	6	2.272842000	4.373589000	-0.183922000				
6	-5.362291000	2.252110000	-1.130691000	6	3.009389000	4.736518000	0.955626000				
6	-5.995732000	3.727808000	1.153451000	6	2.204553000	5.276819000	-1.257078000				
1	-4.040947000	3.151905000	1.869541000	6	3.661980000	5.970551000	1.021461000				

[(THF)(TPP)Fe^{III}(O_2^{2-})]$^-$ (uB97D-def2-TZVP) Charge: -1, Multiplicity: 4

26	-0.148823000	-0.039492000	-0.951123000	6	-6.975750000	1.776185000	-1.060547000	1	2.365938000	4.425799000	1.811598000
7	1.763552000	0.880379000	-0.256608000	1	-5.312112000	0.802239000	-2.035513000	6	1.835056000	6.888040000	-1.138702000
7	0.848107000	-1.855015000	-0.462775000	6	-7.407255000	2.477934000	0.070559000	1	0.868334000	5.230823000	-2.131308000
7	-1.884657000	-0.883482000	-0.275558000	1	-6.830386000	3.286817000	1.989747000	6	2.489268000	7.324534000	0.018521000
7	-0.959677000	1.863960000	-0.438604000	1	-7.672024000	1.562987000	-1.869307000	1	3.182954000	6.765671000	1.987771000
6	2.196618000	-2.110083000	-0.432791000	1	-8.440499000	2.810184000	0.147505000	1	1.685933000	7.571714000	-1.972209000
6	2.426648000	-3.538662000	-0.342272000	6	-1.661384000	-4.661507000	-0.032810000	1	2.847136000	8.349444000	0.091831000
6	1.202097000	-4.133698000	-0.293938000	6	-1.357975000	-5.406542000	1.118179000	1	3.926008000	3.431853000	-0.231127000
6	0.217720000	-3.070328000	-0.336252000	6	-2.452413000	-5.255251000	-1.029462000	1	5.105262000	1.013319000	-0.312776000
6	-1.165043000	-3.261625000	-0.190490000	6	-1.828476000	-6.714262000	1.267920000	1	3.397971000	-4.013545000	-0.292439000
6	-2.127693000	-2.231951000	-0.129348000	1	-0.751400000	-4.950523000	1.897427000	1	0.979626000	-5.189525000	-0.211308000
6	-3.527801000	-2.441471000	0.130121000	6	-2.923538000	-6.563195000	-0.883324000	1	-3.989982000	-3.403201000	0.310130000
6	-4.128511000	-1.211168000	0.110344000	1	-2.694029000	-4.683333000	-1.922637000	1	-5.173177000	-0.979603000	0.271770000
6	-3.098143000	-0.242141000	-0.156152000	6	-2.612687000	-7.297551000	0.266542000	1	-3.501353000	4.029571000	-0.210836000
6	-3.316114000	1.150067000	-0.236799000	1	-1.586450000	-7.275650000	2.168278000	1	-1.078312000	5.195802000	-0.162546000
6	-2.307751000	2.120244000	-0.345713000	1	-3.530928000	-7.009375000	-1.668396000	8	-0.621642000	0.192290000	3.378950000
6	-2.532931000	3.550707000	-0.273120000	1	-2.979507000	-8.315417000	0.381777000	6	-0.056237000	-1.039075000	2.884464000
6	-1.305643000	4.141631000	-0.254560000	6	4.618394000	-1.619319000	-0.364502000	6	0.262399000	1.221742000	2.892519000
6	-0.324571000	3.077875000	-0.347340000	6	5.433951000	-1.410031000	0.760624000	6	1.480062000	-0.872081000	2.961052000
6	1.063060000	3.265404000	-0.264237000	6	5.157443000	-2.305572000	-1.465329000	1	-0.445219000	-1.853561000	3.507394000
6	2.022470000	2.228112000	-0.235207000	6	6.752253000	-1.872391000	0.784895000	6	1.681469000	0.664187000	3.090465000
6	3.448419000	2.460923000	-0.239532000	1	5.022082000	-0.884927000	1.619356000	1	0.071535000	1.402330000	1.825516000
6	4.046485000	1.234146000	-0.281397000	6	6.476479000	-2.767733000	-1.444735000	1	0.056218000	2.133977000	3.465103000
6	2.984841000	0.254438000	-0.296897000	1	4.533290000	-2.470992000	-2.340626000	1	2.371561000	1.054667000	2.336502000
6	3.207083000	-1.138201000	-0.382222000	6	7.279113000	-2.552772000	-0.318978000	1	2.059421000	0.922458000	4.087101000
8	0.541095000	0.303161000	-2.755884000	1	7.366678000	-1.706038000	1.667655000	1	1.951520000	-1.264464000	2.056554000
8	-0.702070000	-0.296241000	-2.716315000	1	6.878178000	-3.292564000	-2.309363000	1	1.896030000	-1.396679000	3.828846000
6	-4.730386000	1.618431000	-0.129227000	1	8.305787000	-2.912662000	-0.301483000	1	-0.367064000	-1.196026000	1.842377000
6	-5.175307000	2.319905000	1.002971000	6	1.561326000	4.668327000	-0.171415000				
6	-5.648297000	1.348915000	-1.157211000	6	2.220633000	5.117969000	0.985239000				
6	-6.502294000	2.747650000	1.103166000	6	1.374919000	5.571358000	-1.231090000				
1	-4.472465000	2.523778000	1.807537000	6	2.680077000	6.434031000	1.081367000				

[(THF)(TPP)Fe^{III}(O_2^{2-})]$^-$ (uB97D-def2-TZVP) Charge: -1, Multiplicity: 2

26	0.071795000	0.025009000	-0.724770000	7	-1.160758000	-1.532757000	-0.183101000	7	-1.496390000	1.246217000	-0.559009000

7	1.280567000	1.572162000	-0.123732000
7	1.636126000	-1.202052000	-0.518736000
6	-2.830082000	0.893467000	-0.638016000
6	-3.659522000	2.079094000	-0.682629000
6	-2.829017000	3.146662000	-0.558507000
6	-1.485584000	2.623428000	-0.436366000
6	-0.376110000	3.405984000	-0.123926000
6	0.916519000	2.887551000	0.054844000
6	2.070628000	3.685281000	0.365576000
6	3.154134000	2.853337000	0.295197000
6	2.654242000	1.549410000	-0.043611000
6	3.471024000	0.434628000	-0.296637000
6	2.973021000	-0.848346000	-0.512442000
6	3.803650000	-2.031301000	-0.581310000
6	2.969769000	-3.101839000	-0.523636000
6	1.620042000	-2.582799000	-0.455929000
6	0.497733000	-3.371296000	-0.208219000
6	-0.802217000	-2.856197000	-0.063206000
6	-1.972390000	-3.678023000	0.072389000
6	-3.052392000	-2.846075000	-0.030193000
6	-2.537516000	-1.518198000	-0.213750000
6	-3.338930000	-0.395121000	-0.483654000
8	-0.330758000	-0.510730000	-2.556247000
8	0.532646000	0.569480000	-2.538996000
6	4.949419000	0.640606000	-0.271643000
6	5.736908000	0.113369000	0.764152000
6	5.576938000	1.386389000	-1.282286000
6	7.119213000	0.320549000	0.786905000
1	5.256288000	-0.458409000	1.554695000
6	6.959193000	1.593844000	-1.263357000
1	4.972008000	1.801408000	-2.085412000
6	7.735226000	1.061046000	-0.228006000
1	7.713955000	-0.092408000	1.599346000
1	7.429899000	2.169820000	-2.057691000
1	8.811062000	1.222856000	-0.211397000
6	-0.569590000	4.875034000	0.057863000
6	-1.285071000	5.369666000	1.159914000
6	-0.033778000	5.788688000	-0.863338000
6	-1.463645000	6.744766000	1.336741000
1	-1.699658000	4.666567000	1.878934000
6	-0.212041000	7.164358000	-0.690223000
1	0.522619000	5.412134000	-1.718702000
6	-0.927774000	7.646967000	0.411121000
1	-2.017987000	7.111273000	2.198529000
1	0.205616000	7.858745000	-1.416628000
1	-1.066407000	8.717555000	0.547128000
6	-4.817293000	-0.576214000	-0.536700000
6	-5.537227000	-0.958212000	0.607462000
6	-5.521206000	-0.351290000	-1.730800000
6	-6.925015000	-1.114283000	0.559089000
1	-4.999382000	-1.126997000	1.537538000
6	-6.909456000	-0.506744000	-1.781977000
1	-4.969906000	-0.055012000	-2.620483000
6	-7.616503000	-0.889387000	-0.636814000
1	-7.467249000	-1.405711000	1.456546000
1	-7.438129000	-0.332236000	-2.717044000
1	-8.697104000	-1.010348000	-0.675391000
6	0.682448000	-4.844494000	-0.072369000
6	0.450301000	-5.479443000	1.158913000
6	1.089963000	-5.625092000	-1.166036000
6	0.623147000	-6.859488000	1.294921000
1	0.135337000	-4.880222000	2.010384000
6	1.263778000	-7.005702000	-1.032788000
1	1.266951000	-5.140922000	-2.123778000
6	1.030987000	-7.627974000	0.198641000
1	0.443690000	-7.334036000	2.257702000
1	1.576454000	-7.595783000	-1.892048000
1	1.165798000	-8.702548000	0.303193000
1	-1.967025000	-4.753561000	0.187567000
1	-4.101119000	-3.110109000	-0.013074000
1	-4.739427000	2.075319000	-0.747945000
1	-3.089608000	4.195676000	-0.512165000
1	2.052224000	4.744052000	0.587729000
1	4.196976000	3.096545000	0.450924000
1	4.884969000	-2.027014000	-0.611716000
1	3.231015000	-4.151163000	-0.493182000
8	0.539578000	0.201581000	3.437784000
6	-0.549515000	0.997133000	2.925162000
6	0.287885000	-1.131138000	2.954357000
6	-1.802276000	0.087415000	2.934032000
1	-0.639328000	1.882291000	3.566258000
6	-1.223800000	-1.340990000	3.129115000
1	0.564747000	-1.204335000	1.891659000
1	0.905693000	-1.820057000	3.542691000
1	-1.621677000	-2.053158000	2.400587000
1	-1.438766000	-1.709709000	4.139490000
1	-2.339550000	0.174858000	1.986141000
1	-2.486352000	0.350898000	3.748629000
1	-0.321153000	1.311733000	1.898557000

[(4-MeIm)(TPP)Fe^{III}(O_2^{2-})]$^-$ (uB97D-def2-TZVP) Charge: -1, Multiplicity: 6

7	1.695974000	1.372491000	-0.129074000
7	-1.183741000	1.610546000	-0.477590000
6	3.032703000	1.057225000	-0.086437000
6	3.822507000	2.268037000	-0.050816000
6	2.945646000	3.313164000	-0.092628000
6	1.615983000	2.743791000	-0.134707000
6	0.421280000	3.487495000	-0.177460000
6	-0.874262000	2.933582000	-0.272888000
6	-2.086867000	3.694544000	-0.072231000
6	-3.125157000	2.813143000	-0.151020000
6	-2.552292000	1.509948000	-0.400621000
6	3.562943000	-0.244878000	-0.059882000
6	0.523926000	4.971807000	-0.083788000
6	1.088477000	5.587718000	1.046315000
6	1.176472000	6.979434000	1.133486000
6	0.702261000	7.780617000	0.088767000
6	0.137488000	7.179087000	-1.041445000
6	0.047491000	5.787288000	-1.124660000
6	5.047099000	-0.375768000	0.064283000
6	5.631980000	-0.804201000	1.265941000
6	7.020284000	-0.921661000	1.381194000
6	7.844157000	-0.609716000	0.294129000
6	7.270380000	-0.180509000	-0.907579000
6	5.881687000	-0.065147000	-1.020442000
1	4.903232000	2.309497000	-0.007526000
1	3.175665000	4.370481000	-0.098634000
1	-2.131152000	4.754951000	0.138249000
1	-4.179357000	3.016937000	-0.017599000
1	1.610478000	7.438246000	2.019660000
1	-0.230495000	7.793607000	-1.860644000
1	7.458073000	-1.252979000	2.320760000
1	7.903215000	0.061855000	-1.759030000
6	-3.308947000	0.321131000	-0.452758000
6	2.808661000	-1.432550000	-0.130278000
6	-2.773950000	-0.981076000	-0.470813000
6	-4.793635000	0.457633000	-0.425131000
7	1.450656000	-1.518081000	-0.324603000
6	3.369097000	-2.758230000	0.009218000
7	-1.443263000	-1.292710000	-0.413277000
6	-3.563552000	-2.195157000	-0.554120000
6	-5.474307000	1.112442000	-1.465068000
6	-5.539927000	-0.054161000	0.649937000
6	1.131992000	-2.854066000	-0.288977000
6	2.329717000	-3.637528000	-0.078767000
1	4.415314000	-2.980631000	0.173322000
6	-1.357292000	-2.658120000	-0.434870000
6	-2.684175000	-3.235986000	-0.533366000
1	-4.642258000	-2.239390000	-0.627698000
6	-6.864986000	1.247084000	-1.435195000
6	-6.929967000	0.082734000	0.683941000
6	-0.163604000	-3.402956000	-0.373771000
1	2.364122000	-4.715652000	0.006615000
1	-2.906520000	-4.293812000	-0.584303000
6	-7.598005000	0.732856000	-0.359852000
1	-7.376171000	1.751083000	-2.253027000
1	-7.490732000	-0.313762000	1.528094000
6	-0.278718000	-4.890508000	-0.356118000
6	0.244971000	-5.662410000	-1.406202000
6	-0.906689000	-5.547695000	0.715011000
6	0.140082000	-7.055953000	-1.389221000
6	-1.009943000	-6.941156000	0.735667000
6	-0.487774000	-7.700359000	-0.317531000
1	0.545910000	-7.637924000	-2.214333000
1	-1.494170000	-7.434043000	1.576373000
1	8.924758000	-0.700151000	0.382931000
1	-8.680548000	0.838973000	-0.334837000
1	-0.568658000	-8.785273000	-0.302771000
1	0.771158000	8.864383000	0.155387000
26	0.165089000	0.044438000	-1.026517000
1	-4.903684000	1.511400000	-2.300592000
1	-5.018937000	-0.552323000	1.463597000
1	4.990655000	-1.043918000	2.111301000
1	5.433856000	0.266948000	-1.954494000
1	-1.306706000	-4.956526000	1.535594000
1	0.731382000	-5.160203000	-2.239355000
1	-0.390043000	5.318976000	-2.003267000
1	1.451798000	4.965186000	1.860565000
8	0.862319000	0.535240000	-2.801131000
8	-0.223763000	-0.386312000	-2.907551000
6	0.246216000	-1.042167000	2.716083000
6	-1.137346000	0.667341000	2.598920000
6	-1.707391000	-0.356057000	3.322306000
7	-0.825667000	-1.423679000	3.395062000
1	1.130097000	-1.638063000	2.527995000
1	-1.511950000	1.631777000	2.288280000
6	-3.070268000	-0.406810000	3.940463000
1	-3.621300000	0.518228000	3.733418000
1	-3.651516000	-1.249709000	3.539061000
1	-3.015800000	-0.539453000	5.030875000
7	0.111948000	0.219338000	2.231162000
1	0.741506000	0.679464000	1.571056000

[(4-MeIm)(TPP)Fe^{III}(O_2^{2-})]$^-$ (uB97D-def2-TZVP) Charge: -1, Multiplicity: 4

7	-0.950518000	-1.771837000	-0.324895000
7	1.761349000	-0.872075000	-0.395425000
6	-2.303165000	-2.004900000	-0.381893000
6	-2.568182000	-3.414141000	-0.277359000
6	-1.353067000	-4.036371000	-0.161218000
6	-0.354275000	-3.003338000	-0.196962000
6	1.034088000	-3.236001000	-0.170994000
6	1.998262000	-2.236739000	-0.295527000
6	3.421056000	-2.492655000	-0.300970000
6	4.043172000	-1.290136000	-0.422556000
6	3.009897000	-0.280607000	-0.463465000
6	-3.298830000	-1.011643000	-0.473024000
6	1.490917000	-4.648831000	-0.020805000
6	1.280375000	-5.339457000	1.183976000
6	1.700399000	-6.664324000	1.333145000
6	2.338291000	-7.322434000	0.275465000
6	2.551294000	-6.645370000	-0.930417000
6	2.129396000	-5.320414000	-1.075879000
6	-4.716242000	-1.465155000	-0.574423000
6	-5.633497000	-1.213312000	0.459309000
6	-6.958968000	-1.647031000	0.363765000
6	-7.389957000	-2.344250000	-0.770316000
6	-6.484948000	-2.603918000	-1.805848000
6	-5.160434000	-2.168958000	-1.706359000
1	-3.551510000	-3.866041000	-0.287694000
1	-1.151325000	-5.095863000	-0.071016000
1	3.873561000	-3.471483000	-0.213141000
1	5.105896000	-1.087788000	-0.447162000
1	1.533044000	-7.181459000	2.276100000
1	3.041996000	-7.150179000	-1.760425000
1	-7.653646000	-1.444774000	1.176858000
1	-6.811353000	-3.142201000	-2.693667000
6	3.273156000	1.089256000	-0.423866000
6	-3.037575000	0.357493000	-0.439884000
6	2.279242000	2.070517000	-0.272705000
6	4.696757000	1.529345000	-0.486544000
7	-1.788737000	0.951144000	-0.311876000
6	-4.064288000	1.374370000	-0.497651000
7	0.919420000	1.832080000	-0.237674000
6	2.538165000	3.476454000	-0.146045000
6	5.449331000	1.349207000	-1.658614000
6	5.321062000	2.115963000	0.626828000
6	-2.028120000	2.311542000	-0.232306000
6	-3.444341000	2.575977000	-0.357349000
1	-5.120403000	1.179709000	-0.629209000

6	0.321815000	3.069399000	-0.098855000
6	1.322979000	4.094670000	-0.015739000
1	3.519579000	3.931834000	-0.153302000
6	6.788793000	1.745177000	-1.718437000
6	6.659674000	2.514054000	0.570557000
6	-1.063153000	3.310347000	-0.088441000
1	-3.890973000	3.561709000	-0.355805000
1	1.123424000	5.150744000	0.108832000
6	7.399188000	2.329957000	-0.603367000
1	7.354473000	1.599996000	-2.636850000
1	7.127183000	2.962236000	1.445328000
6	-1.531700000	4.719715000	0.054523000
6	-1.277498000	5.672649000	-0.945920000
6	-2.248480000	5.120938000	1.194110000
6	-1.725127000	6.989887000	-0.811212000
6	-2.697818000	6.437446000	1.332666000
6	-2.437031000	7.377656000	0.329711000
1	-1.522840000	7.712242000	-1.599775000
1	-3.248413000	6.729567000	2.224930000
1	-8.421310000	-2.682641000	-0.846328000
1	8.441636000	2.638634000	-0.648197000
1	-2.786157000	8.402811000	0.435456000
1	2.665762000	-8.353775000	0.389834000
26	-0.010405000	0.042844000	-0.349333000
1	4.973878000	0.894548000	-2.525000000
1	4.748234000	2.253609000	1.540981000
1	-5.297624000	-0.673596000	1.341956000
1	-4.456828000	-2.370246000	-2.511028000
1	-2.451085000	4.389222000	1.973222000
1	-0.727799000	5.370339000	-1.834318000
1	2.291724000	-4.794730000	-2.014180000
1	0.784938000	-4.826921000	2.005786000
8	-0.252985000	-0.300583000	-2.602572000
8	0.192438000	0.743829000	-3.252246000
6	-1.326718000	-0.342413000	2.594233000
6	0.147501000	-0.469969000	4.238571000
6	0.794549000	-0.246639000	3.042150000
7	-0.143934000	-0.169195000	2.031507000
1	-2.275232000	-0.346646000	2.074617000
1	0.512677000	-0.587944000	5.249364000
6	2.259909000	-0.108020000	2.781835000
1	2.633332000	-0.944269000	2.177442000
1	2.468106000	0.806317000	2.213732000
1	2.814959000	-0.078661000	3.726958000
7	-1.199616000	-0.529448000	3.933171000
1	-1.953872000	-0.678862000	4.587876000

[(4-MeIm)(TPP)Fe^{III}(O_2^{2-})]$^-$ (uB97D-def2-TZVP) Charge: -1, Multiplicity: 2

7	-1.125484000	-1.642941000	-0.359623000
7	1.646913000	-1.112506000	-0.332188000
6	-2.488943000	-1.719007000	-0.537031000
6	-2.926823000	-3.093117000	-0.447603000
6	-1.819454000	-3.843858000	-0.184759000
6	-0.698495000	-2.933410000	-0.136686000
6	0.633362000	-3.334591000	0.033928000
6	1.727036000	-2.470582000	-0.109278000
6	3.109050000	-2.891178000	-0.097315000
6	3.859296000	-1.787116000	-0.375302000
6	2.942760000	-0.679241000	-0.503866000
6	-3.357220000	-0.623934000	-0.658602000
6	0.891676000	-4.773876000	0.328433000
6	0.479370000	-5.328997000	1.551485000
6	0.705199000	-6.678070000	1.839534000
6	1.347782000	-7.497768000	0.904974000
6	1.760054000	-6.957439000	-0.318310000
6	1.532248000	-5.607859000	-0.602725000
6	-4.802078000	-0.911371000	-0.891053000
6	-5.769913000	-0.621686000	0.085195000
6	-7.119979000	-0.907596000	-0.136394000
6	-7.526127000	-1.492238000	-1.341288000
6	-6.571151000	-1.789665000	-2.319888000
6	-5.221845000	-1.502490000	-2.094438000
1	-3.951227000	-3.426130000	-0.554142000
1	-1.754374000	-4.915716000	-0.048787000
1	3.450964000	-3.901206000	0.086216000
1	4.936585000	-1.712604000	-0.449135000
1	0.382062000	-7.088298000	2.794491000
1	2.254312000	-7.588468000	-1.054573000
1	-7.854101000	-0.679109000	0.633995000
1	-6.876958000	-2.242781000	-3.260999000
6	3.349784000	0.657485000	-0.605424000
6	-2.953016000	0.708251000	-0.497568000
6	2.487262000	1.744517000	-0.416649000
6	4.802087000	0.917597000	-0.821228000
7	-1.657760000	1.130762000	-0.278034000
6	-3.854371000	1.837365000	-0.472296000
7	1.122947000	1.660462000	-0.227292000
6	2.918658000	3.119296000	-0.318837000
6	5.415389000	0.546852000	-2.029407000
6	5.594749000	1.504025000	0.179550000
6	-1.733027000	2.490250000	-0.073482000
6	-3.102567000	2.936829000	-0.184512000
1	-4.920821000	1.785905000	-0.647640000
6	0.691066000	2.952051000	-0.014033000
6	1.813234000	3.861762000	-0.029467000
1	3.937670000	3.462124000	-0.439512000
6	6.780790000	0.763706000	-2.236569000
6	6.960197000	1.722221000	-0.023840000
6	-0.644951000	3.351518000	0.114352000
1	-3.430007000	3.963665000	-0.084542000
1	1.751497000	4.930017000	0.130383000
6	7.558614000	1.353657000	-1.234120000
1	7.236495000	0.474048000	-3.181542000
1	7.558382000	2.173800000	0.765409000
6	-0.941917000	4.788670000	0.384478000
6	-0.660051000	5.782893000	-0.566800000
6	-1.537139000	5.172073000	1.597578000
6	-0.956787000	7.124506000	-0.310173000
6	-1.835412000	6.512861000	1.858071000
6	-1.544805000	7.494888000	0.904588000
1	-0.734536000	7.879957000	-1.061501000
1	-2.292593000	6.790739000	2.805924000
1	-8.576815000	-1.715431000	-1.515155000
1	8.621690000	1.522504000	-1.393387000
1	-1.776693000	8.538953000	1.105077000
1	1.524109000	-8.548277000	1.127089000
26	-0.004426000	0.020393000	-0.324629000
1	4.810233000	0.086572000	-2.807430000
1	5.131605000	1.782805000	1.123086000
1	-5.453749000	-0.172008000	1.023672000
1	-4.478984000	-1.733779000	-2.854670000
1	-1.764673000	4.407441000	2.337398000
1	-0.209862000	5.493845000	-1.513603000
1	1.847521000	-5.189764000	-1.555889000
1	-0.020794000	-4.691112000	2.277146000
8	0.036347000	0.007075000	-2.207262000
8	-0.178035000	1.108731000	-2.916800000
6	-1.324276000	-0.265862000	2.380020000
6	0.142026000	-0.287023000	4.032297000
6	0.800565000	-0.135546000	2.832422000
7	-0.134892000	-0.121527000	1.809930000
1	-2.268555000	-0.302082000	1.858227000
1	0.505993000	-0.341195000	5.048402000
6	2.272693000	-0.019586000	2.616249000
1	2.667531000	-0.902968000	2.100669000
1	2.510004000	0.847938000	1.992897000
1	2.781922000	0.081279000	3.582133000
7	-1.200657000	-0.369623000	3.724125000
1	-1.960327000	-0.480732000	4.379450000

[(ArO$^-$)(TPP)Fe^{III}(O_2^{2-})]$^{2-}$ (uB97D-def2-TZVP) Charge: -2, Multiplicity: 6

7	0.586466000	-2.070519000	-0.538124000
7	2.607390000	0.061348000	-0.157547000
6	-0.509045000	-2.885280000	-0.618870000
6	-0.108686000	-4.246817000	-0.327971000
6	1.241733000	-4.226027000	-0.102749000
6	1.672721000	-2.849638000	-0.249481000
6	3.005519000	-2.385937000	-0.089382000
6	3.427986000	-1.036148000	-0.082165000
6	4.806159000	-0.587500000	0.012373000
6	4.782695000	0.778627000	0.024992000
6	3.391093000	1.182761000	-0.068404000
6	-1.828989000	-2.462474000	-0.918643000
6	4.057473000	-3.427303000	0.095694000
6	4.832470000	-3.476079000	1.268003000
6	5.814053000	-4.455925000	1.441008000
6	6.040638000	-5.409404000	0.441724000
6	5.276332000	-5.373371000	-0.730294000
6	4.295137000	-4.392695000	-0.899001000
6	-2.868138000	-3.525462000	-1.033157000
6	-3.981825000	-3.532361000	-0.174833000
6	-4.955069000	-4.530274000	-0.270171000
6	-4.835468000	-5.541483000	-1.230303000
6	-3.733329000	-5.544642000	-2.093464000
6	-2.759941000	-4.546678000	-1.993563000
1	-0.770058000	-5.103140000	-0.289152000
1	1.881236000	-5.062130000	0.151019000
1	5.675177000	-1.231769000	0.056733000
1	5.629689000	1.450985000	0.079195000
1	6.398215000	-4.478526000	2.359238000
1	5.447501000	-6.106613000	-1.516395000
1	-5.803603000	-4.521567000	0.411700000
1	-3.633683000	-6.322417000	-2.848494000
6	2.922483000	2.518094000	-0.075020000
6	-2.261627000	-1.128299000	-1.088501000
6	1.579073000	2.934102000	-0.265992000
6	3.934677000	3.592070000	0.139918000
7	-1.497728000	-0.004782000	-0.904612000
6	-3.601277000	-0.730239000	-1.481203000
7	0.521905000	2.116917000	-0.578923000
6	1.099519000	4.293479000	-0.133416000
6	4.156175000	4.580422000	-0.836178000
6	4.692158000	3.647046000	1.323738000
6	-2.299256000	1.086388000	-1.114305000
6	-3.625167000	0.634182000	-1.496496000
1	-4.412263000	-1.405774000	-1.721270000
6	-0.601167000	2.898519000	-0.675657000
6	-0.246296000	4.271316000	-0.384885000
1	1.705497000	5.149840000	0.134554000
6	5.103342000	5.588614000	-0.638294000
6	5.639981000	4.654061000	1.525763000
6	-1.908141000	2.437681000	-0.974953000
1	-4.458630000	1.275189000	-1.753521000
1	-0.935307000	5.105874000	-0.357233000
6	5.850139000	5.630055000	0.544825000
1	5.262269000	6.339005000	-1.410677000
1	6.210513000	4.680101000	2.452434000
6	-2.971221000	3.470786000	-1.126446000
6	-2.862153000	4.487162000	-2.093234000
6	-4.110768000	3.459523000	-0.301127000
6	-3.855360000	5.460544000	-2.230184000
6	-5.104819000	4.431789000	-0.434726000
6	-4.982160000	5.437992000	-1.399900000
1	-3.751891000	6.233958000	-2.989222000
1	-5.971995000	4.408333000	0.222920000
1	-5.593258000	-6.318939000	-1.306046000
1	6.587841000	6.414717000	0.700827000
1	-5.755732000	6.196368000	-1.504118000
1	6.804495000	-6.172931000	0.575211000
26	0.569547000	0.024018000	-0.603097000
8	0.878441000	-0.842008000	-3.656250000
8	0.910916000	-0.053030000	-2.589290000
1	3.578604000	4.547207000	-1.757055000
1	4.526093000	2.892007000	2.088601000
1	-4.069045000	-2.754832000	0.578556000
1	-1.905248000	-4.547161000	-2.666048000
1	-4.201796000	2.689240000	0.459573000
1	-1.988758000	4.504391000	-2.740991000
1	3.703284000	-4.362917000	-1.810953000
1	4.653437000	-2.738618000	2.046996000
6	-1.663119000	1.186589000	2.333241000
6	-2.977494000	1.182813000	2.795692000
6	-3.660509000	-0.014717000	3.067893000
6	-2.976550000	-1.225639000	2.868606000
6	-1.660141000	-1.256729000	2.409500000
6	-0.968614000	-0.042132000	2.105183000
1	-1.153270000	2.105720000	2.067531000
1	-4.680654000	-0.004164000	3.441784000

1	-1.148193000	-2.190830000	2.206639000
8	-3.713161000	2.338700000	3.011193000
8	-3.713453000	-2.365928000	3.154679000
6	-3.013963000	-3.612118000	3.143356000
1	-3.744309000	-4.371307000	3.441376000
1	-2.629617000	-3.845930000	2.141077000
1	-2.173787000	-3.596386000	3.854063000
6	-3.009632000	3.580577000	2.926495000
1	-2.612315000	3.747681000	1.916215000
1	-3.742282000	4.358316000	3.164725000
1	-2.178013000	3.608839000	3.647107000
8	0.240458000	-0.052228000	1.629403000

$[(ArO^{-})(TPP)Fe^{III}(O_2^{2-})]^{2-}$ (uB97D-def2-TZVP) Charge: -2, Multiplicity: 4

7	0.969071000	-1.891169000	-0.519462000
7	2.480483000	0.517505000	-0.153232000
6	0.057947000	-2.921379000	-0.451524000
6	0.733829000	-4.145403000	-0.161529000
6	2.083918000	-3.854470000	-0.105446000
6	2.213680000	-2.453274000	-0.332810000
6	3.448545000	-1.749681000	-0.316893000
6	3.544857000	-0.364188000	-0.237829000
6	4.788544000	0.373237000	-0.162808000
6	4.466347000	1.680413000	0.030683000
6	3.018427000	1.769746000	0.039899000
6	-1.337548000	-2.798627000	-0.686343000
6	4.692647000	-2.565004000	-0.329574000
6	5.624901000	-2.506156000	0.722733000
6	6.788663000	-3.281167000	0.699948000
6	7.041981000	-4.139985000	-0.374862000
6	6.118501000	-4.217149000	-1.425712000
6	4.957476000	-3.441372000	-1.398993000
6	-2.173253000	-4.025644000	-0.647134000
6	-3.269610000	-4.111741000	0.232934000
6	-4.075313000	-5.252528000	0.275164000
6	-3.801676000	-6.340123000	-0.561561000
6	-2.713755000	-6.271408000	-1.442023000
6	-1.911320000	-5.128919000	-1.482191000
1	0.255383000	-5.105909000	-0.022913000
1	2.905355000	-4.532727000	0.087347000
1	5.775576000	-0.063271000	-0.243141000
1	5.137838000	2.523322000	0.132820000
1	7.493489000	-3.220293000	1.527485000
1	6.306356000	-4.879123000	-2.269326000
1	-4.912153000	-5.294752000	0.970464000
1	-2.496025000	-7.106876000	-2.105423000
6	2.312297000	2.968582000	0.165783000
6	-1.969227000	-1.586239000	-0.964751000
6	0.916235000	3.087212000	-0.074910000
6	3.074049000	4.195055000	0.520325000
7	-1.408462000	-0.332679000	-0.896032000
6	-3.340390000	-1.477201000	-1.419887000
7	0.095035000	2.072160000	-0.520860000
6	0.170235000	4.299711000	0.032543000
6	3.094973000	5.319634000	-0.327373000
6	3.814011000	4.261367000	1.716896000
6	-2.398534000	0.566722000	-1.243176000
6	-3.596690000	-0.156165000	-1.611854000
1	-4.003554000	-2.314916000	-1.591480000
6	-1.141057000	2.643889000	-0.756634000
6	-1.109456000	4.025618000	-0.411556000
1	0.561869000	5.245466000	0.383358000
6	3.827383000	6.461752000	0.003755000
6	4.550394000	5.401571000	2.051506000
6	-2.301683000	1.953817000	-1.191181000
1	-4.512405000	0.297790000	-1.966518000
1	-1.952417000	4.701738000	-0.471466000
6	4.560115000	6.509599000	1.197076000
1	3.834747000	7.313272000	-0.674717000
1	5.111300000	5.426963000	2.984352000
6	-3.495801000	2.774976000	-1.525535000
6	-3.436703000	3.741932000	-2.546608000
6	-4.705486000	2.632052000	-0.820570000
6	-4.547966000	4.526911000	-2.862660000
6	-5.819983000	3.415366000	-1.133858000
6	-5.747755000	4.366322000	-2.157459000
1	-4.480151000	5.261255000	-3.663526000
1	-6.742900000	3.288669000	-0.570413000
1	-4.426732000	-7.230509000	-0.529330000
1	5.131083000	7.399102000	1.456230000
1	-6.614136000	4.978121000	-2.401421000
1	7.946510000	-4.744873000	-0.393262000
26	0.531115000	0.086572000	-0.540594000
8	0.668920000	-0.768848000	-3.287014000
8	0.846485000	0.161287000	-2.372574000
1	2.533257000	5.283992000	-1.257731000
1	3.804329000	3.403173000	2.385186000
1	-3.475322000	-3.273804000	0.893173000
1	-1.072431000	-5.076417000	-2.171980000
1	-4.759077000	1.906579000	-0.013431000
1	-2.505498000	3.868451000	-3.094214000
1	4.240636000	-3.501973000	-2.214777000
1	5.424895000	-1.847158000	1.564218000
6	-1.814173000	0.931543000	2.098471000
6	-3.079899000	0.773794000	2.665194000
6	-3.515468000	-0.472686000	3.143041000
6	-2.648117000	-1.571420000	3.045539000
6	-1.378015000	-1.443457000	2.479050000
6	-0.949526000	-0.185300000	1.982555000
1	-1.483245000	1.874548000	1.682797000
1	-4.500696000	-0.582422000	3.588106000
1	-0.718250000	-2.292478000	2.344772000
8	-3.992323000	1.802861000	2.788476000
8	-3.151894000	-2.763032000	3.531173000
6	-2.260133000	-3.882022000	3.568375000
1	-2.826956000	-4.701943000	4.020117000
1	-1.939820000	-4.167521000	2.557187000
1	-1.372860000	-3.654937000	4.178166000
6	-3.536810000	3.118339000	2.448435000
1	-3.233778000	3.177434000	1.395626000
1	-4.385835000	3.785012000	2.628471000
1	-2.685256000	3.410561000	3.081358000
8	0.244730000	-0.070249000	1.433492000

$[(ArO^{-})(TPP)Fe^{III}(O_2^{2-})]^{2-}$ (uB97D-def2-TZVP) Charge: -2, Multiplicity: 2

7	-0.184037000	2.024492000	-0.496042000
7	-2.503311000	0.387603000	-0.220743000
6	1.026463000	2.658318000	-0.669323000
6	0.904983000	4.063988000	-0.363777000
6	-0.398048000	4.282998000	-0.028718000
6	-1.078786000	3.014996000	-0.145217000
6	-2.458041000	2.846293000	0.038310000
6	-3.114755000	1.612093000	-0.055919000
6	-4.549043000	1.451519000	-0.003616000
6	-4.801460000	0.116354000	-0.115158000
6	-3.519175000	-0.543416000	-0.218703000
6	2.226317000	2.042473000	-1.044995000
6	-3.283359000	4.052165000	0.336475000
6	-3.973613000	4.163643000	1.555804000
6	-4.751922000	5.289071000	1.841138000
6	-4.856061000	6.326836000	0.907936000
6	-4.175527000	6.227910000	-0.311067000
6	-3.397579000	5.101073000	-0.591940000
6	3.414937000	2.908043000	-1.281550000
6	4.568859000	2.789287000	-0.487171000
6	5.677880000	3.610677000	-0.705727000
6	5.655806000	4.568000000	-1.726572000
6	4.513350000	4.696822000	-2.524886000
6	3.405202000	3.874722000	-2.302360000
1	1.717882000	4.777839000	-0.389804000
1	-0.863288000	5.213731000	0.268965000
1	-5.261989000	2.260174000	0.094248000
1	-5.761548000	-0.382963000	-0.122117000
1	-5.273662000	5.357577000	2.794029000
1	-4.254578000	7.026580000	-1.046442000
1	6.557623000	3.507731000	-0.072813000
1	4.486454000	5.435155000	-3.324382000
6	-3.349506000	-1.934334000	-0.261422000
6	2.371329000	0.658252000	-1.174768000
6	-2.099015000	-2.563973000	-0.353256000
6	-4.558284000	-2.801504000	-0.166279000
7	1.396585000	-0.280934000	-0.913767000
6	3.605920000	0.008984000	-1.548505000
7	-0.891471000	-1.935117000	-0.555167000
6	-1.901999000	-3.987414000	-0.197432000
6	-4.897632000	-3.673688000	-1.215508000
6	-5.380583000	-2.782220000	0.973860000
6	2.014100000	-1.505798000	-1.046366000
6	3.387429000	-1.331745000	-1.456949000
1	4.515915000	0.518852000	-1.835486000
6	0.056500000	-2.936195000	-0.573828000
6	-0.563373000	-4.215298000	-0.320511000
1	-2.687037000	-4.705730000	0.000911000
6	-6.023185000	-4.497987000	-1.131129000
6	-6.507080000	-3.604832000	1.062593000
6	1.421561000	-2.755887000	-0.829214000
1	4.082034000	-2.136267000	-1.660026000
1	-0.038410000	-5.158658000	-0.246042000
6	-6.833910000	-4.466700000	0.009328000
1	-6.269684000	-5.161823000	-1.957884000
1	-7.126407000	-3.577545000	1.957394000
6	2.304649000	-3.955161000	-0.859505000
6	2.106111000	-4.990562000	-1.789211000
6	3.370596000	-4.071353000	0.050300000
6	2.943268000	-6.109833000	-1.807581000
6	4.207753000	-5.189805000	0.036234000
6	3.997969000	-6.214885000	-0.893316000
1	2.775543000	-6.897521000	-2.540000000
1	5.021028000	-5.262678000	0.756170000
1	6.519287000	5.208035000	-1.897552000
1	-7.710405000	-5.108146000	0.077182000
1	4.650013000	-7.086156000	-0.906443000
1	-5.461953000	7.203592000	1.128152000
26	-0.542728000	0.058273000	-0.587324000
8	-0.196436000	0.733183000	-3.311279000
8	-0.951525000	0.086238000	-2.417152000
1	-4.267751000	-3.698109000	-2.101928000
1	-5.124460000	-2.116631000	1.794880000
1	4.581599000	2.057769000	0.316044000
1	2.517355000	3.973284000	-2.922863000
1	3.530315000	-3.278515000	0.775683000
1	1.289459000	-4.907680000	-2.502563000
1	-2.871080000	5.022816000	-1.540321000
1	-3.891598000	3.357329000	2.281160000
6	1.429825000	-1.443148000	2.452679000
6	2.725903000	-1.533231000	2.960857000
6	3.541174000	-0.398580000	3.099818000
6	3.013644000	0.847759000	2.722202000
6	1.720316000	0.970411000	2.217182000
6	0.898609000	-0.182189000	2.047267000
1	0.817116000	-2.322663000	2.289649000
1	4.545569000	-0.479743000	3.506447000
1	1.326974000	1.919923000	1.876143000
8	3.313827000	-2.728244000	3.348497000
8	3.874491000	1.921736000	2.883441000
6	3.327516000	3.227292000	2.674080000
1	4.141559000	3.930574000	2.876606000
1	2.977426000	3.354659000	1.641513000
1	2.487247000	3.412797000	3.360525000
6	2.467786000	-3.879090000	3.411909000
1	2.082604000	-4.148174000	2.418712000
1	3.093435000	-4.692152000	3.793925000
1	1.618778000	-3.704074000	4.089989000
8	-0.301321000	-0.093848000	1.541472000

[(ArS^{-})(TPP)Fe^{III}(O$_2^{2-}$)]$^{2-}$ (uB97D-def2-TZVP) Charge: -2, Multiplicity: 6

7	-0.949476000	1.985508000	-0.356687000	1	2.134711000	7.284915000	-2.334215000	1	5.716982000	-4.567744000	-2.767512000
7	-2.328411000	-0.593033000	-0.227286000	6	-1.996198000	-3.047391000	-0.292614000	1	6.907751000	-2.646188000	0.902590000
6	-0.112696000	3.073471000	-0.332568000	6	2.064852000	1.889365000	-0.738203000	1	3.827271000	7.810134000	-0.580874000
6	-0.875937000	4.259540000	-0.002852000	6	-0.590244000	-3.072153000	-0.410324000	1	-4.498607000	-7.819538000	0.066325000
6	-2.173897000	3.867913000	0.156229000	6	-2.691204000	-4.363755000	-0.192582000	1	7.414894000	-4.203045000	-0.979166000
6	-2.215728000	2.438701000	-0.076106000	7	1.605963000	0.597830000	-0.678667000	1	-8.056898000	4.215104000	0.812285000
6	-3.377706000	1.642225000	0.001154000	6	3.489970000	1.882539000	-0.987427000	26	-0.405394000	0.012626000	-0.829209000
6	-3.418001000	0.233215000	-0.097108000	7	0.220060000	-1.979280000	-0.601356000	8	-0.355065000	0.763528000	-3.840695000
6	-4.624914000	-0.565754000	-0.062199000	6	0.226235000	-4.262911000	-0.295994000	8	-0.627138000	0.104212000	-2.711391000
6	-4.240239000	-1.873566000	-0.143966000	6	-2.631333000	-5.286974000	-1.250286000	1	-2.075132000	-5.025022000	-2.147410000
6	-2.795473000	-1.884986000	-0.229767000	6	-3.412315000	-4.712705000	0.962022000	1	-3.455252000	-4.008218000	1.789256000
6	1.280451000	3.048557000	-0.557771000	6	2.693523000	-0.225905000	-0.827980000	1	3.162462000	3.935587000	1.186462000
6	-4.672230000	2.349878000	0.225426000	6	3.878901000	0.575659000	-1.040083000	1	0.966443000	5.091313000	-2.316486000
6	-5.423256000	2.126259000	1.391941000	1	4.109883000	2.762349000	-1.100539000	1	4.722336000	-1.467428000	0.987282000
6	-6.633080000	2.792921000	1.603426000	6	1.516114000	-2.433549000	-0.621549000	1	3.533557000	-3.385984000	-2.667772000
6	-7.114697000	3.695875000	0.648858000	6	1.526256000	-3.868616000	-0.424062000	1	-4.591304000	3.438703000	-1.630997000
6	-6.375741000	3.927309000	-0.516727000	1	-0.148452000	-5.261737000	-0.113329000	1	-5.046136000	1.428227000	2.135667000
6	-5.165141000	3.260662000	-0.724461000	6	-3.278617000	-6.522259000	-1.160039000	6	2.616395000	-1.165511000	3.732474000
6	1.987995000	4.362108000	-0.566821000	6	-4.058326000	-5.948221000	1.056115000	6	3.996602000	-0.966614000	3.656929000
6	2.945046000	4.669588000	0.414708000	6	2.670507000	-1.635346000	-0.772196000	6	4.522923000	0.183419000	3.052649000
6	3.603197000	5.902228000	0.411612000	1	4.875654000	0.187407000	-1.202990000	6	3.630961000	1.122746000	2.516875000
6	3.315059000	6.850092000	-0.576842000	1	2.414204000	-4.484460000	-0.365655000	6	2.252046000	0.929290000	2.593457000
6	2.362952000	6.555632000	-1.559273000	6	-3.995189000	-6.857552000	-0.005755000	6	1.691053000	-0.219956000	3.212778000
6	1.704688000	5.322716000	-1.552029000	1	-3.226050000	-7.221344000	-1.992501000	1	2.228670000	-2.067821000	4.203793000
1	-0.465918000	5.254691000	0.111711000	1	-4.606440000	-6.202938000	1.961154000	1	5.598570000	0.334940000	2.985377000
1	-3.022769000	4.482760000	0.425883000	6	3.982497000	-2.342360000	-0.837171000	1	1.583657000	1.664030000	2.150441000
1	-5.631698000	-0.176284000	0.014011000	6	4.275728000	-3.226515000	-1.888765000	16	-0.043891000	-0.457652000	3.336620000
1	-4.874902000	-2.750131000	-0.148827000	6	4.947733000	-2.141459000	0.164176000	1	4.015675000	2.008448000	2.014372000
1	-7.197005000	2.610941000	2.516287000	6	5.504260000	-3.891112000	-1.941950000	1	4.667799000	-1.721071000	4.067978000
1	-6.743584000	4.624607000	-1.267041000	6	6.174905000	-2.807988000	0.114008000				
1	4.336967000	6.124090000	1.184149000	6	6.458952000	-3.684452000	-0.939626000				

[(ArS^{-})(TPP)Fe^{III}(O$_2^{2-}$)]$^{2-}$ (uB97D-def2-TZVP) Charge: -2, Multiplicity: 4

7	0.809026000	-1.947019000	-0.316911000	6	2.200765000	2.925257000	-0.306703000	1	-4.262021000	-7.506264000	-0.925248000
7	2.319373000	0.454820000	-0.232452000	6	-2.125501000	-1.696405000	-0.825042000	1	5.028180000	7.521091000	-0.114267000
6	-0.085483000	-2.998686000	-0.339332000	6	0.804902000	3.019671000	-0.356129000	1	-7.131526000	4.666709000	-0.857229000
6	0.582847000	-4.229556000	-0.000381000	6	2.986031000	4.191810000	-0.253178000	1	7.757128000	-4.676317000	0.901678000
6	1.896109000	-3.926052000	0.202861000	7	-1.571602000	-0.439785000	-0.691786000	26	0.389886000	0.005494000	-0.599252000
6	2.036266000	-2.508176000	-0.019038000	6	-3.530824000	-1.593150000	-1.124018000	8	0.295748000	-0.831060000	-3.639828000
6	3.254775000	-1.821852000	0.041309000	7	-0.073353000	1.962085000	-0.505554000	8	0.617201000	-0.089530000	-2.597365000
6	3.369936000	-0.433686000	-0.106797000	6	0.077930000	4.257794000	-0.233271000	1	2.350833000	4.861700000	-2.198643000
6	4.626226000	0.272954000	-0.133576000	6	2.953646000	5.099391000	-1.325134000	1	3.791769000	3.814806000	1.707766000
6	4.332192000	1.599751000	-0.242363000	6	3.767122000	4.508698000	0.870822000	1	-3.443266000	-3.740030000	1.005217000
6	2.896093000	1.710613000	-0.275211000	6	-2.620617000	0.444896000	-0.832849000	1	-1.188158000	-4.899539000	-2.457885000
6	-1.450112000	-2.907210000	-0.638753000	6	-3.839815000	-0.266771000	-1.121804000	1	-4.600527000	1.735572000	1.041242000
6	4.498018000	-2.610397000	0.277994000	1	-4.190800000	-2.432768000	-1.297370000	1	-3.293192000	3.684416000	-2.556545000
6	5.263347000	-2.411949000	1.439516000	6	-1.335407000	2.526031000	-0.517617000	1	4.345708000	-3.726919000	-1.557072000
6	6.428437000	-3.150290000	1.664368000	6	-1.246846000	3.952212000	-0.325770000	1	4.933314000	-1.675096000	2.168159000
6	6.849902000	-4.101098000	0.727974000	1	0.530561000	5.228374000	-0.078534000	6	-2.587784000	1.105667000	3.776645000
6	6.096383000	-4.307423000	-0.433080000	6	3.684682000	6.289645000	-1.277844000	6	-3.979896000	1.030477000	3.693922000
6	4.930867000	-3.568450000	-0.654134000	6	4.497211000	5.699249000	0.922245000	6	-4.601271000	-0.027323000	3.015935000
6	-2.231909000	-4.174205000	-0.720348000	6	-2.538531000	1.835677000	-0.705138000	6	-3.791882000	-1.001426000	2.414941000
6	-3.239813000	-4.458749000	0.215516000	1	-4.801906000	0.197206000	-1.293054000	6	-2.401576000	-0.932035000	2.499115000
6	-3.966543000	-5.650340000	0.144109000	1	-2.093797000	4.622288000	-0.262733000	6	-1.746182000	0.121557000	3.190751000
6	-3.696549000	-6.578310000	-0.868089000	6	4.459644000	6.594080000	-0.153080000	1	-2.125271000	1.937966000	4.305820000
6	-2.693743000	-6.305870000	-1.805475000	1	3.651531000	6.977594000	-2.120546000	1	-5.685813000	-0.081528000	2.942805000
6	-1.967091000	-5.114236000	-1.729703000	1	5.091458000	5.930347000	1.804245000	1	-1.797261000	-1.689836000	2.006417000
1	0.099197000	-5.194042000	0.082880000	6	-3.804996000	2.620761000	-0.754437000	16	0.002827000	0.202483000	3.321235000
1	2.700617000	-4.592296000	0.484599000	6	-4.045876000	3.545609000	-1.783661000	1	-4.250110000	-1.815787000	1.856416000
1	5.601051000	-0.193089000	-0.078826000	6	-4.783715000	2.445716000	0.238184000	1	-4.585095000	1.809900000	4.1574900
1	5.019831000	2.433438000	-0.295025000	6	-5.236380000	4.277290000	-1.822498000				
1	7.004455000	-2.986350000	2.573131000	6	-5.973261000	3.178443000	0.202282000				
1	6.418233000	-5.041316000	-1.169554000	6	-6.204962000	4.096591000	-0.828442000				
1	-4.739809000	-5.856068000	0.881842000	1	-5.409189000	4.985507000	-2.630763000				
1	-2.478860000	-7.020098000	-2.598092000	1	-6.717826000	3.034703000	0.983393000				

[(ArS^{-})(TPP)Fe^{III}(O$_2^{2-}$)]$^{2-}$ (uB97D-def2-TZVP) Charge: -2, Multiplicity: 2

7	1.429902000	-1.646761000	-0.255747000	6	2.805523000	-1.729939000	-0.211958000	6	2.065067000	2.503761000	-0.068075000
7	1.993359000	1.134083000	-0.193450000	6	3.698532000	-0.651101000	-0.269885000	6	-0.372372000	-3.330950000	-0.140124000
6	0.970370000	-2.936850000	-0.100055000	6	3.299447000	0.691827000	-0.246245000	6	5.156981000	-0.960544000	-0.299929000
6	2.079764000	-3.844420000	0.085322000	6	4.207604000	1.813676000	-0.208652000	6	6.002469000	-0.597260000	0.762276000
6	3.217081000	-3.099289000	-0.005230000	6	3.443436000	2.935873000	-0.077845000	6	7.366393000	-0.901600000	0.731382000

6	7.911457000	-1.578968000	-0.365445000
6	7.080126000	-1.949575000	-1.428572000
6	5.716691000	-1.643231000	-1.393618000
6	-0.705902000	-4.769679000	0.058262000
6	-1.503393000	-5.167017000	1.145974000
6	-1.834824000	-6.510452000	1.342110000
6	-1.375053000	-7.485677000	0.449424000
6	-0.584131000	-7.103498000	-0.640227000
6	-0.255182000	-5.758607000	-0.832871000
1	1.992419000	-4.908806000	0.259307000
1	4.243225000	-3.432141000	0.084492000
1	5.286013000	1.744365000	-0.267951000
1	3.772010000	3.965317000	-0.013541000
1	8.002492000	-0.615721000	1.567201000
1	7.493918000	-2.474809000	-2.287525000
1	-2.449114000	-6.796477000	2.194081000
1	-0.228471000	-7.852662000	-1.345403000
6	0.972370000	3.379619000	-0.002557000
6	-1.430372000	-2.449418000	-0.399532000
6	-0.355716000	2.981741000	-0.199940000
6	1.256285000	4.821828000	0.248486000
7	-1.332819000	-1.081280000	-0.504715000
6	-2.781235000	-2.879295000	-0.676674000
7	-0.776735000	1.692883000	-0.448405000
6	-1.480104000	3.889266000	-0.228083000
6	0.996433000	5.800479000	-0.725783000
6	1.808284000	5.231731000	1.474340000
6	-2.602324000	-0.636987000	-0.812960000
6	-3.501613000	-1.756929000	-0.955715000
1	-3.117186000	-3.908174000	-0.680389000
6	-2.131102000	1.780825000	-0.687923000
6	-2.575353000	3.147124000	-0.555241000
1	-1.428052000	4.951882000	-0.030182000
6	1.274913000	7.148556000	-0.482162000
6	2.088062000	6.578596000	1.722377000
6	-2.991078000	0.702333000	-0.926602000
1	-4.547005000	-1.684957000	-1.225500000
1	-3.599277000	3.479863000	-0.666736000
6	1.821708000	7.543516000	0.744178000
1	1.070323000	7.890112000	-1.252366000
1	2.510542000	6.875173000	2.680746000
6	-4.413322000	1.011224000	-1.247052000
6	-4.742751000	1.702570000	-2.425649000
6	-5.453106000	0.641531000	-0.376747000
6	-6.071729000	2.010734000	-2.730816000
6	-6.782806000	0.948685000	-0.678618000
6	-7.098623000	1.633796000	-1.857759000
1	-6.305581000	2.542018000	-3.651735000
1	-7.573125000	0.659299000	0.012107000
1	-1.632206000	-8.532336000	0.600131000
1	2.039179000	8.592599000	0.935068000
1	-8.133887000	1.873447000	-2.092984000
1	8.973030000	-1.817155000	-0.390481000
26	0.325290000	0.014516000	-0.377256000
8	0.432322000	-0.963075000	-3.046912000
8	0.507202000	0.111254000	-2.264327000
1	0.575814000	5.493573000	-1.680614000
1	2.013125000	4.480625000	2.234151000
1	-1.861674000	-4.407845000	1.837540000
1	0.353513000	-5.461468000	-1.683643000
1	-5.203524000	0.126969000	0.547020000
1	-3.944082000	1.995945000	-3.103508000
1	5.069729000	-1.931431000	-2.219244000
1	5.578167000	-0.076588000	1.617555000
6	-2.321629000	1.142155000	2.435231000
6	-3.684260000	1.117113000	2.734450000
6	-4.307675000	-0.072985000	3.132728000
6	-3.539781000	-1.241427000	3.221137000
6	-2.175786000	-1.216938000	2.919890000
6	-1.527007000	-0.024244000	2.524634000
1	-1.858324000	2.067051000	2.101921000
1	-5.372153000	-0.091121000	3.359867000
1	-1.592733000	-2.134140000	2.975777000
16	0.195952000	0.006957000	2.168859000
1	-4.007437000	-2.180457000	3.516868000
1	-4.269207000	2.031355000	2.639051000

References

(1) Petasis, D. T.; Hendrich, M. P., Chapter Eight - Quantitative Interpretation of Multifrequency Multimode EPR Spectra of Metal Containing Proteins, Enzymes, and Biomimetic Complexes. In *Methods in Enzymology*, Qin, P. Z.; Warncke, K., Eds. Academic Press: 2015; Vol. 563, pp 171-208.
(2) Alessandro Bencini, D. G., *Electron Paramagnetic Resonance of Exchange Coupled Systems*. Springer Berlin, Heidelberg: 1990.
(3) Golombek, A. P.; Hendrich, M. P., *J. Magn. Reson.* **2003,** *165*, 33-48.
(4) Cohen-Tannoudji, C.; Diu, B.; Dui, B.; Laloë, F.; Hemley, S. R.; Ostrowsky, N.; Ostrowsky, D. B., *Quantum Mechanics*. Wiley: 1977.
(5) Slater, J. W.; Marguet, S. C.; Cirino, S. L.; Maugeri, P. T.; Shafaat, H. S., *Inorg. Chem.* **2017,** *56*, 3926-3938.
(6) Peters, M. K.; Röhricht, F.; Näther, C.; Herges, R., *Org. Lett.* **2018,** *20*, 7879-7883.
(7) Shirazi, A.; Goff, H. M., *J. Am. Chem. Soc.* **1982,** *104*, 6318-6322.
(8) Muresan, A. Z.; Thamyongkit, P.; Diers, J. R.; Holten, D.; Lindsey, J. S.; Bocian, D. F., *J. Org. Chem.* **2008,** *73*, 6947-6959.
(9) Wang, J.; Schopfer, M. P.; Puiu, S. C.; Sarjeant, A. A. N.; Karlin, K. D., *Inorg. Chem.* **2010,** *49*, 1404-1419.
(10) Ehudin, M. A.; Gee, L. B.; Sabuncu, S.; Braun, A.; Moënne-Loccoz, P.; Hedman, B.; Hodgson, K. O.; Solomon, E. I.; Karlin, K. D., *J. Am. Chem. Soc.* **2019,** *141*, 5942-5960.
(11) Wang, B.; Graskemper, J. W.; Qin, L.; DiMagno, S. G., *Angew. Chem. Int. Ed.* **2010,** *49*, 4079-4083.
(12) Ghiladi, R. A.; Kretzer, R. M.; Guzei, I.; Rheingold, A. L.; Neuhold, Y.-M.; Hatwell, K. R.; Zuberbühler, A. D.; Karlin, K. D., *Inorg. Chem.* **2001,** *40*, 5754-5767.
(13) Chufán, E. E.; Karlin, K. D., *J. Am. Chem. Soc.* **2003,** *125*, 16160-16161.
(14) Mondal, P.; Ishigami, I.; Yeh, S.-R.; Wijeratne, G. B., *Angew. Chem. Int. Ed.* **2022,** *61*, e202211521.
(15) Frisch, M. J.; Trucks, G. W.; Schlegel, H. B.; Scuseria, G. E.; Robb, M. A.; Cheeseman, J. R.; Scalmani, G.; Barone, V.; Petersson, G. A.; Nakatsuji, H.; Li, X.; Caricato, M.; Marenich, A. V.; Bloino, J.; Janesko, B. G.; Gomperts, R.; Mennucci, B.; Hratchian, H. P.; Ortiz, J. V.; Izmaylov, A. F.; Sonnenberg, J. L.; Williams; Ding, F.; Lipparini, F.; Egidi, F.; Goings, J.; Peng, B.; Petrone, A.; Henderson, T.; Ranasinghe, D.; Zakrzewski, V. G.; Gao, J.; Rega, N.; Zheng, G.; Liang, W.; Hada, M.; Ehara, M.; Toyota, K.; Fukuda, R.; Hasegawa, J.; Ishida, M.; Nakajima, T.; Honda, Y.; Kitao, O.; Nakai, H.; Vreven, T.; Throssell, K.; Montgomery Jr., J. A.; Peralta, J. E.; Ogliaro, F.; Bearpark, M. J.; Heyd, J. J.; Brothers, E. N.; Kudin, K. N.; Staroverov, V. N.; Keith, T. A.; Kobayashi, R.; Normand, J.; Raghavachari, K.; Rendell, A. P.; Burant, J. C.; Iyengar, S. S.; Tomasi, J.; Cossi, M.; Millam, J. M.; Klene, M.; Adamo, C.; Cammi, R.; Ochterski, J. W.; Martin, R. L.; Morokuma, K.; Farkas, O.; Foresman, J. B.; Fox, D. J. *Gaussian 16 Rev. C.01*, Wallingford, CT, 2016.
(16) Grimme, S., *J. Comput. Chem.* **2006,** *27*, 1787-1799.
(17) Ovalle, S.; Malardier-Jugroot, C., *Comput. Theor. Chem.* **2022,** *1213*, 113726.
(18) Weigend, F.; Ahlrichs, R., *Phys. Chem. Chem. Phys.* **2005,** *7*, 3297-3305.
(19) Barone, V.; Cossi, M., *J. Phys. Chem. A* **1998,** *102*, 1995-2001.
(20) https://www.chemcraftprog.com *Chemcraft* Version 1.8, build 682.
(21) E. D. Glendening, A. E. R., J. E. Carpenter, F. Weinhold *NBO Version 3.1*.

(22) Mondal, P.; Ishigami, I.; Gérard, E. F.; Lim, C.; Yeh, S.-R.; de Visser, S. P.; Wijeratne, G. B., *Chem. Sci.* **2021,** *12*, 8872-8883.
(23) Liu, J.-G.; Ohta, T.; Yamaguchi, S.; Ogura, T.; Sakamoto, S.; Maeda, Y.; Naruta, Y., *Angew. Chem. Int. Ed.* **2009,** *48*, 9262-9267.
(24) Kim, H.; Rogler, P. J.; Sharma, S. K.; Schaefer, A. W.; Solomon, E. I.; Karlin, K. D., *Angew. Chem. Int. Ed.* **2021,** *60*, 5907-5912.
(25) Liu, J.-G.; Shimizu, Y.; Ohta, T.; Naruta, Y., *J. Am. Chem. Soc.* **2010,** *132*, 3672-3673.